NON-DESTRUCTIVE VISCOELASTICITY MICROSCOPY: A SPECTROSCOPIC APPROACH USING DUAL BRILLOUIN/RAMAN SCATTERING PROCESSES

A Dissertation

by

ZHAOKAI MENG

Submitted to the Office of Graduate and Professional Studies of
Texas A&M University
in partial fulfillment of the requirements for the degree of

DOCTOR OF PHILOSOPHY

Chair of Committee,	Vladislav V. Yakovlev
Committee Members,	Brian E. Applegate
	Javier A. Jo
	Alexei V. Sokolov
Head of Department,	Anthony Guiseppi-Elie

May 2016

Major Subject: Biomedical Engineering

ABSTRACT

The tremendous progress in life sciences and medicine has been greatly facilitated by the development of new imaging modalities. The elastic properties of molecules, sub-cellular and cellular structures play a crucial role in many areas of biology and medicine. Tissue elasticity has recently been recognized as a critical regulator of cell behavior, with clear roles in embryogenesis, tissue morphogenesis and stem cell differentiation, as well as contributing to pathologies such as tumor progression, coronary artery disease and tissue scarring. This dissertation is focused on developing a novel instrumentation to image viscoelastic properties of cells and tissues using Brillouin microspectroscopy. Following design, construction and optimizations that maximize the signal quality, we obtained the highest resolution Brillouin imaging system in a confocal backscattering arrangement suitable for bio-imaging applications. Furthermore, a powerful combination of Brillouin and Raman spectroscopies has yielded a confocal microscope capable of performing simultaneous mechanical and chemical imaging in a non-invasive and non-contact manner.

The novel instrument was optimized and validated for several biomedical applications. For example, we demonstrated that Brillouin spectroscopy is capable of performing *in-vivo* measurements of the mechanical properties of artificial biocompatible materials such as photocrosslinkable gelatin methacrylate (GelMA). With the assistance of animal models of human congenital muscular dystrophies, we show that Brillouin spectroscopy can serve as a unique diagnosis tool, which can detect differences in muscle elasticity even between very similar muscular dystrophy genotypes. We have also demonstrated that Brillouin spectroscopy is an invaluable approach in developmental biology since it is capable of making non-destructive imaging of an embryo's elasticity during its development process, which is crucial to understand the formation of many essential organs such as bone and brain.

In summary, we have developed a novel instrument for biomedical imaging sensing, which is compatible with other microscopic imaging modalities and is specific to local elasticity. Numerous applications of this new technology have been explored, and the instrument's performance was validated for several systems.

ACKNOWLEDGEMENTS

Many people contributed to the final form of this dissertation. First of all, I would like to thank my committee chair, Prof. Vladislav V. Yakovlev for his solid support for my research and studies. During the past five years, his extensive knowledge and innovative ideas were always the most important guidance for my research. Besides, he also impressed on me his diligent work and enthusiasm for scientific research, which will definitely influence my future life.

I also thank my committee members, Prof. Brian E. Applegate, Prof. Javier A. Jo, and Prof. Alexei V. Sokolov, for their guidance and support throughout the course of my research. Their comments and suggestions for my dissertation were really helpful.

I would like to thank Dr. Georgi I. Petrov for his patient guidance, which helps me overcome the initial barriers in the field of experimental optics. His comprehensive knowledge and innovative ideas always inspired me to find solutions for many technical challenges.

I would like to thank my lab mates, Mr. Charles Ballmann, Mr. Joel Bixler, Mr. Zachary Cooker, Dr. Brett Hokr, Dr. John D. Mason, Mr. Dawson Nodurft, Mr. Jonathan Thompson, Dr. Andrew Traverso, Ms. Maria Troyanova-Wood, and Mr. Sergio Warqued, for sharing their ideas and experiences. Working in such a group was a memorable experience.

Many collaborators contributed to this research project. I would like to thank them, Prof. Vladislav M. Panin, Prof. Akhilesh K. Gaharwar, Prof. Marlan O. Scully, Prof. Arne Lekven, Prof. Alvin T. Yeh, Prof. Roland R. Kaunus, Prof. Kenith E. Meissner, Prof. Michael R. Moreno, Prof. Zhandos N. Utegulov, Dr. Holly Gibbs, Dr. Manish K. Jaiswal, Dr. Sandra C. Bustamante-Lopez, Dr. Yuqiang Bai, Miss Teena Thakur, Mr.

Mingliang Jiang and Mr. Ryan Baker. The research presented in this dissertation will not be performed so smoothly without their ideas, and efforts.

I would like to thank the undergraduate students who collaborated with me during the last four years, Mr. Berkay Basagaoglu, Mr. Ben Boyett, Miss Chandani Chitrakar, Miss Cassidy Gobbell, Miss Jessica Hanson, Miss Hailey Marsh, Miss Marianna Peraza, Mr. Zachary Steelman, Mr. Carlos Tovar, and Mr. Omar Yusufzai. I would like to thank them for sharing their time, ideas, efforts and assistances.

I am very thankful to my former academic advisors. I would like to thank Prof. Ping Yang and Prof. George W. Kattawar for their efforts during my Master's studies. More importantly, without their guidance and advices, I will not enter the field of optics, and recognize the field of biomedical engineering and experimental optics. I would like to thank Prof. Chunxu Pan for his guidance during my undergraduate studies. I cannot start my research life so smoothly without his directions.

I would like to thank Prof. Giuliano Scarcelli and Prof. Seok-Hyun Yun for sharing their ideas, suggestions and comments. Without their help, I cannot establish the Brillouin imaging system so efficiently.

Finally, sincerest gratitude is owed to every member in my family – my wife, my parents and my grandparents. Their love and support always accompanied me and enabled me to continue my research and obtain the degree.

TABLE OF CONTENTS

Page

LIST OF FIGURES

LIST OF TABLES

TABLE Page

CHAPTER I

INTRODUCTION

The elastic properties of molecules, sub-cellular and cellular structures play a crucial role in many areas of biology and medicine. Tissue stiffness has recently been recognized as a critical regulator of cell behavior, with clear roles in embryogenesis, tissue morphogenesis and stem cell differentiation, as well as contributing to pathologies such as tumor progression, coronary artery disease and tissue scarring. In the field of biomedical studies, the importance of elasticity and viscosity are hard to underestimate. In a classical example of breast cancer self exam, women are asked to check for lumps, and roughly 40% of breast cancers are first detected by women themselves feeling hardened knots in some parts of their breasts. Elastography, a relatively new medical imaging modality, which deals with measuring and mapping elastic properties of tissues, is mostly dominated by ultrasound imaging [2]. Nevertheless, microscopic ultrasound imaging is limited in spatial resolution, which is defined by the acoustic frequency (~10 MHz). Higher frequency ultrasound experiences a very strong absorption in water and biological tissues, limiting the penetration depth and applicability of such imaging modality. Only several reports have been published on using GHz range ultrasound for cell-level imaging [3, 4].

Brillouin spectroscopy, being first introduced to the field of biomedical research about 40 years ago, is emerging as a promising spectroscopic imaging method to provide a new contrast in biomedical imaging. In this dissertation, we aim to develop a microscope based on spontaneous Brillouin light scattering, which enables high-resolution mechanical imaging in a non-invasive manner. We, first, provide a brief overview of instrumentation and challenges of Brillouin spectroscopy. We will then provide with a synopsis of developing new breakthroughs in instrumentation and applications, which inevitably will lead to new fundamental discoveries, research and clinical applications,

and commercial products. The theory governing the physical principles of spontaneous Brillouin light scattering, and the corresponding optical instrumentation suitable to simultaneously collect Brillouin and Raman signals is given in Chapter 2. Showcases of the results obtained by the dual Raman/Brillouin microscopy/spectroscopy are presented in Chapter 3-6. In Chapter 7, we propose the coherent Raman/Brillouin spectroscopy, and provide a viable optical instrumentation. The demonstrative results are presented as well.

1.1 Optical Scattering and Spectroscopy

Optical spectroscopy techniques are critical in a variety of disciplines, including biomedical applications, material science and applied physics (e.g., [5-19]). These techniques are aimed to characterize the physical properties of a target, including its morphological, mechanical and chemical properties, using its light scattering behaviors. Since the pioneer investigations by Mie [20], Brillouin [21] and Raman [22], optical spectroscopy and light scattering problems have been consistently investigated for nearly one century. With the technology advancements emerged during the last few decades, including lasers, ultra-sensitive optical detectors, and high-resolution spectrometers, optical scattering and spectroscopy have become an emerging approach for biomedical applications.

From the microscopic view, all matters are composed by molecules, atoms and even free electrons (such as in metals). The incident electromagnetic field interacts with these micro-systems mainly in two ways:

1. Electric charges in the systems are driven to oscillate at the same frequency as the incident source, oscillations of the charges will emit the same-frequency electromagnetic waves in all directions;

2. Quantum states of the system are changed by incident source, and the electromagnetic waves with a new frequency will be re-emitted.

The first kind of interaction includes all elastic scattering processes, including Rayleigh/Mie scatterings [1, 20, 23] and other scatterings induced by non-spherical particles [24-26]. The wavelength of the scattered light remains identical to the incident field. In this case, part of the radiative source energy would be transferred to other forms of energy, such as thermal energy, which defines the absorptivity / transparency of the system. The second kind of interaction includes all types of inelastic scattering processes, such as Raman scattering, Brillouin scattering, fluorescence, etc. In this case, the wavelength of the scattered light is different from the incident light. Depending on the scattering mechanism, the wavelength difference between the scattering and the incident light, or wavelength/frequency shift, represents certain physical/chemical properties of the scatterer. For example, when a Raman scattering happens, the wavelength shift is an indicator of a specific type of chemical bond within the scatterer.

Fig. 1 illustrates the two types of scattering processes described above. In this case, a monochromatic light is sent into a sample. After a light-matter interaction, a portion of the photons is re-emitted from the sample and forms the scattered light field. The wavelength of the scattered photons may or may not remain the same as the incident photons, depend on the scattering mechanism. A variety of characteristic information could be extracted from the scattered light field, including the sample's chemical composition, mechanical properties, and morphological information.

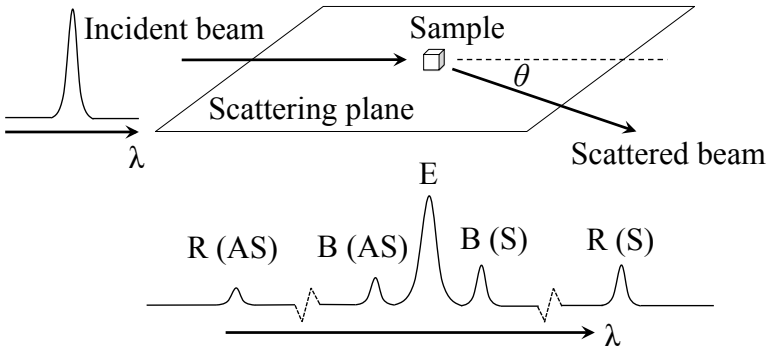

Figure 1 Illustration of the light scattering process, and the spectrums of the incident beam and the scattered beam, respectively. The output intensity, wavelength shift and angular dependence all characterize the sample, including its chemical, morphological and mechanical properties. R: Raman; B: Brillouin; E: Elastic scattering; S: Stokes peak; AS: anti-Stokes peak.

1.1.1 Raman spectroscopy

Raman scattering is an inelastic scattering phenomenon of a photon. It was first discovered by C. v. Raman and K. S. Krishnan in 1928 [22]. It provides valuable characteristic information about molecular species and their chemical bonds. When compared with other molecular-specific imaging techniques (e.g., fluorescence, chemiluminescence or radioactivity microscopies), Raman spectroscopy provides a label-free contrast mechanism intrinsically induced by the molecules contained in the sample. It sets investigators free from complicated sample preparation processes and allows substantial multiplexity due to a narrow line-width of Raman transitions. In many bio-imaging applications, it often provides better molecular specificity, faster imaging speed and higher spectral resolution [27, 28].

Theoretically, Raman scattering is resulted from an excitation-emission process of the molecules. The frequency of molecular vibration range (~ 10^{12} Hz – 10^{14} Hz) corresponds to the radiations in the infrared region in electromagnetic spectrum. In most biomedical applications, experiments are done in room temperature, and most of the

molecules stay in the ground state. Only a few molecules stay in the excited state. The ratio between the numbers of the two molecule types can be described by Boltzmann's distribution. Ground molecules can be excited to higher states by absorbing incident electromagnetic radiations (e.g., photons). In the inelastic scattering process, an absorbed photon is re-emitted with a different energy. In Raman scattering process, the difference in energy between the absorbed and the re-emitted photons corresponds to the energy required to excite a molecule to a higher vibrational mode. Fig. 2 shows the energy diagram for a typical Raman process in comparison with an elastic scattering process.

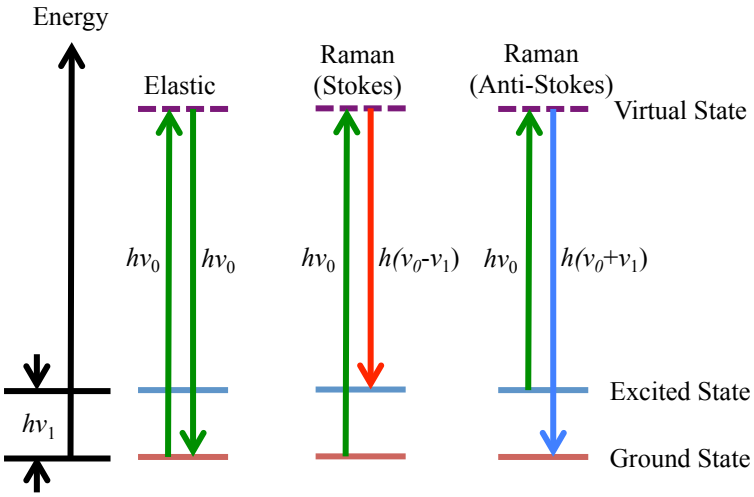

Figure 2 An energy diagram for a typical elastic scattering process, and Raman scattering processes (Stokes and anti-Stokes). The "excited state" represents the excitation of molecule bond vibration.

Typically, the measurable properties of Raman peaks include the peak intensity, frequency shift, line shape and the polarization status. For a typical chemical bond, the vibrational frequency is fixed in a relative small range. For example, CH_2 starching vibration corresponds to 2845 cm^{-1} Raman line, while =CH group could results a 3015 cm^{-1} Raman line [29]. Moreover, the Raman line-shape and polarization status usually corresponds to the finer or secondary structures of the molecules. The Raman scattering

application is extensively studied for non-biological materials. However, corresponding investigations for biomedical applications is still required.

Experimentally, Raman scattering can be detected by various principles, including direct spontaneous Raman scattering detection, stimulated Raman scattering (SRS) [7, 9, 12, 15, 30-32], coherent anti-Stokes Raman scattering (CARS) [6, 14, 33], surface enhanced Raman scattering [10] and Raman induced Kerr effect (RIKE), etc. Some methods are capable to make detections over the whole spectrum in one time. In those methods, the desired signals contain photons with different frequencies, and can be separated by optical gratings. A CCD detector can be used to collect the separated light, and record the properties of Raman peaks. The similar detections can also be achieved by wavelength tuning. For example, for the stimulated Raman scattering detection, we can fix the pump laser while tuning the wavelength of the probe laser. By scanning the probe over a spectrum range, we can get a whole picture of the Raman spectrum.

1.1.2 Spontaneous Brillouin spectroscopy

The origin of the Brillouin effect can be traced down to the theory of light scattering on random fluctuations of local density described by Smoluchowski and Einstein [34, 35]. Those density fluctuations, as it was pointed by Mandelshtam [36], can be considered as a superposition of elastic waves propagating in all possible directions.

The history of Brillouin effect is rather fascinating. In Russian literature it is called Mandelshtam-Brillouin scattering, and there is a substantial reasoning for this, since Leon Brillouin in his original paper [37], which is often cited as the first description of Brillouin scattering effect, actually describes inelastic light scattering on two counter propagating acoustic waves. Such an arrangement is likely to happen in impulsive stimulated Brillouin scattering, where optical pulses excite two acoustic waves. Leonid

Mandelshtam first described the true spontaneous Brillouin scattering, which originates from dissipating fluctuations in a medium, in 1918. However, being dedicated to experimentally observe his theoretical predictions, he only published these results in 1926. Interestingly enough, Raman scattering, which Mandelshtam and Landsberg first observed in quartz in 1928, was an unexpected finding, which they haven't rushed to publish because the observed wavelength shift was much larger than the one predicted by Mandelshtam's theory. The best experimental results, which they were able to obtain, indicated that there is some possible line broadening of mercury lines upon scattering in quartz. When visiting the State Optical Institute in St. Petersburg (at that time, Leningrad) in 1930, Mandelshtam learned that Eugenii Gross had developed a unique optical set up of several cascaded interferometers capable of providing substantial frequency dispersion to analyze the fine structure of atomic lines [38]. During discussion, Gross acknowledged his knowledge of Mandelshtam's paper of 1926 and admitted of sending out his results on the first experimental observation of this effect [39]. In a series of follow-up work [40-42], Gross was able to fully confirm all theoretical predictions of Mandelshtam's theory. Thus, if we want to acknowledge the historical fairness, spontaneous Brillouin scattering should be called Mandelshtam-Gross effect, while any stimulated version of it should be referred to as a Brillouin effect. Alternatively, paying tribute to the extraordinary contributions of all scientists involved in this fascinating discovery, it should be named Mandelshtam-Gross-Brillouin effect. However, in order to avoid any possible confusion, we will use the original name commonly used in literature, Brillouin scattering, through the whole text of this review.

The physical principles governing spontaneous Brillouin spectroscopy is described in the next few paragraphs. When a monochromatic electromagnetic wave, $\vec{E} = \vec{E}_0 \cos\left(\omega_0 t - \vec{k}\vec{r}\right)$, interacts with an elastic wave, $\vec{A} = \vec{A}_0 \cos\left(\Omega t - \vec{q}\vec{r}\right)$, where $\vec{k}$ and $\vec{q}$ are the wave vectors of electromagnetic and elastic waves, respectively, the electromagnetic wave will diffract in the direction defined by the angle:

$$\sin\frac{\theta}{2}=\frac{\lambda}{2n\Lambda}, \tag{1.1}$$

where λ and Λ are the wavelengths of electromagnetic and elastic waves, and n is the refractive index of the medium.

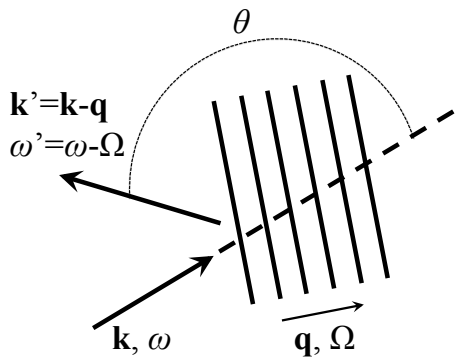

Figure 3 Schematic of the spontaneous Brillouin scattering process.

The intensity of light scattering will modulated by $\cos(\Omega t)$ leading to the appearance of two satellite frequencies, ω-Ω and ω+Ω, which are called the Stokes and the anti-Stokes components in Brillouin spectroscopy, respectively. Ω is the modulation frequency of the elastic wave, which can be re-written taking into account Eq. (1.1) as

$$\Omega = v\,q = v\left(\frac{2\pi}{\Lambda}\right) = 2\omega_0 n\frac{v}{c}\sin\frac{\theta}{2}, \tag{1.2}$$

Here, c and v are the speed of light and sound, respectively. Therefore, by measuring the frequency shift of a scattered wave, one can measure the local speed of sound in the medium, which, in its turn, is related to the elastic properties of the medium. One can see that this frequency shift reaches its maximum in back scattering geometry, i.e. when θ=180°. For many practical applications, this is the most desirable geometry, so, unless otherwise is specified, we will consider the backscattering geometry and a relative frequency shift to be

$$\frac{\Omega}{\omega_0}=2n\frac{v}{c}. \tag{1.3}$$

On the other hand, the decay of elastic waves causes a line broadening of those satellite components. This line broadening is proportional to absorption of GHz sound waves in a material under study. From the general equation governing the propagation of longitudinal acoustic waves in a viscoelastic medium the complex longitudinal modulus, M^*, is given by [1]:

$$M^* = M' + iM'' = \rho v^2 + i\frac{2\rho v^3 \alpha}{\Omega} \tag{1.4}$$

where α is the attenuation of the acoustic phonons, related to the line bandwidth at the full-width half-maximum (FWHM), Δ, as

$$\Delta = \frac{\alpha v}{\pi} \tag{1.5}$$

As one can see from the Eqns. 1.3-1.5, Brillouin spectroscopy measurements permit to fully describe the complex modulus of material for a known density, ρ, of material. It is important to acknowledge the fact that the above-described modulus describes the propagation of GHz-frequency ultrasound, i.e. reflects the high-frequency modulus of material, which is substantially different from the conventional Young's modulus measured by stress-strain measurements, or quasi-static modulus. Recent studies [43, 44] revealed a power-law dependence of the elastic modulus on the frequency. This theoretically derived relationship with the scaling factors, which can be experimentally measured for any particular system, is extremely valuable for using Brillouin spectroscopy, which assess high frequency modulus, for analysis of biological tissues, for which quasi-static elastic modulus can vary several orders of magnitude for different tissues. As one can see from the example, given by Scarcelli et al. [45], almost two orders variation of quasi-static modulus results only in a moderate change of Brillouin shift and related high-frequency modulus.

Table 1 compares the differences between Brillouin and Raman scattering processes. Although both processes are based on inelastic light scattering, their typical frequency/wavelength shifts are substantially different. Therefore, different instruments

are required to perform the detections. The corresponding optical instrumentations will be described in Chapter 2.

Table 1 Comparison between spontaneous Raman and Brillouin spectroscopies

	Brillouin	**Raman**
Typical shift	~ 1 – 10 GHz (0.03 – 0.3 cm^{-1})	100 – 4000 cm^{-1}
In wavelength	~ 1 – 10 pm	~ 10 – 150 nm (for visible laser source)
Source of contrast	Sound velocity, or longitudinal modulus	Chemical bonds

1.1.3 Coherent Brillouin spectroscopy

The coherent Brillouin scattering processes are introduced in the next few paragraphs. Brillouin scattering involves parametric interaction of optical and acoustic waves. The classical description of this nonlinear interaction is similar to nonlinear Raman scattering [46], and, similar to coherent Raman effects, such as coherent anti-Stokes Raman scattering (CARS) [47, 48], stimulated Raman scattering (SRS) [49, 50], impulsive stimulated Raman scattering (ISRS) [51-53], and Raman induced Kerr effect scattering (RIKES) [54-56], totally analogous nonlinear optical effects were experimentally observed in the medium, where, instead of molecular vibrations, acoustic oscillations were used as a source of nonlinearity. These effects include coherent anti-Stokes Brillouin scattering (CABS) [57], stimulated Brillouin scattering (SBS) [58], impulsive stimulated Brillouin scattering (ISBS) [59, 60], and Brillouin induced Kerr effect scattering (BIKES) [61, 62].

Unlike coherent Raman scattering spectroscopies, none of the above methods, except ISBS, was able to gain popularity, despite being claimed to be superior to spontaneous

Brillouin scattering in terms of its signal amplitude. We believe, it is mostly due to the instrumental challenges, since nonlinear Brillouin spectroscopy normally requires two laser sources, whose relative wavelength should be controlled with MHz precision.

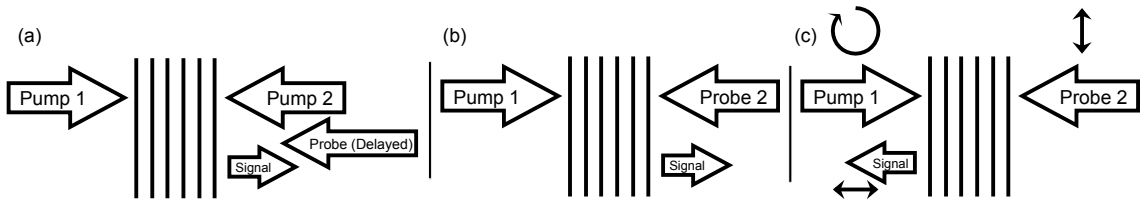

Figure 4 Illustrative diagrams of CABS (a), SBS (b) and BIKES (c).

On the other hand, ISBS spectroscopy has been widely used for spectroscopic studies. Following the original work by Nelson and Fayer [63], counter-propagating acoustic waves are excited in a sample using a pair of interfering short laser pulses and form a standing wave, whose amplitude varies an time, as two acoustic waves are traveling one against each other and decay in time. The second pulse or, in some cases [64], cw beam samples the temporal behavior of this diffraction grating through an acousto-optical effect, and provides the same information as Brillouin spectroscopy, except in the time domain. Due to abundance of short-pulsed laser systems, ISBS gained significant interest in studying liquids and glassy transitions[53, 63, 65-68].

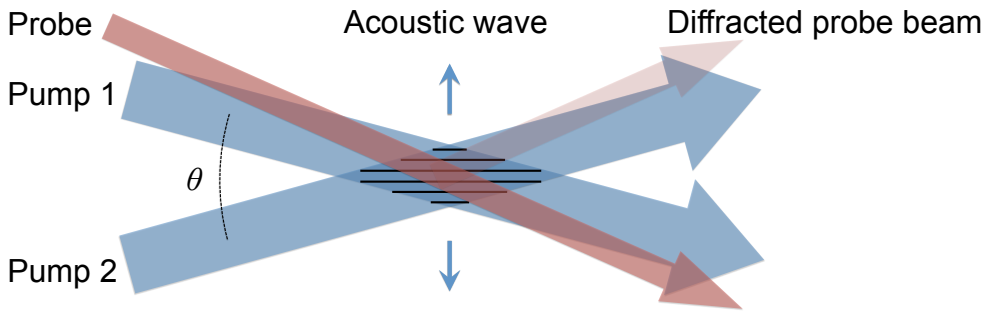

Figure 5 Illustration of the ISBS process showing the generation of counter-propagating acoustic waves.

1.2 Mechano-Biology

The elastic properties of human body parts, such as muscle, adipose (fat), and skin, are usually indicators of a person's health status. A patient goes to the doctor's office often because of a mechanical change or defect in his/her body, such as a new swelling or lump, muscular stiffness, edema, constricted blood flow, or obstructed airflow. As such, the ability to measure the mechanical properties of the human body – including elasticity or compressibility – is critical to advancing our understanding of how the body's physical properties change as a disease develops or as part of regular biological functions, such as embryo development or wound healing. In order to understand physiological-related aspects of living systems, we must first be able to explain how mechanical properties contribute to affect the physiological properties of living cells and tissues, as well as how the external forces impact cell fate and developmental process [69]. Such insights will enrich not only basic life science but also approaches to clinical therapy.

Clinicians recognized the central importance of physical forces in physiological control quite early. Well-known examples include the effects of inspiratory pressure on lung function, hemodynamic shear stress on vascular remodeling, compression on bone generation, and tension on skin aging. During the last few decades, investigators started to reveal the central role of physical forces in genetic and cellular regulation, as well as in developmental control [70]. The researches on biomechanics has grown exponentially since then. Currently, this field covers a wide range of scientific/engineering disciplines including biophysics, molecular biology, cell biology, developmental biology, genetics and physiology, as well as optical engineering, mechanical engineering, materials science and nanotechnology.

Recent studies revealed that microscopic changes in cell mechanics and extracellular matrix structure could dysregulate molecular mechanisms of mechanotransduction, a

process by which cells sense external mechanical signals and convert them into chemical/physiological responses [70-72]. Examples exist among morphogenesis, cancer developments and other diseases. For example, altered matrix mechanics would induce developmental abnormalities (e.g., osteogenesis imperfecta); hydrodynamic flow-mediated tumor cell adhesion would cause elevated cancer cell metastasis [73, 74]. There are numerous other examples in virtually all areas of medicine and surgery [75]. Specifically, in embryonic and cancer developments, physical forces, material flows, and cellular mechanics input essential signals in the program that drives cell sorting, differentiation, growth and angiogenesis [76]. In these cases, biomechanics underlies the abilities of cells, tissues or organs to perform normal functions in health or to malfunction in disease.

1.3 Review of Current Elastography Techniques

Elastography is a medical imaging modality that maps the elastic properties of biological tissues. Currently, the most prominent techniques in elastography are ultrasound and magnetic resonance imaging. Specifically, ultrasound techniques use ultrasound waves to image the internal body/organ structures [2, 77]. External ultrasound pulses are sent into the body by means of a transducer. Their reflections (echoes) are recorded to yield an image. In this technique, an external mechanical force (stress) is applied to tissue, and the ultrasound images prior to and after the compression are compared. The areas of the image that are least deformed (strain) are the stiffest, while the most deformed areas are the softest [2, 78]. On the other hand, Magnetic Resonance Imaging (MRI) uses strong magnetic fields and radio waves to yield an image of the body [79]. In MRI elastography, a mechanical vibrator is used on the surface of the patient's body which creates mechanical waves that travel into the patient's deeper tissues. An imaging acquisition sequence that measures the velocity of the waves is used, and this is used to extract the tissue's stiffness (the Young’s/shear modulus) [79, 80]. The result of an MRI

elastography is a 3D map of the tissue stiffness, which is capable of covering the patient's entire organ or body.

Although the ultrasound and MRI techniques have been extensively used in clinical practices for over 20 years, they are inherently limited by a spatial resolution of the order of hundreds of microns. Over the last decades, the scientific community has made great efforts to enhance the spatial resolution of elastography systems down to a micrometer scale, which would eventually enable investigators to image the mechanical properties of microscopic/cellular biological systems. For example, the employment of optical techniques has led to the development of optical elastography (OE), a rapidly expanding research area that aims to extract mechanical information of biological specimens by a combination of optical and mechanical approaches. Specifically, Optical Coherence Elastography (OCE) benefits from the superior spatial resolution of Optical Coherence Tomography (OCT), and have shown promising applications in a variety of research fields [81-84]. Since its first development in 1998 [85], OCE was utilized to assess the tissue biomechanics through the measurement of localized deformation and strain inside of the sample. It generally relies on an external or internal mechanical stimulation to load the tissue and an OCT detection to measure the tissue's mechanical response [86]. Reinforced by the high spatial resolution of OCT, the imaging spatial resolution of OCE is ranging from several to hundreds of microns [87], while keep an adequate field of view (FOV). Nevertheless, external or internal mechanical perturbation is required for OCE measurements.

On the other hand, investigators employed atomic force microscopy (AFM) to make direct mechanical contact with cellular level biological samples, and extract the localized mechanical properties [88]. Originally, AFM was developed for high-resolution imaging purposes. It has unique capabilities to probe the mechanical modulus of the sample by recording the deformation resulted at its nanoscopic indenters. Particularly, sharp indenters are used to probe the cell cytoskeleton, and the elasticity information is derived

by analyzing the force response through different contact models. AFM elastography combines imaging and indentation modalities to map the spatial distribution of biological samples, which is capable of reflecting the structure and function of the underlying cytoskeleton. The utilization of AFM elastography has substantially contributed to our understanding of cell mechanics and cell biology. However, this technique could only make surface detection of samples with a penetration to be less than 20 nm. In this sense, 3D elasticity-specific imaging is impossible. Moreover, the sharp nano-indenter can also lead to irreversible damages on the sample, making this technique to be destructive and invasive.

Several other nanoscale imaging/sensing techniques, such as X-ray diffraction (XRD) [89] and electron microscopies, including transmission electron microscopy (SEM) and scanning electron microscopy (TEM) [90], were also developed for the proposes of mechanical probing. Their underlying physical principles are similar with OCE: the imaging techniques are used to capture the deformation information of the sample under external/internal mechanical perturbations. However, the destructive nature of X-ray and electron beams and the limited field of view (FOV) usually forbid investigators to make *ex-vivo*/*in-vivo* whole-cell observations.

Nevertheless, the utilization of OCE, AFM and SEM/TEM has yielded fruitful results for a variety of biological samples. Unfortunately, the results derived by these microscopic techniques did not show a good agreement with the conclusions drawn from macroscopic approaches. For example, the elastic modulus of individual type 1 collagen fibrils were found to be several GPa when measured by AFM [91] or XRD [89]. However, for macroscopic collagen tissues and corneal collagen crosslinking, the elastic modulus is markedly reduced to several kPa [92, 93]. Cancer cells are softer than healthy cells when measured by AFM [94-96]. To the contrary, the cancerous tissues are usually more than 10 times stiffer than healthy tissues in macroscopic scale [97, 98]. These contradictions imply that the microscopic biomechanical properties of living organisms

are usually not simply an analogy of their macroscopic counterparts. Their mechanical properties are not only depended on discrete functions, but also relied on the scale of measurement [92]. Therefore, in order to fully understand the underlying mechanisms of biological systems, a reliable mechanical-specific imaging modality specified for 100 nm to 10 μm applications is expected.

1.3.1 Spontaneous Brillouin elastrography

Unlike all the aforementioned techniques, Brillouin spectroscopy permits the determination of the elasticity modulus of sample volumes of a few cubic microns. As an optical technique, Brillouin spectroscopy provides a viable pathway to viscoelastic characterization without any mechanical perturbations. The spatial resolution of Brillouin spectroscopy follows the general optical rules for a typical confocal microscope, which ranges from <200 nm to several micron, depending on the focusing geometry of the laser beam. It offers a non-contact, non-invasive, and label-free contrast mechanism with microscopic spatial resolution and enables investigations of cellular/tissue mechanics with a sub-micron spatial resolution, which is essential for understanding biological development and disease pathophysiology [78]. Moreover, for most of the biological samples, the penetration depth of Brillouin spectroscopy could approach hundreds of microns, making cellular and tissue level 3D imaging possible.

However, compared with other imaging modalities such as fluorescence and optical reflectance, Brillouin scattering is a weak process. In most situations, elastically scattered light due to Rayleigh/Mie scattering or optical reflections is orders-of-magnitude stronger than Brillouin signal. Therefore, a suitable Brillouin spectrometer should be offered with both sub-GHz spectral resolution as well as high spectral contrast (or extinction). The requirements on spectral resolution and extinction had been achieved by scanning-grating monochromators [99], optical beating methods [100], and

multiple-pass scanning Fabry-Perot interferometers [101]. However, these techniques require sequential scanning over the optical frequency. Consequently, it usually requires a few minutes to several hours to obtain a single Brillouin spectrum, depending on the insertion loss of the instrument. In this sense, these probing methods are only good for single-point sampling or static measurements. Multi-points scanning/imaging will be impractical with these techniques.

Over the past decade, the optical instrumentation for Brillouin spectroscopy and microscopy has been dramatically improved. The application of Virtually Imaged Phase Array (VIPA) and various other innovative designs introduced by Scarcelli et al. have greatly enhanced the acquisition efficiency of Brillouin spectra [5, 102, 103]. As a result, the entire Brillouin spectra can be acquired within 10 seconds in a fully parallel and non-scanning manner. Nevertheless, for most practical applications, the elastic scattering is orders-of-magnitude stronger than Brillouin signals. Without sufficient suppression of elastically scattered light, the residual component of elastic scattering may contaminate or overlap with the dispersed spectrum, making it difficult to identify the Brillouin spectrum.

In order to overcome this difficulty, Scarcelli et al. developed a multi-stage VIPA spectrometer [102]. In brief, this is a method of cascading multiple VIPAs in an orthogonal-axis configuration. The cross-axis cascade approach provides a simple way to separate the stray light from the Brillouin signal after each stage. Therefore, this innovative setup is capable to reducing the background and crosstalk. The two-stage VIPA spectrometer could provide a 55-dB extinction ratio, which is ~ 25-dB greater than a single-stage VIPA. Scarcelli et al. also extended this optical arrangement to a three-stage setup, which is capable of providing an 80-dB extinction ratio. Recently, Berghaus et al. further enhanced the extinction ratio and the finesse of 2-stage VIPA spectrometers using two VIPAs with different free spectral range (FSR) [103, 104]. Compared with 2-

stage VIPAs with identical FSR [102], the new design provides a greatly improved rejection ratio of white-light background noise.

The innovations in multi-stage VIPA spectrometers provide a crucial step towards the application of Brillouin scattering spectroscopy to turbid samples, including biological tissues. However, although multi-stage VIPA arrangement provide ultrahigh extinction ratio, the signal transmission is substantially decreased. The multi-stage arrangements also increase the system's complexity. Moreover, for some biological samples, such as skin, adipose tissue and bone, the extinction ratio created by multi-stage arrangement is still insufficient for making practical and routine measurements.

During the last few years, Meng et al., Antonacci and Török and Scarcelli et al. have developed a variety of techniques to eliminate the parasite elastic photons within the Brillouin spectra and have substantially enhanced the signal quality obtained from a VIPA-based Brillouin spectrometer [105-107]. Specifically, in Meng et al.'s approach, a molecular/atomic gaseous absorptive cell is utilized as a narrow-band notch filter, which absorbs the elastic photons while transmits the Brillouin signals. Antonacci and Török introduce a reference beam, which heterodyne with the backscattered beam from the sample. In this way, the unwanted elastic photon is removed via destructive interference. More recently, Scarcelli et al. introduced a custom designed Farby-Perot etalon into the back-scattered beam, which is capable of rejecting the unwanted elastic photons while pass the Brillouin signals.

With the assistance of the technical improvements, Brillouin spectroscopy has emerged as a promising spectroscopic imaging method to provide a new contrast in biomedical imaging at different levels of spatial organization, including cellular/subcellular level, tissue level and whole-body measurements [105, 106, 108-113]. More importantly, Brillouin spectroscopy is fully compatible with other methods and can provide new information to chemical imaging using Raman spectroscopy or fluorescence

spectroscopy imaging, since Brillouin spectrum does not interfere with those spectroscopies [112, 114-118].

1.3.2 Historical and current biomedical applications of Brillouin spectroscopy

The very first proposal to use Brillouin spectroscopy to study systems of biological significance likely belongs to Fabelinskii [119]; however, the first experimental data on gelatin gel, which is considered to be an important biomaterial, appeared only in 1976 [120]. Within several years after this first biological application, several groups successfully attempted in measuring Brillouin spectra of collagen and collagen-rich tissues [121-123]. The very first application to a biomedical problem was reported in 1980 by Vaughan and Randall [124], who measured for the first time the elastic properties of the lens and cornea of the eye. Despite very impressive data showing the appropriateness of Brillouin spectroscopy for such measurements, a significant drawback of a long acquisition time (10 minutes to achieve ~1000 photon counts, corresponding to the SNR of just over 10) was noted. Since many biological samples require some fixing procedure to be characterized or imaged on this time scale, and a fixing procedure might affect the elastic properties of a sample under study, Brillouin spectroscopy was for a long time considered to be not so useful for biomedical imaging. Significant elastic light scattering in biological samples was also considered as a substantial barrier to any practical application. Thus, most of the work for almost 30 years was focused on the systems, which were unlikely to undergo any significant variations over an extended period of time, such as bones [120, 125]. Despite these drawbacks, during this time Brillouin spectroscopy was applied to many biological systems and new experimental techniques were invented. The elastic properties of dipalmitoyl phosphatidylcholine (DPPC), the major constituent of pulmonary surfactant, were measured [126]. The speed of sound in DNA, which is a measure of the long range interatomic forces in the molecule, was measured [127, 128]. The compressibility of

lysozyme in solution was measured by the use of optical heterodyne detection [129]. This was significant at the time because the method used provided a way to detect the small shift in frequency from the lysozyme in solvent solution relative to the solvent alone. Brillouin scattering allowed the probing of viable single muscle fibers at high frequencies (GHz) that had not previously been achieved [130]. Using impulsive Brillouin with picosecond pulses to study the fast processes in proteins, Brillouin studies of heme proteins was performed [131, 132].

It was not until 2005 that Brillouin scattering was applied to multi-dimensional imaging. Koski and Yarger obtained a two-dimensional Brillouin image of a solid-liquid interface with 20 μm spatial resolution with 10 second per pixel acquisition time [133]. This presented Brillouin scattering as not just a spectroscopy, but as a microscopy with much potential applications for biomedical imaging. For instance, two years later, three-dimensional imaging of a mouse eye *in situ* was obtained with only 0.5 second acquisition times [5]. This drastic reduction in acquisition time is a result of the implementation of a VIPA [134, 135], as discussed earlier. Then in 2012, *in vivo* Brillouin microscopy of the human eye was performed with only 0.4 second acquisition times [108]. However, Brillouin scattering microscopy was used not only for bulk biological samples, but at the cellular level as well. Since 2008, its use in cellular imaging, particularly subcellular imaging, has received much attention. Subcellular Brillouin microscopy has been realized using picosecond photoacoustic generation [136, 137]. All the samples above are either transparent or so thin diffuse scattering is not an issue. But for thick, highly diffuse scattering samples this is a problem since signal is proportional to the signal volume. If only a frequency shift is needed, such as studying a samples change with temperature, and depth microscopy is not needed, use of picosecond ultrasonic techniques (the same principle method for subcellular imagine above) provides a way around diffuse scattering. Through this method, Brillouin scattering of media with strong diffuse scattering is accomplished by generating the strong but short lived sound wave at the boundary of the sample by a pump beam, so the

signal from the probe originates from a distance of around one micrometer. This method has been demonstrated in bovine whole milk [138]. It should be noted that Brillouin scattering has also been used to measure the elasticity of some viruses [139, 140], but imaging at such small scales is not feasible with the methods above due to the diffraction limit. However, through the use of plasmonic nanostructures, intense, highly localized sound waves are produced which provide the potential for submicron Brillouin imaging [141-144].

Due to many improvements in experimental equipment and design, as discussed above, the possible use of Brillouin scattering as a clinical diagnostic tool has been considered. The most straightforward approach is to directly exert Brillouin spectroscopy onto transparent/translucent biofluids. For example, we performed a preliminary experiment using Brillouin spectroscopy to screen for increased total protein in cerebrospinal fluid (CSF) during bacterial meningitis [109]. Traditionally, diagnosis of bacterial meningitis is a challenging task for most physicians due to the non-specificity of symptoms, particularly in small children [145]. Rapid diagnosis and immediate treatment with antibiotics would greatly reduce the mortality rate [146], however most existing diagnostic techniques are either slow (such as bacterial cultures, which require at least 24 hours [147]) or destructive to at least a portion of the CSF sample [148]. Nevertheless, in virtually all cases of bacterial meningitis, protein concentrations in the CSF are elevated [149]. As the protein concentration of a solution changes, the elasticity of the fluid would change accordingly [150], and can be characterized by spontaneous Brillouin spectroscopy. The current results showed that elevated protein levels in CSF altered the liquid's Brillouin shift by ~ 100 MHz [109]. This is enough for detection using Brillouin spectroscopy with ~ 60 MHz resolution. Unlike other techniques (biuret methods, dye-binding techniques, and nephelometry), Brillouin spectroscopy offers a possible method of quantifying total protein concentration without alteration of the fluid obtained from the body, representing a powerful simplification over most current techniques.

To date, background-free spontaneous Brillouin spectroscopy [105], due to its high extinction ratio, is found to be suitable for imaging/characterizing many types of biological tissues. Examples include bones [151], skin [152], muscle [151], and atherosclerotic-induced plaque [110, 153]. More recently, Brillouin spectroscopy has also been extended to characterize the mechanical properties of biocompatible materials [154]. In this dissertation, some of the most recent applications of Brillouin spectroscopy/microscopy, including cellular/tissue /whole-body level imaging/sensing, are presented in the next few chapters.

CHAPTER II

EXPERIMENTAL INSTRUMENTATION *

Many technical challenges exist when extending Brillouin spectroscopy to the field of biomedical imaging. The most critical challenge is to separate the Brillouin components from elastic scattering components, including those induced by Rayleigh and Mie scatterings. The small frequency shift (1~30 GHz) in Brillouin scattering process imposes a spectral resolution to be less than 1 GHz and a resolving power to be greater than 10^6, which standard diffraction-grating-based spectrometers are unable to achieve [155]. The second challenge in Brillouin spectroscopy is the contamination coming from the parasite background induced by the elastic scattering photons. This background becomes a significant issue when imaging biological tissues, where the strong Mie scattering often saturates the CCD detector. Finally, the weak signal strength of the Brillouin spectroscopy is also a challenge. How to effectively utilize the limited number of Brillouin scattered photons becomes a challenging issue.

In the following sections of this chapter, we first introduce the Virtually Imaged Phased Array, an optical component that is capable of inducing adequate optical dispersion and is suitable to analyze Brillouin spectra. The physical principles governing VIPAs will be described. A VIPA-based Brillouin spectrometer will be discussed in the subsequent sections. Further optimizations and data processing algorithms are presented as well.

---

* Part of this chapter is reprinted with permission from "Background clean-up in Brillouin microspectroscopy of scattering medium" by Zhaokai Meng, Andrew J Traverso, Vladislav V Yakovlev, 2014. Optics Express, 22, 5410-5415, Copyright 2014 by The Optical Society, and "Optimizing signal collection efficiency of the VIPA-based Brillouin spectrometer" by Zhaokai Meng, Vladislav V Yakovlev, 2014. Journal of Innovative Optical Health Sciences, 8, 1550021, Copyright 2014 by World Scientific Publishing Co Pte Ltd.

Finally, the development of the dual Brillouin/Raman spectrometer will be described in detail.

2.1 Virtually Imaged Phased Array (VIPA)

A substantial challenge in Brillouin spectroscopy is to separate the Brillouin component from elastically scattered photons, including those induced by Rayleigh and Mie scatterings. Brillouin scattering usually results a frequency shift (1-30 GHz), which is too small to be resolved by conventional grating-based spectrometers [155]. For example, distilled water typically results a 7.46 GHz frequency shift for Brillouin scattering in room temperature [5, 133], which corresponds to a ~0.0094 nm wavelength difference (assuming the incident wavelength is 532 nm).

Traditionally, Brillouin spectroscopy can be resolved by several complex techniques, including multipass diffraction grating monochromators [99, 156] and heterodyne light beating methods [100, 157, 158]. Besides these relatively complicate techniques, Fabry-Perot interferometers have been mainly engaged in Brillouin spectroscopy thanks to the high angular dispersion [133, 159, 160]. Since the release of piezoelectric stages, the spectrum has been commonly acquired by scanning the optical cavity of the Fabry-Perot interferometer and collected by means of single channel detectors such as high-sensitivity photodiodes and photomultipliers (PMT) [101, 155, 161]. The development of new high-sensitivity multichannel detectors (e.g. CCD and photodiode arrays) has allowed it to operate in a faster non-scanning mode using fixed cavity length FP etalons [162-164]. Furthermore, the general requirement of maintaining a sensible parallelism during the scanning process with a conventional FP interferometer has been overcome [165]. However, despite the high spectral resolution, both scanning and non-scanning FP interferometers are fundamentally limited by their maximum throughput efficiency, that is inversely proportional to their finesse [159]. Consequently, the high finesse demand in

Brillouin spectroscopy has typically limited the transmission of the input signal to be less than 1%, therefore leading to long data acquisition duration [166] up to several hours.

In this study, in order to overcome the long data acquisition times and simultaneously maintain a high spectral resolution, we employ an optical device named Virtually Imaged Phased Array (VIPA) [134]. With the assistance of VIPA, the insertion loss induced by the dispersive optical component has been substantially minimized. In this sense, the Brillouin scattering photons can be efficiently utilized, allowing fast acquisition of Brillouin signal.

The theoretical model and the typical optical arrangement of VIPA are shown in Fig. 6. The VIPA etalon is conceptually similar to a tilted Fabry-Perot etalon [135]. It has three different coating areas. The front surface has a highly reflective (HR) coating (R_1>99%), as well as a small area with anti-reflection (AR) coating, through where the input optical beam is coupled. The back surface has a partially reflective coating (R_2~95%). As shown in Fig. 6, the input beam is focused into the VIPA by a cylindrical lens and enters the inner space of the VIPA. It is important to align the beam focus close to the boundary between the HR and AR regions to minimize the tilt angle while minimizing insertion loss. Inside the VIPA, the beam undergoes multiple internal reflections and produces an array of output beams with increasing phase delays. The VIPA is so named due to the similarity of the device's operation with that of a series of multiple virtual sources interfering with each other as in a phased array. The interference among the phased array of beams provides large angular dispersion so that different frequency components are emitted at different angles. A spherical lens translates the angular separation into a spatial separation in the plane of a CCD camera.

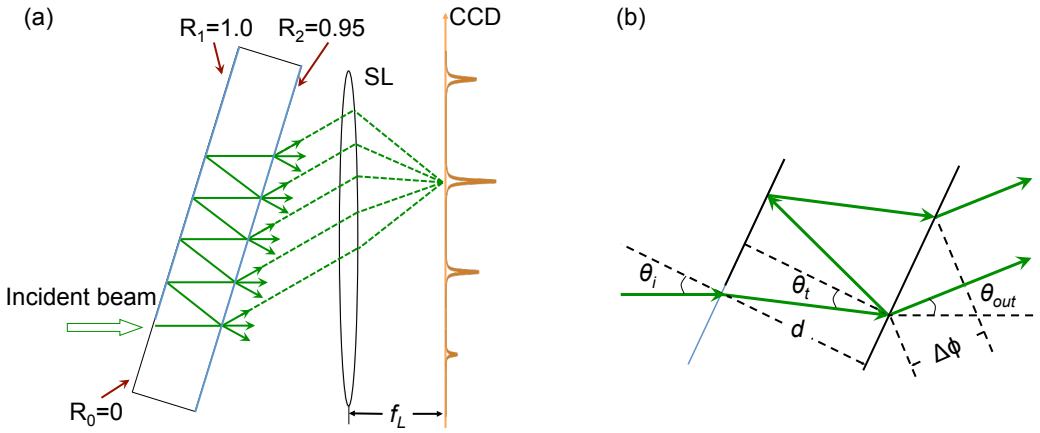

Figure 6 Illustration of VIPA's theoretical model.

The optical path length between the two output orders is $2L\tan(\theta_{in})\sin(\theta_i+\theta_{out})$. Here θ_i is the tilting angle of the VIPA, θ_{out} is the output angle. According to the Snell's Law, $\frac{\sin(\theta_i)}{\sin(\theta_{in})}=\frac{1}{n}$, where n is the refractive index of the VIPA spacing material. Therefore, the condition of constructive interference can be written as:

$$2kL\left[\frac{n}{\cos(\theta_{in})}-\tan(\theta_{in})\sin(\theta_i+\theta_{out})\right]=2m\pi \tag{2.1}$$

where $k=\frac{2\pi}{\lambda}$ and m is an integer. Correspondingly, the free spectral range (FSR) can be derived:

$$\mathrm{FSR}=\frac{c}{2L}\left[\frac{n}{\cos(\theta_{in})}-\tan(\theta_{in})\sin(\theta_i+\theta_{out})\right]^{-1} \tag{2.2}$$

The electrical field contributed by m^{th} order virtual image is $E_m=E_0(R_1R_2)^m$. Here R_1 and R_2 are the reflectivity of the front and back side coatings. By placing a spherical imaging lens behind the VIPA, the angular dispersion can be turned into spatial dispersion, and the interference fringes can be imaged:

$$I(x,\lambda) \propto \exp\left(-\frac{2f_1^2x^2}{f_2^2W^2}\right)\frac{1}{\left(1-R_1R_2\right)^2+4R_1R_2\sin^2\left(\frac{\pi\delta}{\lambda}\right)} \tag{2.3}$$

where f_1, f_2 are the focal length of the cylindrical lens and imaging lens, respectively [167, 168]. x is the distance between the interested point and the axis of the imaging lens. The phase delay δ can be written as:

$$\delta = L\left(2\cos(\theta_{in})-2\tan(\theta_{in})\cos(\theta_i)\theta_\lambda-\frac{\cos(\theta_{in})\theta_\lambda^2}{n}\right) \tag{2.4}$$

Here paraxial approximation $x/f_2 \approx \theta_\lambda$ is used. The typical output of a VIPA is plotted in Fig. 6 as well.

For the VIPA system, it is important to ensure the incident beam to be located in the boundary between the HR and the AR interface, i.e., R_0=0 area. Meanwhile, the first order reflection should be located at the R_1=1.0 area. Therefore, a restraint of θ_i should be applied:

$$L\tan\left(\frac{\theta_i}{n}\right) \geq \omega_0\sqrt{1+\left(\frac{L\lambda}{n\pi\omega_0^2}\right)^2}\ . \tag{2.5}$$

In our case, the incident wavelength can be set as 532 nm or 780 nm. In the 532 nm system, the parameters of the VIPAs are: R_1=99.5%, R_2=95%, L=3.0916 mm, fused silica spaced (n=1.457021). Therefore, the FSR for this VIPA is 33.3 GHz. Here we assumed that the input and output angles are both close to 0 degree.

Fig. 7 presents the output of the VIPA as a function of the tilting angle θ_i ranges between 0.5° to 1.0°. The peaks get narrower when θ_i increases. Correspondingly, the spectral resolution decreases, since the spectral range corresponding to a single CCD pixel decreases. Therefore, when θ_i decreases, the spectral resolution of the entire system increases. However, this small tilting angle usually goes over the restriction

provided by Eqn. (2.5), the throughput efficiency correspondingly decreases. Thus there is a trade-off between the spectral resolution and the efficiency.

Figure 8(a) illustrates the optical arrangement for the VIPA as a tool to separate Brillouin scattering signal from the elastic scatterings. Note that the incident light contains both Brillouin signal and elastically scattered photons. Due to the dispersion induced by the VIPA, the Brillouin signals, including the Stokes and the anti-Stokes signals, can be separated from elastic signals (green dots). Experimentally, the separated signal will be collected by a detector array, such as a CCD camera.

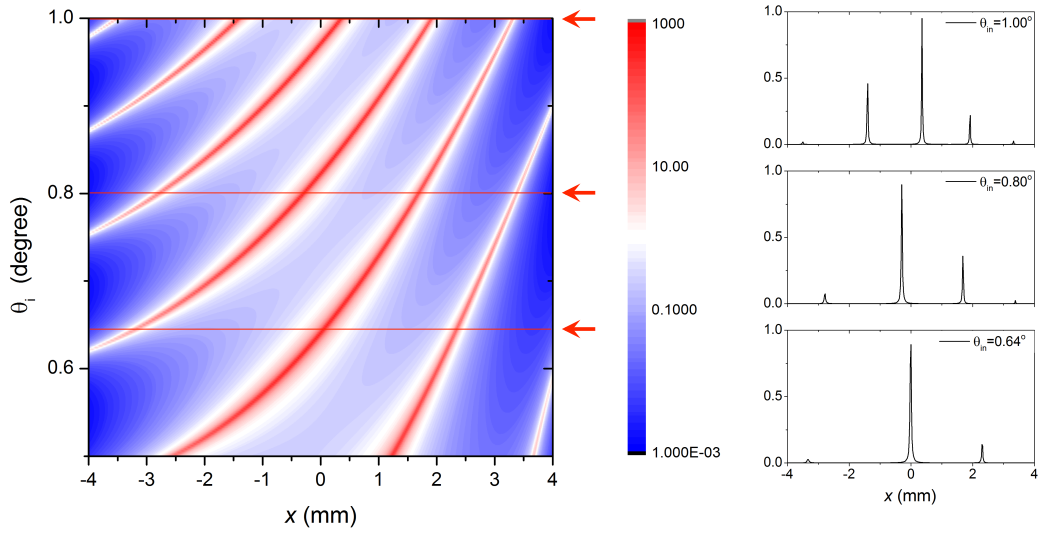

Figure 7 Output of the 532 nm VIPA as a function of VIPA tilting angle and the position at the focal plane. The color-coding refers to the output intensity. The tilting angle θ_{in} ranges from 0.5° to 1.0°. Three tilting angles, 0.64°, 0.80° and 1.00° are specifically calculated and shown in the right.

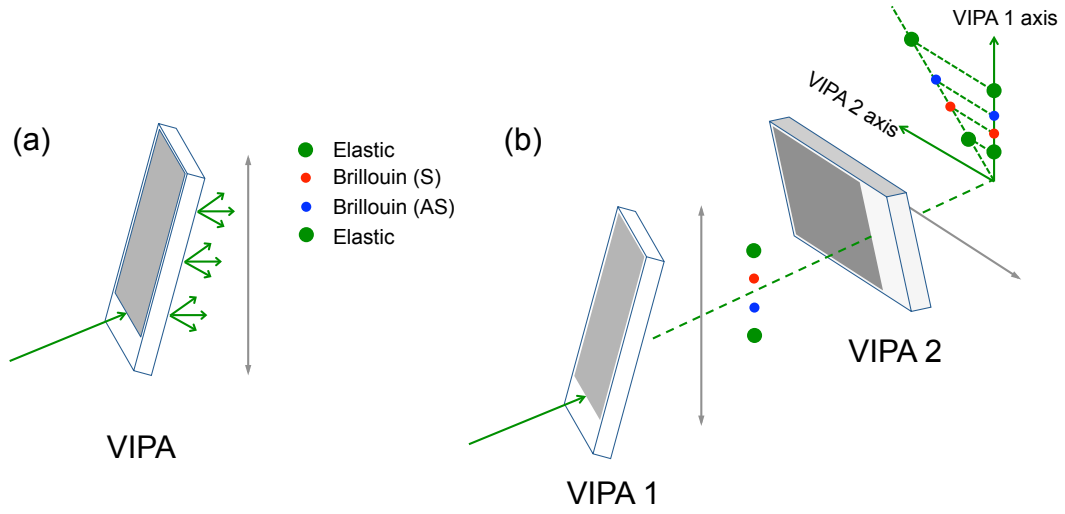

Figure 8 Illustration of (a) One-stage VIPA spectrometer, and (b) Two-stage VIPA spectrometer. S: Stokes; AS: ant-Stokes.

Although a single VIPA is sufficient to distinguish photons with different frequencies in theory, it is usually difficult to avoid stray light and unwanted elastic scatterings. Inspired by the optical arrangement of the cross-axis cascading diffraction gratings, Scarcelli et al. developed a two-stage VIPA arrangement. The cross-axis cascade approach offers a simple way to separate and filter out the stray light from the spectral signal after each stage and thereby to reduce the background and crosstalk substantially.

Fig. 8 compares the principle of single stage VIPA and the cross-axis cascade VIPAs. In the first stage arrangement, the VIPA is aligned along the vertical direction and the spectral pattern is dispersed vertically. When the sample is not transparent or when there are strong optical reflections, the elastic scattering component increases dramatically. If the ratio between elastic scattering (dark-green circles) and Brillouin scattering (light-green circles) exceeds the spectral extinction of the spectrometer, a crosstalk signal appears along the spectral axis (green line). This “stray light” can easily overwhelm the weak Brillouin signal.

Experimentally, due to diffractions and limitations induced by optical components, the light beam cannot perfectly follow the paths shown in Fig. 8. A portion of incident photons turns into “stray light”, and contaminates the useful signals. This pheromone is even worse when testing the tumid liquids, as Mie scattering dominates and the number of stray light photons significantly increases. Scarcelli and Yun [102] proposed a multistage VIPA setup to overcome this difficulty. An illustration of two-stage VIPA spectrometer is shown in Fig. 8.

2.2 Instrumentation of the VIPA-Based Brillouin Spectrometer

In this section, the optical arrangement of the VIPA-based Brillouin spectrometer is described at the system level. The setup is shown in Figure 9. The setup is inspired by the optical arrangement of a typical confocal back-scattering microscope. A 532-nm single mode solid-state laser (Lasermate Group Inc.; model: GMSL-532-100FHA) was employed as the source of incident radiation. The center wavelength is specified as 531.9587 nm ± 0.3 pm with its maximum output power at ~100 mW. The nominal output linewidth for this pump source is ~ 640 kHz. An optical isolator (Electro-Optics Technology, Inc., Model: BB-8-05-I-090) prevented unwanted feedback from the rest of the optical set-up. A non-polarizing 50/50 beam splitter was placed in the beam path to reflect the backscattered light towards a single mode fiber (Fibercore Inc., Model: SM600, length: 1 m). An infinity-corrected microscope objective lens (Nikon Inc., CFI Plan Fluor 20x, N.A.= 0.5) served to both focus the pump onto the sample and collected the back-scattered light. The power at the sample was adjusted to be less than 40 mW for all the measurements. The sample solution was placed in a quartz cuvette (Starna Cells Inc.). The output of the fiber was coupled into a single stage or 2-stages VIPA spectrometer.

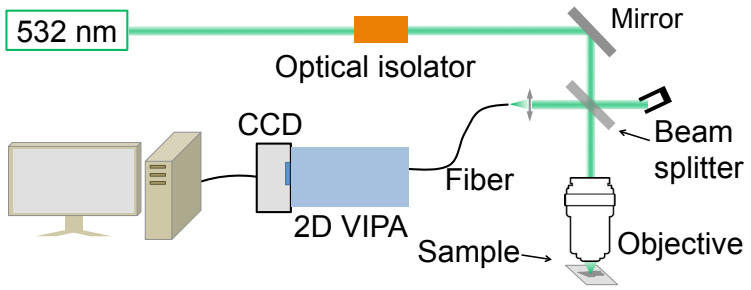

Figure 9 The basic optical arrangement of VIPA-based Brillouin spectrometer.

Fig. 10 depicts the 2-stage VIPA spectrometer in greater detail. The fiber output was collimated by a positive lens. The rest of the 2-stage VIPA spectrometer followed the design set forth by Scarcelli and Yun [102], and is already described in Figure 8. The VIPAs (Light Machinery Inc., model: OP-5642) were specifically designed for 532-nm applications with a nominal free spectral range (FSR) of 33.3 GHz. A lens (focal length 1000 mm) was used after VIPA2 so that the Brillouin component and elastic component were well separated. To minimize the parasitic diffraction, optical lenses with large diameters (2-inch) were used within the VIPA spectrometer. A computer-controlled CCD camera (Moravian Instruments, Model: G2-8300) was placed at the focal plane to collect the images. A single-stage VIPA spectrometer (not shown in the figure) was used to characterize the iodine cell's extinction efficiency, which was accomplished by removing the second VIPA (VIPA2) and its corresponding cylindrical lens, while maintaining the rest of the optical setup.

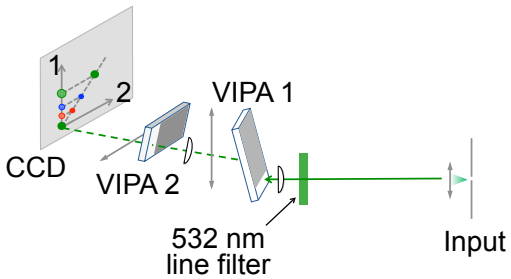

Figure 10 The detailed optical arrangement of a 2-stage VIPA-based Brillouin spectrometer.

2.3 Background Clean-up in Brillouin Spectroscopy of Scattering Medium

In Brillouin spectroscopy, the measured frequency shifts are small (in the range of GHz). In the previous section, by taking advantage of single- or multi-stage virtually imaged phased array (VIPA [135]), Scarcelli and Yun employed Brillouin spectroscopy to acquire 2D *in-situ* images of translucent biological tissues [102, 169]. Compared with conventional scanning Fabry-Perot interferometers, VIPA spectrometers enable better signal-to-noise ratio over a shorter acquisition time, while maintaining good spectral resolution [133].

However, a relatively weak signal level makes Brillouin scattering difficult to be distinguished from the elastic scattering background. This becomes a significant issue when imaging biological tissues, where strong elastic scattering often saturates the CCD detector. Moreover, this problem is further compounded when paired with the usual imperfections of a typical optical setup, which often couples in stray light and diffracted beams. Scarcelli and Yun [102] addressed these difficulties by introducing a multi-stage VIPA setup, which provides an additional 25 dB of background suppression. However, in most practical applications involving confocal imaging of highly scattering samples, even stronger background suppression is necessary. One possible strategy to surmount this problem would be to add additional VIPAs, and, while this would reduce the background, it would also further complicate the optical setup as well as significantly reduce the useful Brillouin signal. It would be highly desirable to employ a very narrow notch filter prior to the VIPA spectrometer, allowing only inelastic components to transmit.

In this section, we demonstrate that gaseous absorption cells are capable of acting as the desired notch filters, thus making VIPA-based Brillouin spectrometers simpler and more efficient. If the incident radiation is in a resonance with a narrow-band atomic or molecular transition, selective absorption will reduce the transmitted intensity of the

incident light, leaving the off-resonant radiation mostly unperturbed [170]. The excited molecule can then decay by spontaneous fluorescent emission or other non-emitting mechanisms. Compared to the incident photons, the emitted photons can often be less energetic and are likely to propagate in random directions. For this study, we chose iodine vapor due to the many vibronic transitions around 532 nm from the ground state, $X^1\Sigma_g^+$, to the 2nd excited state, $B^3\Pi_{0u}^+ B^3\Pi_{0+u}$, where the typical linewidth for a transition is less than 0.05 cm^{-1} (<1.5 GHz) [171], which is perfectly suitable for Brillouin spectroscopy. We note that the atomic/molecular absorption cells were first employed in Raman and Brillouin spectroscopy applications in the 1970s [172, 173] and have been in use throughout the 1980s and 1990s. For example, the iodine absorption cell was employed when measuring low-frequency Raman shifts [174], and a rubidium absorption cell was used in Fourier transform Raman and Brillouin spectroscopy [175]. In this study, we, for the first time, utilize a VIPA spectrometer in conjunction with a molecular absorption cell, which allows the acquisition of *in-vivo* mechanical property specific microscopic images. In this report, for the sake of simplicity, we only demonstrate spectroscopic applications to illustrate the proof of principle.

2.3.1 Experimental setup

Fig. 11(a) portrays the basic experimental arrangement of the new system. We adopted the basic setup from the system described in Fig. 2.4. The new setup of the 2-stage VIPA spectrometer is depicted in Fig. 11(b) in greater detail. Unlike the previous setup, the fiber output was collimated by a positive lens and coupled to a 75-mm long cylindrical-shaped (25.4-mm diameter) iodine absorption cell (Opthos Instruments, Inc.). No buffer gas has been added into the cell. The vapor pressure was controlled through the cell's temperature, which was monitored by K-type thermocouples. A 532-nm line filter was placed behind the iodine cell to filter the undesired spontaneous emissions coming from

the gaseous cell. The rest of the 2-stage VIPA spectrometer followed the previous design [102].

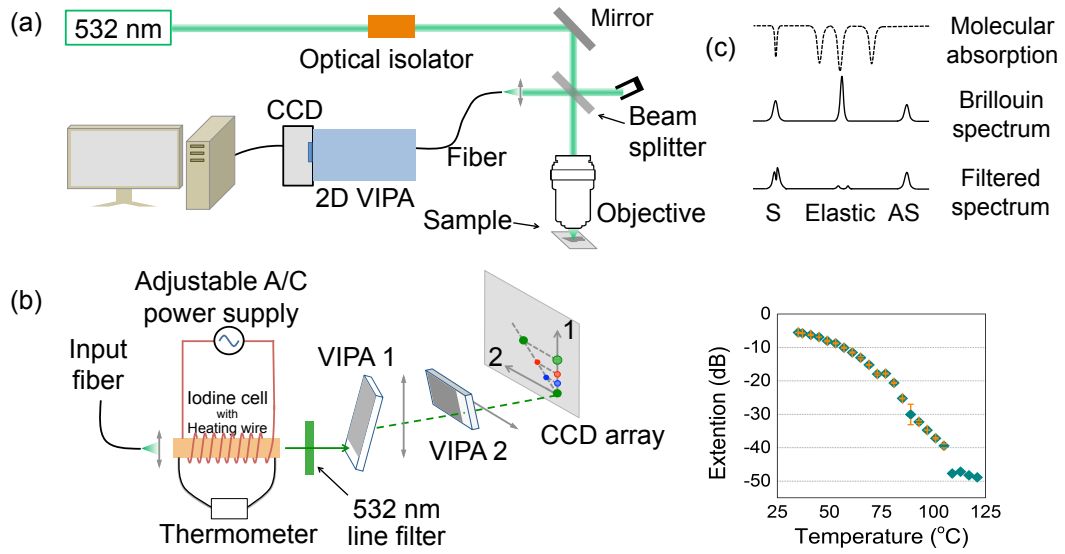

Figure 11 (a) Schematics of the experimental setup. (b) A more detailed illustration for the 2-stage VIPA spectrometer. (c) (Top) A conceptual diagram showing the working principle of a molecular absorption notch filter; here the absorption band suppresses the Rayleigh scattered light, where "S" and "AS" denote the Stokes and anti-Stokes components, respectively; (Bottom) the measured extinction of the iodine cell as a function of temperature.

Fig. 11(c) illustrates both the fundamental principle of the molecular absorption cell, and its extinction properties as a function of temperature. Here, the wavelength of our pump laser coincides with absorption line 660 (18793.205 cm^{-1}) as noted in Ref. [171]. In this way, the iodine vapor is optically thick for the elastically scattered photons, while optically transparent for Brillouin scattered photons in most cases. There is also a possibility that one of the Brillouin components (Stokes or anti-Stokes) coincides with another absorption band, such as the situation shown in Fig. 11(c). For example, the anti-Stokes peaks may hit absorption lines 661 and 662, which correspond to ~ 5.87 GHz and ~ 8.24 GHz in frequency. The Stokes peaks may be absorbed by lines 659 and 658, equivalent with ~ 2.65 GHz and ~23.32 GHz in frequency. However, it is unlikely that

the Stokes and anti-Stokes peaks are simultaneously and strongly affected by the iodine vapor, unless the heating temperature is relatively high (> 70 °C), and Doppler and pressure broadenings become severe. The Brillouin shift could still be measured from the unattenuated peak.

To verify the extinction ability of the iodine cell, we measured the extinction efficiency as a function of the iodine cell temperature. The iodine cell was heated up to 150 °C, and cooled ambiently at a cooling rate less than 2 °C / min. The transmitted power decreased as the iodine cell was heated due to the increase in the iodine vapor density. The power suppression was over -50 dB when the iodine cell was heated above 100 °C, where absorption line broadening dominates (e.g., Doppler broadening and pressure broadening [176]).

2.3.2 Preliminary test results

We first tested the capabilities of the 2-stage VIPA spectrometer both with and without the assistance of the iodine cell. The results are shown in Fig. 12 (a) and (b). Here, we chose acetone as the sample, and an integration time of 20 s was used for both acquisitions. In Fig. 12 (a), the Brillouin components were well separated from the elastic components, but the elastic component and the surrounding pixels give relatively strong signal. To the contrary, with assistance of the iodine cell, the elastically scattered component was substantially absorbed as shown in Fig. 12 (b), though still remained visible as a reference.

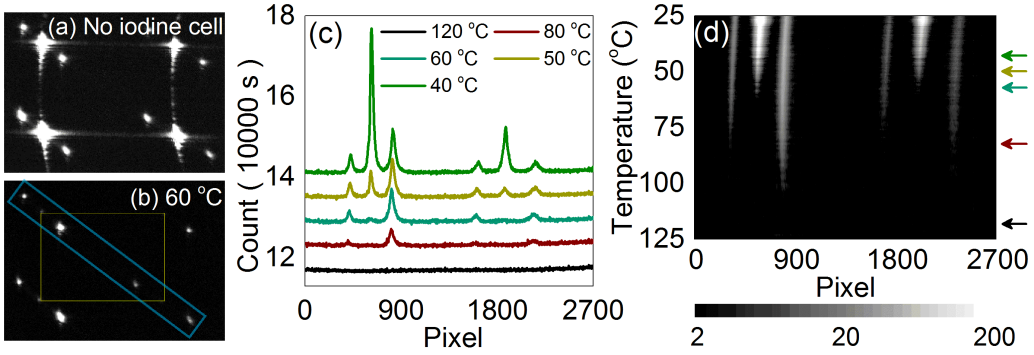

Figure 12 (a) The CCD image of the VIPA spectrometer for acetone, without the iodine cell (35 mW, 20 sec); (b) The CCD image for acetone, with the iodine cell heated at 60 °C (35 mW, 20 sec); (c) Quantatitive pixel readings within the blue box shown in (b); (d) Contour plot of the same data in (b). The data plotted in (c) are indicated with arrows.

Fig. 12 (c) and (d) depicts the suppression efficiency as a function of the iodine cell temperature. For this experiment, we heated the iodine cell to over 150 °C, and let it cool down naturally. A small rectangular box of the CCD image was selected along the diagonal line shown in Fig. 12 (b). The pixel readings were interpolated and added along the direction of the short edge of the rectangle. Fig. 12 (c) shows the results at some typical heating temperatures. For temperatures below 60 °C, two periodic triplet structures are apparent within those plots, where each of those triplet structures contains the elastically scattered components (central peak), as well as the anti-Stokes (left) and Stokes (right) components for Brillouin scattering. The intensity of both the Rayleigh and Brillouin components decreased with increasing temperature. However, the Rayleigh component is suppressed much more strongly and more quickly as the temperature increases. At 60 °C, the elastically scattered peak was almost unnoticeable, leaving only the Brillouin peaks. Fig. 12 (d) summarizes the data shown in Fig. 12 (c) and extends it to other temperatures. Due to the absorption line broadening, at the temperatures above 110 °C, all the spectral components disappear below the noise limit of our detection. The Stokes component is still discernable at 100 °C, whereas the anti-Stokes peak, which partially overlaps with one of the absorption lines, disappears above ~ 75 °C. In contrast, the elastic component disappears above ~ 60 °C. Due to a slight

wavelength drift of the laser source, the position of the Brillouin and elastic peaks do not remain the same during the entire experiment. The 40 °C data was taken 40 minutes later than the 100 °C data. A 16-pixels drift has been identified between them, which corresponds to ~ 370 MHz in frequency.

The presence of elastic scattering significantly complicates the situation. To induce some scattering, we added some coffee cream (mainly, lipid droplets in water) to dimethyl sulfoxide (DMSO). With as little as 4 μL of coffee cream added to 4 mL of DMSO, the solution became highly scattering, as shown in Fig. 13(a). Fig. 13 (b) and (c) show the Brillouin scattering results for the mixture. To minimize absorption, we positioned the focal plane of the objective at the cuvette-sample interface. As shown in Fig. 138 (b), the CCD reading for the two-stage VIPA spectrometer without the iodine cell shows substantial background. In contrast, Fig. 13 (c) shows a CCD image with the assistance of the iodine cell, which was kept at ~ 80 °C. The contamination of elastically scattered photons was reduced, and the Brillouin peaks are clearly shown. Fig. 13 (d) quantitatively illustrates the ratio between the elastic and Brillouin signals as a function of the iodine cell's temperature. Here, the signal strength refers to the total number of photons for each peak. For all samples, this ratio decreases with the increasing temperature.

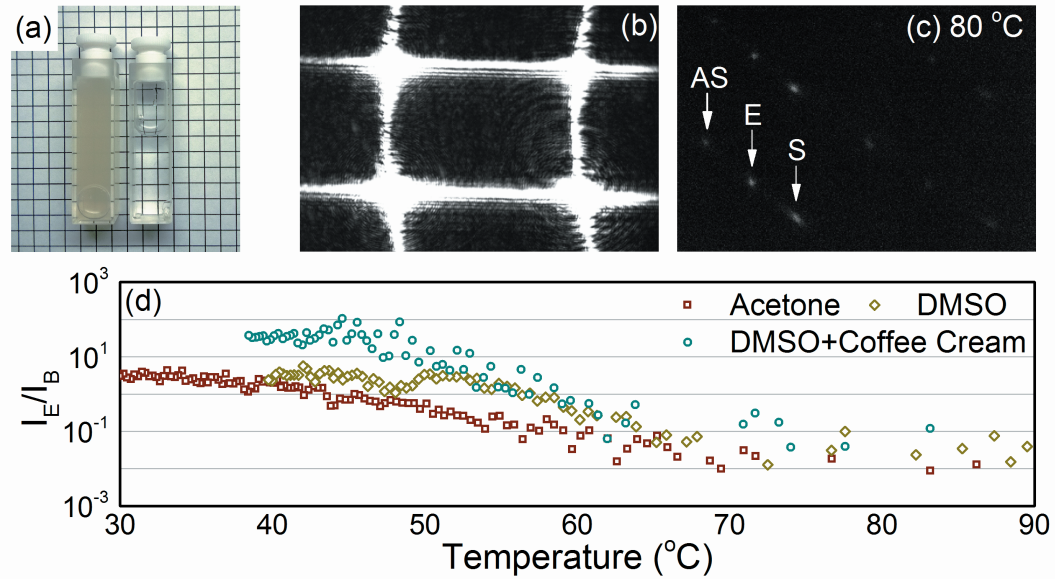

Figure 13 (a) Pure DMSO (right) and DMSO with 4 μL coffee cream (left). (b, c) The CCD readings of the 2-stage VIPA spectrometer with (b) and without (c) the iodine cell. (d) The signal ratio between elastically scattered and Brillouin scattered components.

The single-stage VIPA setup was also tested. Figs. 14 (a) and (b) shows the CCD images of the single-stage VIPA spectrometer with a 2 s integration time. Here, three heating temperatures were tested: 120 °C, 80 °C, and 40 °C. Unlike the 2-stage VIPA, the single-stage VIPA spectrometer has a higher transmission rate [102], making Stokes peak still visible at 120 °C. A dip in the anti-Stokes peak (marked by an arrow) is possibly induced by absorption line 662 of the iodine vapor as noted in [16]. Fig. 14 (b) shows the average signal along the horizontal direction in Fig. 2.9 (a). Based on the Stokes peak, the Brillouin shift was measured to be 8.395 ± 0.008 GHz with a linewidth of 1.674 ± 0.037 GHz, which is in good agreement with previous reports [177]. In the case of the DMSO solution with added scattering agents (coffee cream), the Brillouin components become visible when the iodine cell is heated up to 80 °C. The corresponding Brillouin shift was measured to be 8.535 ± 0.034 GHz with a linewidth of 1.986 ± 0.219 GHz.

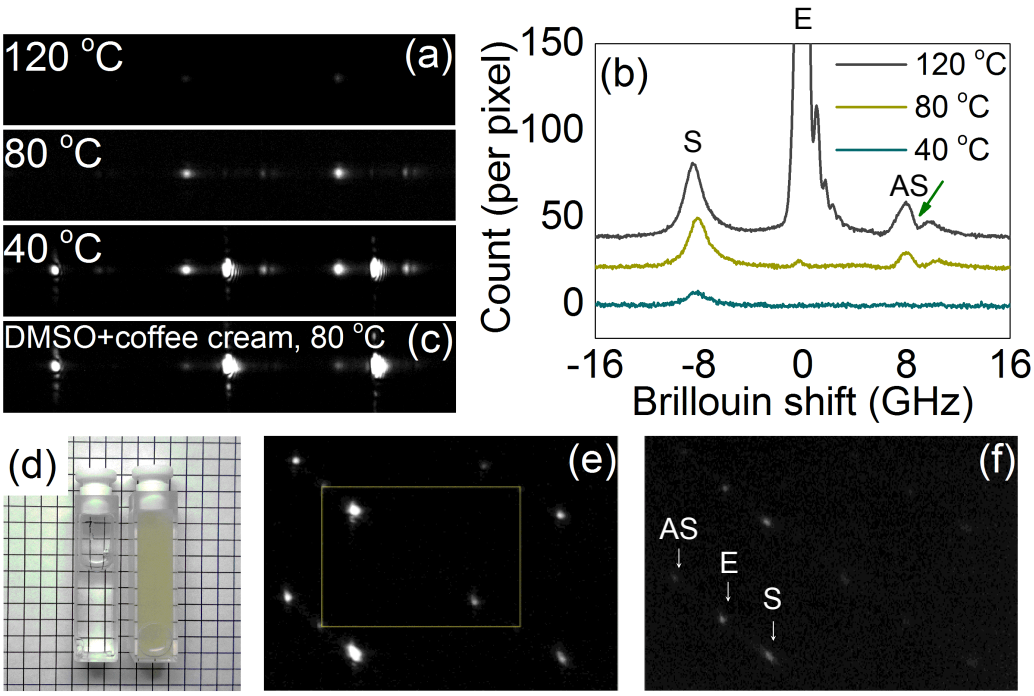

Figure 14 (a-b) The CCD image of the single-stage VIPA spectrometer for pure DMSO; the Brillouin shift is 8.320 ± 0.008 GHz, with a linewidth (FWHM) of 1.745 ± 0.035 GHz. (c) The single-stage VIPA spectrum for the DMSO solution with added scatterers.

2.3.3 Discussion

The recent development of VIPA spectrometers has greatly enhanced the signal acquisition efficiency and simplified the Brillouin spectroscopy setup. In this section, we have successfully demonstrated that molecular absorption cells can be implemented as valuable notch filters in VIPA spectrometers. The background associated with elastic scattering is substantially lowered, and the relatively weak Brillouin peaks are easily identifiable. With the assistance of molecular absorption cells, Brillouin spectroscopy could be used to study turbid samples, including collagen fibers, bones [178], high density lipid solutions, and blood [102]. Moreover, when utilizing absorption cells, single-stage VIPA spectrometers are capable of characterizing turbid samples; this reduces acquisition time and substantially simplifies the optical system.

The use of absorption cells as notch filters could be extended to other pump wavelengths. For example, rubidium vapor provides absorption lines at 780 nm and 795 nm, while potassium vapor is highly absorptive at 764 nm and 770 nm. These wavelengths are ideal for biomedical applications as they are well within the transparency window for optimized penetration depth for living organisms. However, the iodine vapor provides the highest figure of merit among popular atomic/molecular filters (e.g., I_2, Hg, Cs, Pb, Ba, K, etc.) [179].

The application of absorption cells requires strict stabilization of the laser source. The solid-state laser source employed in this study showed satisfied short- and long-term stabilities. For future routine uses, the diode laser sources are preferred, due to their superior tunabilities and stabilities. The frequency locking procedures will be performed for further stabilization [25].

In this demonstration, the absorption bands for molecular iodine vapor are densely distributed around the pump wavelength (~ 532 nm). Therefore, Brillouin peaks are likely to be absorbed, which would affect the shape and accurate identification of those peaks. To calculate the exact Brillouin shift, a full knowledge of the absorption spectrum for the absorbing agent is required. This can be studied with tunable diode lasers with ultrahigh spectral resolutions. As a result, compensating algorithms can be established, and the Brillouin shift can be determined with better accuracy.

2.4 Precise Determination of Brillouin Scattering Spectrum Using VIPA Spectrometer and CCD Camera

In previous sections, the experimental instrumentation of Brillouin microspectroscopy, have been introduced in detail. However, due to the limited adoption of Brillouin spectroscopy and VIPA spectrometer, retrieving Brillouin spectral information from the VIPA output has not yet been extensively studied.

During the past decade, the dispersion law of VIPA spectrometers have been carefully evaluated using plane wave approximation [180] as well as Fresnel diffraction theory [167, 181]. Typically, the output of a VIPA spectrometer can be described by a Lorentzian function, given the incident light source is spectrally narrow compared to the free spectral range (FSR) of the VIPA [167, 181]. Compared with more conventional Fabry-Perot (F-P) etalons, the VIPA spectrometer results in a more complex interference output at the detection plane [134, 167]. Retrieving methods (e.g., [163, 182, 183]) designed for F-P etalons cannot be directly extended to the VIPA spectrometers. A common strategy of retrieving the Brillouin shift from the VIPA spectrometer output is to compare the spectra with those of known samples, including water and PMMA [184]. Precise retrieving the Brillouin shift, which is solely based on the sample's VIPA output, remains a challenging task. Moreover, when atomic / molecular absorption cells are employed as narrow-band notch filters, Brillouin signal is often affected by the additional absorption bands induced by the molecular or atomic absorption at the nearby transitions (e.g., [105, 106]). As a result, the experimentally detected Brillouin peak can no longer be described by the Lorentzian shape, which is valid in absence of the absorption cells [167, 181]. This phenomenon induces additional difficulties in retrieving the Brillouin shift. On the other hand, the precise determination of Brillouin shift and linewidth is essential in many applications [163, 182, 183]. For example, the 20-MHz uncertainty in the Brillouin shift would result in ~1 °C inaccuracy in

temperature sensing [185]. Previous studies also indicate that quantifying Brillouin shifts' variations below 200 MHz are essential in understanding the elasticity of the cornea and lens in human eyes [184].

The overall goal of this report is to find a simple and robust procedure to determine the Brillouin shift from the CCD output of a typical VIPA spectrometer containing absorptive notch filter. In this method, the signal contamination resulted by the vapor absorption has been effectively compensated. A sub-pixel accuracy could be achieved, and the final accuracy of the measured Brillouin shifts is sufficient to provide a very good agreement with previous theoretical/empirical predictions (e.g., [185]). The Brillouin linewidth shows the same trend as previous predictions though its absolute value is affected by the experimental setup, which used a tight focusing geometry [186].

2.4.1 Experimental setup

In the studies covered within this section, we adopted the experimental setup as described in section 2.3 (see Fig. 11).

2.4.2 Theoretical considerations

2.4.2.1 Converting pixel number into Brillouin shift

The simplified model of the VIPA-based spectrometer is shown in Fig. 15. A VIPA is equivalent to a tilted etalon. The front side of the VIPA is coated with a highly refractive coating ($R_1 \cong 1.0$), and a small entrance window on one side of the etalon is fully transparent (R_0=0). The backside of the VIPA is coated with the reflectivity R_2=0.95

coating. Following the previous studies [167, 168], for a single wavelength input, the output at the focal plane (i.e., at the CCD chip) could be expressed as:

$$A(\lambda,r)=\frac{1}{1+F\sin^2\left(\frac{nk}{2}\left(2d\cos\theta_t-\frac{2dr\tan\theta_t\sqrt{1-n^2\sin^2\theta_t}}{nf_L}-\frac{dr^2\cos\theta_t}{nf_L^2}\right)\right)} \tag{2.6}$$

θ_t is related with the tilting angle of the VIPA. Usually, the tilting angle is less than 2 degrees. $k=\frac{2\pi}{\lambda}$ is the wavevector of the incident light. f_L is the focal length of the focusing lens. r refers to the position at the CCD chip. F is the finesse of the VIPA, which is determined by the reflectivity of the front and back coating of the VIPA, $F=4R_1R_2/(R_1-R_2)^2$. The above Eq. 1 can be rewritten in a simplified empirical form, which expresses the CCD output as:

$$A(\lambda,r)=\frac{1}{1+F\sin^2\left(v\left(b+d\left(r+r_0\right)+e\left(r+r_0\right)^2\right)\right)} \tag{2.7}$$

where, b, d, and e are some unknown parameters. ν is the frequency of the incident beam. Therefore, the positions of the elastic peaks will satisfy the following condition:

$$v_e\left(b+d\left(r+r_0\right)+e\left(r+r_0\right)^2\right)=(m+l)\pi \tag{2.8}$$

where m and l are both integers. In this particular case, m=c/(λ·FSR)≈16934, and l=0, 1, 2, …. (c is the light speed in vacuum). When collecting Brillouin spectrum, the Brillouin peaks show up on both sides of the elastic peaks. Now, let's assume the distance between the elastic peak and the neighboring Brillouin peak to be Δr at the CCD and the Brillouin shift ν_B to satisfy the following expression:

$$\begin{aligned}\Delta v&=\frac{(m+l)\pi}{b+d\left(r+\Delta r+r_0\right)+e\left(r+\Delta r+r_0\right)^2}-v_e\\&=\frac{(m+l)\pi}{b+d\left(r+\Delta r+r_0\right)+e\left(r+\Delta r+r_0\right)^2}-\frac{(m+l)\pi}{b+d\left(r+r_0\right)+e\left(r+r_0\right)^2}\\&\approx B\Delta r+C\Delta r^2+D\Delta r^3+...\end{aligned} \tag{2.9}$$

This expression can be expanded into the Taylor series since Δv is usually much smaller than v_e. Based on the spacing of the elastic peaks, we are enabled to calculate Δr, when

Δv is the integer multiples of the free spectral range (FSR) of the VIPA. For example, the spatial and the spectral distances between peaks #1 and #2 in Fig. 15 (c) are r_{21} and FSR=33.334 GHz, respectively. Similarly, for peaks #1 and #3, their spatial distance is $r_{21} + r_{32}$. Since the spectral distance between peaks #2 and #3 is also FSR=33.334 GHz, the peaks #1 and #3 are spectrally separated by 2×FSR=66.668 GHz. Based on these data, we can find parameters B, C, D… in the Eq. (4). In practice, the distance between different peaks is expressed in terms of pixel numbers. In our experimental setup, the total number of pixels is 1600 using full vertical binning (FVB) setup. A typical pixel-to-spectrum correspondence is shown in Fig. 15 (d). Here we used all the four elastic peaks (the central peaks of the triplet structures) to determine the corresponding relationship which is shown as a curve in Fig. 15 (d).

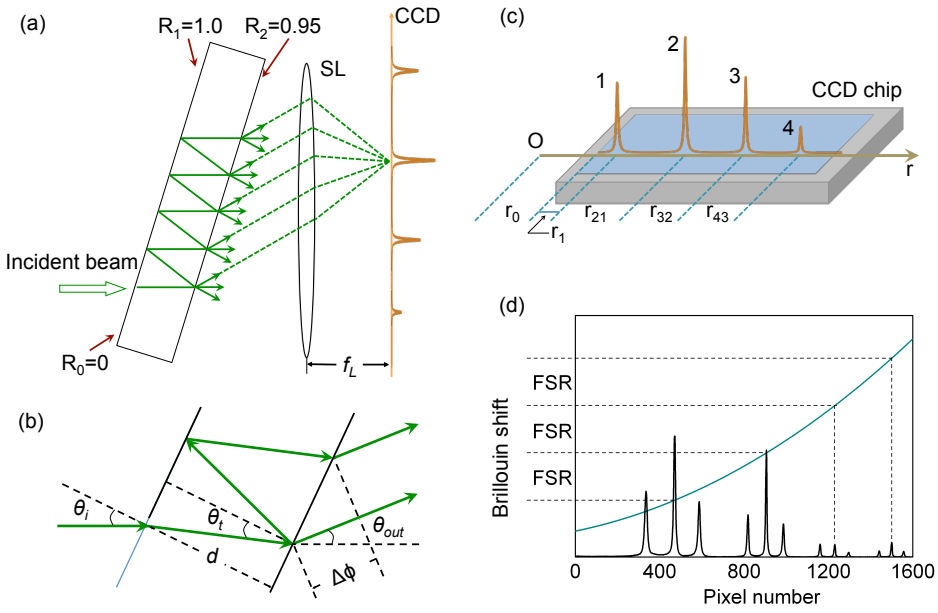

Figure 15 (a) Illustration of the VIPA spectral dispersing geometry; (b) a close-up illustration of the interference geometry of the VIPA; (c) a typical VIPA output on a CCD chip (here we only show the VIPA response for a single wavelength input); (d) the pixel number to Brillouin shift correspondence for a typical CCD output (here we used the 3rd order polynomial interpolation to determine the corresponding relationship). FSR: the free spectral range of the etalon.

2.4.2.2 Compensation of the atomic/molecular absorption

A typical spectrum for Brillouin scattering consists of three parts: the elastic (Rayleigh/Mie) scattering peak, and the Stokes and anti-Stokes peaks for the Brillouin scattering. The acquired Brillouin peaks are expected to follow the Lorentzian shape. A typical Brillouin peak can be expressed as:

$$f(\nu,\nu_B)=\frac{A}{1+\left[2(\nu\pm\nu_B)/(\pi\Gamma_B)\right]^2}+b \tag{5}$$

Here, A is the amplitude of the Brillouin peak, ν_B is the Brillouin shift, Γ_B is the linewidth, and b is the overall background. After transmission through the iodine absorption cell, the collected signal should be a product of the actual Brillouin spectrum and the absorption spectrum:

$$f'(\nu,\nu_B)=g_I(\nu)f(\nu,\nu_B)=\frac{A\cdot g_I(\nu)}{1+\left[2(\nu\pm\nu_B)/(\pi\Gamma_B)\right]^2}+b \tag{2.10}$$

Note that the background is mostly due to the dark current and read-out noise of the CCD detector, so we do not multiply it by the iodine absorption spectrum.

The output wavelength of the excitation laser was found to be overlapping with the iodine absorption line #640 (according to Simmons and Hougen [187]) or #1146 (according to Gerstenkorn et al. [188]). Several additional absorption lines always exist in the surrounding spectral regions; for example, for line #1146, there are lines #1144 and #1145 on the Stokes side, and # 1147 on the anti-Stokes side. There are also some much weaker absorption lines in between lines # 1146 and # 1147. To verify those absorption bands, we recorded the Brillouin spectra of mineral oil, which is sufficiently broad to visualize all the surrounding absorption bands. In our particular absorption cell, the observed line #1147 was located about 10.23 GHz away from the excitation

wavelength. Considering a typical spectral resolution of a VIPA spectrometer, we set the linewidths to be 1.50 – 2.00 GHz (note, that no literature data on the spectral linewidths of those lines are available to the best of our knowledge). All the considered absorption bands are listed in Table 2. The final absorption spectrum of the iodine cell is a summation of all the surrounding absorption lines (Fig. 16 (a)). All the absorption bands, including a small peak in between #1146 and #1147 lines, are taken into consideration. The absorption spectrum can be expressed as:

$$g_I(\nu) = \prod_{i=1}^{n} \left(1 - \frac{A_i}{1 + \left[2(\nu - \nu_i) / (\pi \Gamma_i) \right]^2} \right) \tag{2.11}$$

Table 2 Parameters in the expression of the iodine cell's absorption spectrum

i	**A**	**n (GHz)**	**Γ (GHz)**
1	0.9900	10.236	2.5000
2	0.6000	8.2000	2.0000
3	1.0000	0.0000	1.5000
4	0.9000	-6.9007	2.0000
5	0.9000	-9.3416	1.5000

The effect of the iodine absorption on Brillouin spectra is illustrated in Fig. 16 (b-d). Here we simulate a series of mock Brillouin spectra to prove the principle. In Fig. 2.11 (b), we show a typical Brillouin spectrum with the Brillouin shift of 7.46 GHz (preset shift) and the linewidth of 1.20 GHz (preset linewidth). The Brillouin peaks and the elastic peak are all represented by the Lorentzian functions. Both the original and the filtered VIPA output are plotted in Fig. 16 (b). Although the Brillouin peaks are significantly altered by the iodine molecular absorption, they are still visible. However, the peaks are no longer can be represented by the Lorentzian functions.

In Fig. 16 (c), we simulate more examples with varying value of the Brillouin shift. Here, for simplicity, we only show the anti-Stokes side of the spectrum. When the Brillouin peak overlaps the most with the iodine absorption line, its shape exhibits the most dramatic changes. When the Brillouin shift exceeds 10 GHz, the Brillouin peak is completely split into two parts. If we directly use Lorentzian nonlinear fitting algorithm on those contaminated peaks, the retrieved Brillouin shift will be substantially altered.

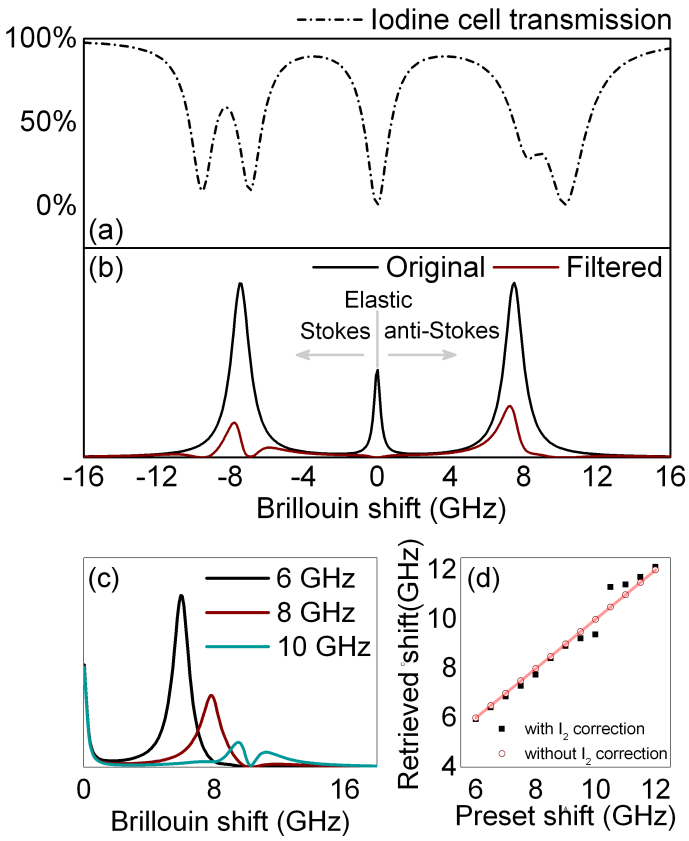

Figure 16 (a) The iodine absorption spectrum around the excitation wavelength. (b) A typical Brillouin spectrum before and after transmitting through the iodine absorption cell (Brillouin shift: 7.46 GHz, linewidth: 1.20 GHz). (c) The filtered Stokes peak for various Brillouin frequencies. (d) The Lorentzian fitting results for the filtered Stokes peaks.

A comparison between the retrieved and preset Brillouin shift is shown in Fig. 16 (d). Taking into account Eqs. 2.9 and 2.10, we employ a Levenberg-Marquardt algorithm to provide a nonlinear least-square fit to the data of the CCD output. Those fitting results are also included in Fig. 16 (d) as red dots. Even when the spectrum is strongly affected by the absorption transitions, the algorithm could still precisely retrieve the Brillouin shift and linewidth. For example, for the 10-GHz Brillouin spectrum, the retrieved Brillouin shift is 9.9941 ± 0.0199 GHz, and the Brillouin linewidth is 1.1981 ± 0.0601 GHz. The uncertainty is even smaller if we process the less contaminated Brillouin peaks. For example, when processing the 6-GHz Brillouin peak, we the retrieved Brillouin shift is 5.9968 ± 0.0034 GHz, and the Brillouin linewidth is 1.1982 ± 0.0122 GHz. Here, we determine the uncertainty by the 95% confidential interval calculated from the Jacobian Matrix. Considering the typical separation between two elastic peaks is ~ 350 pixels in our setup and the FSR is ~ 33.334 GHz, the width of a pixel correspond to ~ 100 MHz in the Brillouin shift, or about 5 times larger than the worst uncertainty obtained using our fitting method.

2.4.2.3 Testing the algorithm on practical experimental results

Next, we applied this method on the real experimental data acquired by the VIPA spectrometer. In this study, we collected the Brillouin spectra of hot water during its cooling process. The initial water temperature was 45 °C, and the final temperature was 20 °C. The water temperature was probed by a commercial food thermometer. Fig. 17 (a) presents typical Brillouin spectra collected at different times after the cooling process began. The excitation power was up to 100 mW, and the integration time was 1 second. The temperature of the iodine cell was tuned to 100 °C, so that the elastic peak could be partially blocked but remained identifiable. The retrieved Brillouin shift and linewidth

are shown in Fig. 17 (b) and (c), respectively. During the retrival process, we assume the environmental temperature was a constant, and neglect the possible frequency drift induced by our DPSS laser. When preparing the data, we utilized the anti-Stokes peaks only, as they are less affected by the absorption band. The Brillouin shift starts to decrease when the cooling process began, and the corresponding linewidth started to increase. These trends satisfy the previous theoretical predictions set forth by Fry et al. [185] and Gao et al. [189]. However, the linewidth in our experiment was broader than the results presented by Gao et al. [189]. This may be due to the limited spectral resolution of the current VIPA setup, as well as some imperfections of the optical alignment. Nevertheless, the Brillouin shift shows good agreement with the previous studies. For example, at 45 °C (0 min), the retrieved Brillouin shift is 7.7154 ± 0.0010 GHz. Meanwhile, according to the empirical expression given by Fry et al. [185], the Brillouin shift should be 7.7250 GHz. By the end of the experiment, the water temperature decreased to 20 °C. The measured Brillouin shift was 7.4448 ± 0.0015 GHz while the empirical prediction is 7.4461 GHz. On the other hand, we also retrieved the Brillouin shift without consideration of the iodine filter. The results are presented in Fig. 17 (b, c) and Table 2. A similar correlation between the temperature and the Brillouin shift/linewidth also exist. However, the absolute value of the retrieved Brillouin shift was greatly altered especially at low temperature (up to 250 MHz). The retrieved Brillouin linewidths were similar with the results with iodine filter correction (Fig. 17 c).

We also utilized the Stokes peaks to retrieve the Brillouin shift/linewidth despite the contamination induced by the iodine absorption. The results are presented in Fig. 17 (d-f) and Tab. 3. Compared with the results obtained from anti-Stokes peaks, we could get similar shifts based on the Stokes peaks. However, the retrieved linewidths did not well agree with the Stokes-based results (Tab. 3), although they still broadened with the cooling down process.

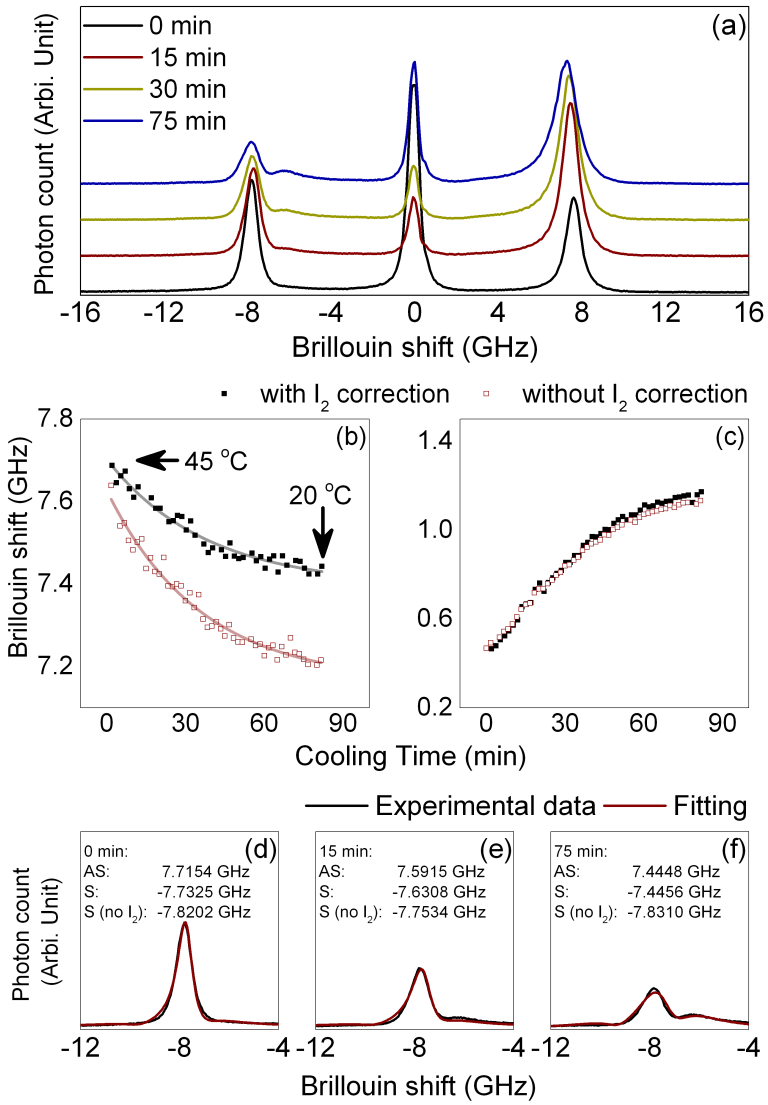

Figure 17 Illustration of the Brillouin spectra acquired during a spontaneous cooling process of hot water. The initial temperature was 45 °C, and the final temperature was 20 °C. (a) The acquired Brillouin spectra at different times. (b-c) The retrieved Brillouin shift and linewidth with and without consideration of the molecular iodine absorption. Here we employed the Stokes peaks only. (d-f) Comparison between the Brillouin shift based on the Stokes and anti-Stokes peaks.

Table 3 Comparison of the retrieved Brillouin shifts and linewidths based on the Stokes and anti-Stokes peaks

Time	Brillouin shift (GHz)		S-AS Difference	Brillouin linewidth (GHz)		S-AS Difference
	Anti-Stokes	Stokes		Anti-Stokes	Stokes	
0 min	7.7154 ± 0.0010	-7.7325 ± 0.0009	0.22%	0.4329±0.0028	0.5030 ± 0.0030	16.19%
15 min	7.5915 ± 0.0012	-7.6308 ± 0.0011	0.52%	0.6644±0.0032	0.6240 ± 0.0033	4.04%
30 min	7.5515 ± 0.0012	-7.6298 ± 0.0022	1.03%	0.8522±0.0033	0.8901 ± 0.0070	4.45%
75 min	7.4448 ± 0.0015	-7.4456 ± 0.0040	0.01%	1.1692±0.0040	1.8118 ± 0.0139	64.26%

2.4.3 Discussions and summary

The introduction of atomic/molecular absorption filters can greatly suppress the elastic scattering background when acquiring Brillouin spectra. With the assistance of these filters, it is now possible to collect the Brillouin spectra for various turbid samples, including many biological tissues [109, 111]. Correspondingly, noninvasive and non-contact assessment of their mechanical properties becomes possible. However, the absorption transitions for many atomic/molecular filters are densely distributed. Therefore, Brillouin peaks are likely to be affected by those lines, which, in its turn, would affect the shape and accurate identification of those peaks. In this report, we implemented the iodine absorption profile into the nonlinear fitting algorithm. The Brillouin shift can be extracted from a sample's Brillouin spectrum without comparison with other known samples.

In this section, we employed the iodine absorption spectrum based on previous publications. We also validated and corrected these results by analyzing the Brillouin spectra using mineral oil, a liquid, which provides a very broad Brillouin peak. However, to further improve the accuracy of this method, a direct acquisition of the absorption spectrum is highly desired. Thus, this approach will be very suitable in a similar configuration employing atomic Rb or Cs vapors as a narrow-band absorber. The

absorption spectrum of those elements is known with a much greater precision, and the linewidths of all the related transitions are known as well (see, for example, http://www.nist.gov/data/PDFfiles/jpcrd705.pdf). Tunable diode lasers may allow for compensation for the pump wavelength drift during data processing, which should further improve the accuracy of data acquisition. Nevertheless, the current absorption profile already allows us to extract the Brillouin shift, which is in good agreement with previous results collected through a much more sophisticated approach and significantly longer acquisition times.

In conclusion, we have demonstrated a simple and efficient Brillouin shift retrieval method suitable for background-free VIPA spectrometer. This method is suitable for acquiring the Brillouin shift and linewidth information based on the background-free VIPA spectrometers. We anticipate the wide use of this method in future applications of Brillouin spectroscopy.

2.5 Optimizing Signal Collection Efficiency of the VIPA-Based Brillouin Spectrometer

Despite the efforts made in previous sections, the limited signal strength is still a critical challenge when extending Brillouin spectroscopy into biomedical imaging/sensing applications. Practically, the weak signal is still highly possible to be immersed in the background. This becomes a significant issue when imaging turbid biological tissues [190, 191]. This problem is further compounded when paired with imperfect optical setups, which are usually polluted with unwanted background noises and signal losses. Scarcelli and Yun addressed these difficulties by introducing a multi-stage VIPA setup, which provides an additional 25 dB of the background suppression [102]. However, in most practical applications involving confocal imaging of highly scattering samples, even stronger background suppression is required. Moreover, the original signal was also weakened via this multistage setup. To induce higher signal-to-noise ratio, one possible strategy is to add additional VIPAs, and, while this would reduce the background, it would also further complicate the optical setup as well as significantly reduce the useful Brillouin signal. Another possibility, increasing the pumping power, is usually highly undesirable for biology-related applications, as the corresponding thermal effect may burn the samples. How to effectively utilize the limited number of Brillouin scattered photons becomes an important problem.

In this section, we specifically investigated the signal loss induced by a single-mode (SM) fiber attached to the VIPA Brillouin spectrometer. We found that due to the insertion loss and the inherent attenuation, SM fiber becomes a significant source inducing signal loss. Further, we replaced the fiber-based setup with an open space setup with a pinhole and found the corresponding signal has been enhanced. We demonstrated that the employment of such a pinhole is helpful in enhancing the sensitivity of the VIPA-based Brillouin spectrometer. Additionally, we also introduced Faraday rotators for the purpose of ensuring strict backscattering while maintaining considerable signal

collection efficiency. In this study, we, for the first time, utilize a VIPA spectrometer in conjunction with a confocal pinhole setup, which allows the acquisition of *in-vivo* viscoelasticity-specific microscopic images. In this report, for the sake of simplicity, we only demonstrate spectroscopic applications to illustrate the proof of principle.

2.5.1 Experimental setup

The basic framework of the VIPA-based Brillouin spectrometer is given in Fig. 18. Its structure follows the description in Fig. 2.6 except two changes. Firstly, instead of a single mode fiber, we sent the Brillouin signal to the VIPA spectrometer through a pinhole. Secondly, we adopted a Faraday rotator (Electro-Optics Technology, Inc.) to manipulate the polarization of the incident and the back-scattered beams. Practically, we placed the Faraday rotator prior to the objective lens.

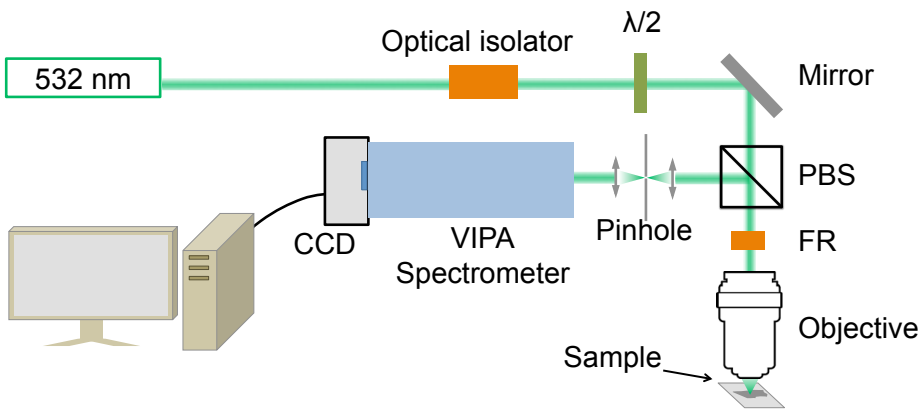

Figure 18 Schematics of the experimental setup. PBS: Polarizing beam splitter, FR: Faraday rotator, VIPA: Virtually imaged phased array.

In this section, in order to demonstrate the benefits induced by our optimizations, we tested difference entrance strategies of the VIPA spectrometer. An SM fiber (1-m long, Model: SM600, Fibercore Inc.) and a multi-mode fiber (1-m long, N.A.=0.22, Model:

FG050LGA, Thorlabs Inc.) were taken into consideration. The corresponding fiber launching system (Model: NanoMAX-TS, Max313, Thorlabs Inc.) was adopted as well.

2.5.2 Demonstrative results

2.5.2.1 An open-space pinhole setup enhance Brillouin signal strength while maintain strict confocality

Fig. 19 compares the typical outputs of the VIPA spectrometer using various entrance strategies, including single- and multi-mode fibers (Fig. 19 (a) and (b), respectively), open-space without and with a pinhole (Fig. 19 (c) and (d), respectively). When collecting data in Fig. 19 (a), we followed the fiber launching system described in Meng et al. [105]. A spherical lens (f = 8 mm, N.A. = 0.5) was applied in order to launch the backscattered beam into the fiber. The iodine cell was heated to 140 °C. The result shown in Fig. 19 (a) proves that the SM fiber setup is capable of collecting Brillouin signals as well as elastically scattered photons, though the overall signal level is low (< 30,000 photons per Brillouin line). Compared with Scacelli and Yun [5], our result is ~5 times weaker, which may due to the absorption of the iodine cell.

When collecting the data shown in Fig. 19 (b), we employed an N.A.=0.22 multi-mode fiber manufactured by Thorlabs (Model: FG050LGA). There was no observable Brillouin peak when using multi-mode fibers. Therefore, we chose to replace the sample with a reflective mirror, and reduced the CCD integration time (50 ms). Compared with SM fibers, the multi-mode fiber gave a loosely focused stripe. This is mainly caused by the imperfect input of the VIPA. When using multi-mode fibers, their large core size and high numerical aperture make its output difficult to be tightly re-focused. Therefore, the input may be sent to cover a broad area around the optimal entrance. Aspherical and

acylindrical lens may squeeze the focusing spot tighter by eliminating optical abbreviations. However, this strategy also increases the system cost and complexity. This loosely focused input also forbids signal to be efficiently coupled into the VIPA. For example, in order to ensure 90% signal to be coupled into the VIPA using a 50 μm wide stripe, the corresponding minimal tilting angle of the VIPA would be greater than 2.6° (calculations follow Shirasaki [135] and Xiao et al. [181]). As a result, when focusing the VIPA output at 1-m away, the separation between the peaks of different orders will be ~ 2 mm, or 125 pixels in the Newton 971 camera (pixel size: 16 μm × 16 μm). Considering the free spectral range (FSR) of the VIPA (33.3 GHz), each pixel will represent at least 260 MHz, which results in a very poor spectral resolution. The peak separation could be expanded with smaller tilting angle. However, the reflective coating will block a significant portion of the signal photons. Moreover, instead of the desired fundamental mode (LP01) given by SM fibers, the output of a multi-mode fiber is not simply a Gaussian distribution. In most cases, the output of multi-mode fibers will include a composition of many fundamental modes, many of which are hollow at the center. As a result, the image received by a CCD camera will be affected by the fiber output pattern and contaminate the acquired Brillouin spectrum.

Fig. 19 (c) presents the typical output of a VIPA spectrometer with an open-space entrance without any spatial filters. By removing the fiber setup, the corresponding insertion loss and the fiber's attenuation effect were avoided, and hence the CCD reading was drastically increased. However, when the equivalent pinhole is not presented, the inevitable scatterings / reflections induced by the optical components and the surface of the sample container / holder would be sent to the CCD detector, which induces unwanted contaminations. Moreover, when employing high N.A. objective lenses, Brillouin peaks broadening may happen due to the dependence of the frequency shift on the scattering angle [192]. Without an equivalent confocal pinhole (e.g., without an SM fiber), this broadening effect cannot be efficiently suppressed [186, 190]. In the

specific measurements shown in Fig. 19 (a) and (c), the Brillouin line was broadened by 5 pixels (i.e., ~ 400 MHz in Brillouin shift). The comparison is also given in Fig. 19 (e).

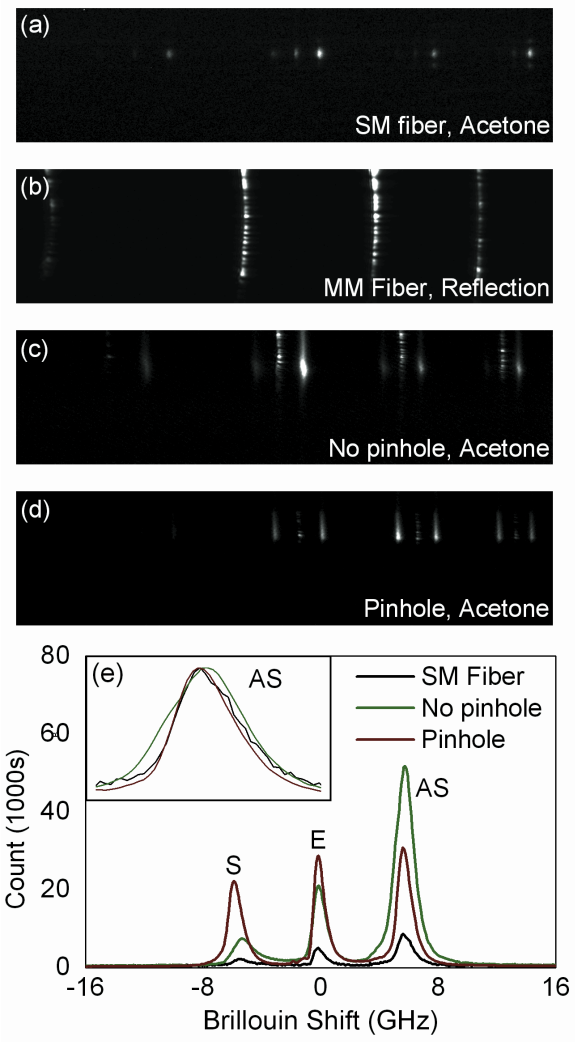

Figure 19 CCD images acquired with different setups utilizing (a) a SM fiber, (b) a multi-mode fiber, (c) open space without pinhole and (d) open space with a pinhole. (e) the retrieved Brillouin spectra for each setups. The "SM fiber" result has been stretched by 3 times. S: Stokes peak; AS: anti-Stokes Peak; E: Elastic peak. We used acetone as the sample in all tests except (b). Incident power: 35 mW. Integration time: 4 s.

Fig. 19 (d) depicts the CCD reading of a VIPA spectrometer with an open-space entrance plus a pinhole. Compared with Fig. 2.11 (c), the Brillouin peaks' linewidth

becomes narrower, though the signal strength was weakened as well. Nevertheless, the signal was still stronger than fiber-based setups.

Fig. 19 (e) compares the obtained Brillouin spectra by aforementioned different strategies. Note that the SM fiber's result has been stretched by 3 times for better visibility. Due to the laser wavelength drift, the Stokes peak has drifted as well, and may have passed through an absorption band of the iodine cell. Therefore, the Stokes peak in the pinhole experiment did not match its counterparts in the "no pinhole" and "SM fiber" measurements. Nevertheless, the anti-Stokes peak was not drastically affected by the iodine cell. The comparison shows that the anti-Stokes peak in the "pinhole" setup was ~ 10.70 times stronger than its counterpart in the "SM fiber" setup. The inset of Fig. 2.14 (e) depicts the linewidth difference between various setups. The peaks have been normalized. Unlike the "no pinhole" result, the Brillouin linewidth in the pinhole setup was similar with the "SM fiber" setup, indicating that the pinhole setup's confocality was maintained.

2.5.2.2 An optical Faraday rotator helps further enhance the collected signal and reduce the setup complexity

Due to the tiny wavelength shift in Brillouin scattering, there are no available dichroic mirrors that could separate the Brillouin-scattered photons from elastically scattered photons. In previous studies, investigators usually introduce a small offset in the incident angle, so that the Brillouin scattered photons will not follow the original incident path (e.g., [5, 102, 193, 194]). In this way, scattered photons could be spatially separated from the incident beam. However, the scattering angle of the collected photons would be slightly away from 180° with an uncertainty (resulted from manual tuning). The corresponding Brillouin shift, due to its dependency on the scattering geometry, will be affected. Another approach is to utilize a 45° non-polarizing beam-splitter (usually a

reflective neutral-density filter) to split the incident and the backscattered light (e.g., [105, 190]). This approach ensures a 180° scattering angle. However, even in the best case, only 50% of the signal could be induced to the detector. Considering the beam-splitter also blocks another 50% of the incident energy, 75% of the total system total potential was wasted.

On the other hand, in most of the biomedical sensing and imaging applications, only C_{11} in the stiffness tensor is taken into consideration. In this case, we only need to measure the backscattered Brillouin photons which keep the original polarization state of the incident beam [155]. In this experiment, we inserted a Faraday optical rotator prior to the objective lens. In this way, the polarization axis of the incident beam would be rotated by 45° when passing the rotator. The Brillouin scattered photons originated from the sample would pass the rotator again from the opposite direction. Consequently, the polarization status of the Brillouin photons would be rotated by an additional 45°, which makes the incident and the backscattered beams to be polarized in perpendicular directions. Therefore, the two beams can be simply separated by a polarizing-beam-splitter (PBS). In practice, we adopted a broadband PBS (Model: PBS051, Thorlabs) and a broadband Faraday rotator (Electro-Optics Technology, Inc.). A typical output is shown in Fig. 20 (a). The signal was collected without amplification setup (for example, electron multiplication). A Fully Vertical Binning (FVB) option was selected, so the readings on each column of the CCD array were added up. The strongest Brillouin peak reaches ~ 20,000 photons in amplitude. Considering the linewidth and multiple replicas of the Brillouin peaks, there were over 2,000,000 photons contributing to a specific Brillouin shift. Fig. 20 (b) shows a comparison among all the strategies mentioned in this study. The SM fiber's result was again stretched by 3 times for better visibility. Note that the "SM fiber" and the "pinhole" measurements in this figure were derived without Faraday rotators. Nevertheless, the results shown in Fig. 20 were collected with assistance of Faraday rotators. The anti-Stokes peak in "pinhole+FR" was 2.85 times stronger than the standalone "pinhole" setup, and was 30.21 times stronger than "SM

fiber" setup. Again, due to the iodine absorption and laser wavelength drifting, the Stokes peaks were not in a consistent position, and the absorption efficiency of the elastic peaks were distinct during separate measurements.

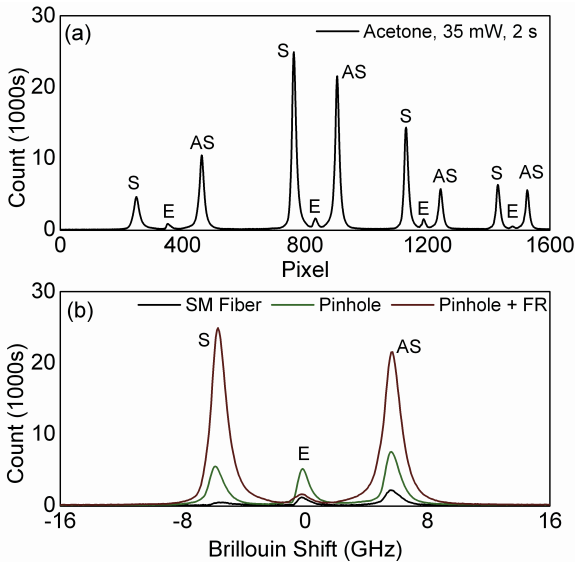

Figure 20 (a) Brillouin spectrum acquired with the optimized system. The exposure time was 2 seconds, and the incident power was 35 mW. (b) Comparison between different VIPA spectrometer entrances. The "SM fiber" result has been stretched by 3 times. The sample was acetone. S: Stokes peak; AS: anti-Stokes peak; E: elastic peak; FR: Faraday rotator.

2.5.3 Discussion and conclusion

In this section, we have demonstrated a simple and efficient Brillouin microspectroscopy setup, which allows for an accurate and fast assessment of Brillouin spectra of weak scattering samples. For the purpose of enhancing the signal collecting efficiency, we replaced the fiber-based entrance by an open-space setup with a pinhole. To ensure the scattering angle to be 180° while maintaining 100% signal collection efficiency, we inserted a Faraday optical rotator prior to the focusing objective lens. The optimizations of the setup are simple but efficient. We anticipate the wide use of this experimental arrangement in future applications of Brillouin microspectroscopy.

2.6 Dual Brillouin/Raman Microscope for Mechanical and Chemical Characterization and Imaging

In this section, we present the optical arrangement for establishing the dual Brillouin/Raman microspectroscopy. Raman spectroscopy/microscopy, since its inception, has become a staple technique with a diverse range of applications in an equally diverse number of fields spanning industrial product inspection, scientific research, and medical diagnostic sensing [32, 33, 114-117, 195-201]. Even now, novel adaptations of Raman spectroscopic imaging have been realized for tomography and noninvasive deep tissue diagnosis [202, 203]. Unlike Raman spectroscopy, which offers information about the chemical makeup of the sample, Brillouin spectroscopy provides information about the viscoelastic properties of a material. Each of these imaging/sensing tools offers useful diagnostic information, therefore a single apparatus that could provide simultaneous measurement of both spectra from the same point would be extremely powerful for sample characterization and analysis.

So far, complementary use of Raman and Brillouin microscopy has only been reported once, and the spectra were acquired using separate instruments [204]. Long acquisition times (~10 min) for each Brillouin spectra are clearly impractical, and a lack of same-point detection for both spectra makes the analysis complicated. To overcome these issues, we use a single pump laser to generate both Raman and Brillouin spectra and provide simultaneous imaging/sensing from the selected confocal volume. More importantly, we take advantage of recent advancements in Brillouin spectroscopy to decrease the acquisition time, as any practical implementation of simultaneous detection requires that the times for both to be comparable.

2.6.1 Experimental setup

Our experimental setup, sketched in Fig. 21, follows the typical optical arrangement of a back-scattering confocal microscopy. Similar with the setups described in previous sections, the setup is based on a 532-nm single mode solid-state laser, with an output power of ~100 mW (Lasermate Group Inc.; model: GMSL-532-100FHA). The nominal output linewidth for this pump source is ~ 640 kHz. Similar with the setup discussed in section 2.4, we used an optical isolator (Electro-Optics Technology, Inc.; BB-8-05-I-090) to prevent feedback from the optical set-up. A polarizing beam splitter was placed in the beam path to direct the backscattered light towards the Brillouin or Raman spectrometer. A microscope objective focused the pump laser onto the sample and collected the back-scattered light. A Faraday optical rotator (Electro-Optics Technology, Inc.) was placed prior to the objective lens to rotate the polarization of the back-scattered beam by 90°.

When the backscattered light is collected by the objective lens, it is split spectrally by a 45° long-pass filter (cut-on wavelength: 537.5 nm), decoupling the Raman signal and passing it into a fiber coupled spectrometer (Shamrock 303i with attached iDus 401 CCD, Andor Inc.) while the elastic and Brillouin components of the spectra are reflected, focused into a 25 μm confocal pinhole, and are then sent into a 15 cm long iodine cell acting as a notch filter. With the elastic scattering suppressed by the iodine cell, the light is passed into a VIPA with a free spectral range (FSR) of 33.3 GHz, which images the Brillouin spectrum onto a CCD (Newton 971, Andor Technology, Inc.). The iodine cell plays the role as described in previous sections. The use of the iodine cell as a notch filter is necessary, as the elastically scattered light from a sample is usually intense enough to obscure the Brillouin signal. In Raman spectroscopy, conventional long-pass and dielectric notch filters are sufficient as the Raman frequency shifts are extremely large in comparison.

Prior to each spectroscopic acquisition, we utilized an optical microscope setup to determine the position of the focusing spot (Fig. 21a, inset). In this case, the sample was illuminated by an LED source (Mightex Inc., FCS-0540-000, wavelength: ~530 – 590 nm). The 532 nm laser was still focused onto the sample. An appropriate neutral density filter was inserted in the beam path of the laser so the camera would not be saturated. The image was collected by a CMOS camera (Mightex Inc., BCE-C050-U, shown in the inset of Fig. 21a).

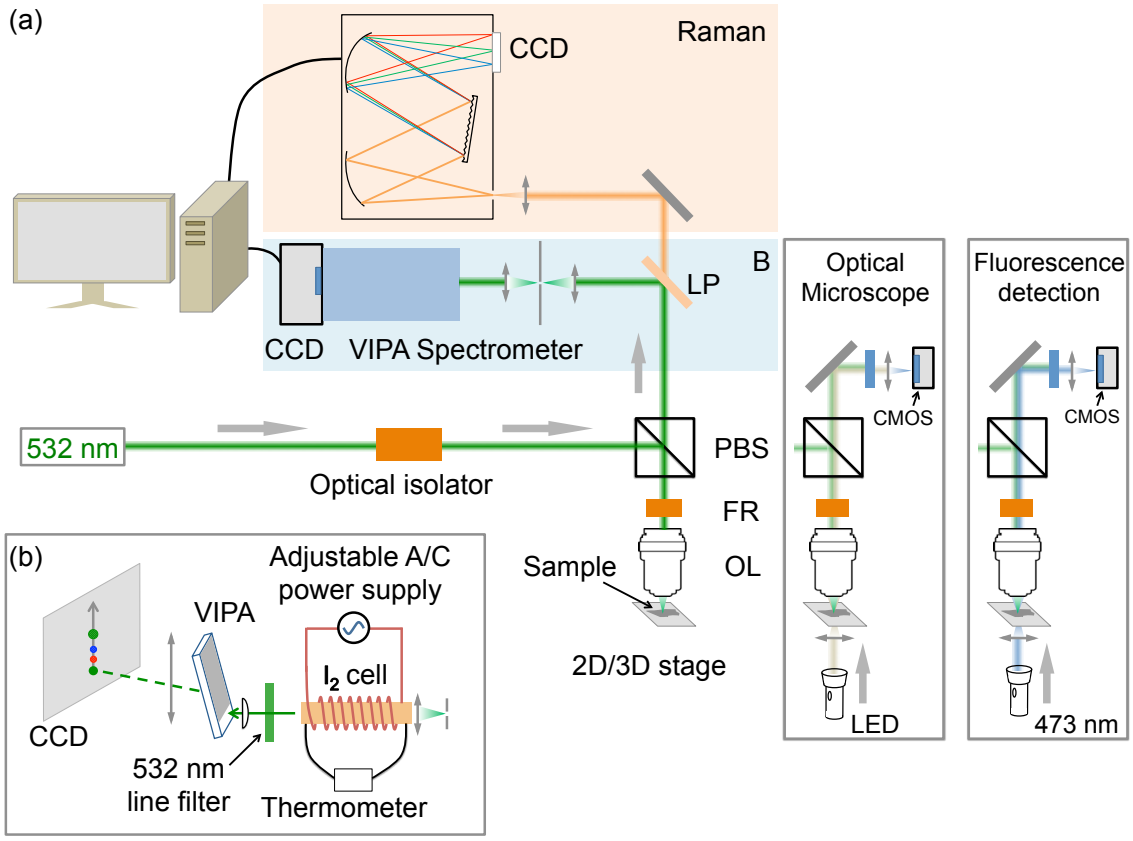

Figure 21 (a) A schematic diagram of the optical setup for Brillouin and Raman spectroscopy and microscopy. VIPA: virtually imaged phased array; LP: long-pass filter; FR: Faraday rotator; PBS: polarizing beam splitter; OL: microscope objective lens; R: Raman acquisition branch; B: Brillouin acquisition branch; Insets: optional branch for possible wide field optical microscope imaging (left) or fluorescence imaging (right); (b) The VIPA spectrometer in greater detail.

The sample is placed upon a piezo or motorized scanning microscopy stage (Thorlabs Inc, Model: MLS203-1, or Micos Inc., model SMC MT-40 2D). The stage, as well as the Raman spectrometer and Brillouin camera, are all controlled by LabVIEW software allowing for simultaneous acquisition of Raman and Brillouin spectra as the sample is translated.

To validate the imaging capability of the microscope, an intramuscular adipose tissue taken from chicken legs was imaged. Specifically, we restricted our scanning area at an interface between the adipose (fat) tissue and the muscle tissue. After preparation, the sample was placed on the translation stage and raster scanned to create two-dimensional Raman and Brillouin images. Scanning was performed in 5 μm increments using a 20x/0.40 NA Nikon objective lens, creating an image of 35 × 40 pixels with dimensions of 175 μm × 200 μm. The scan was performed using exposures of 0.5 s for each Raman and Brillouin spectrum, respectively. These exposure times were chosen to provide adequate contrast without incurring a large time cost. The total scan time, limited by the Raman spectral acquisition, was about 15 minutes. The spot size of the beam was calculated to be ~2 μm; however, submicrometer spatial resolution is possible by simply using a higher numerical aperture objective lens.

2.6.2 Demonstrative results using phantom samples

Acquisition and analysis of Raman spectra has been extensively discussed in the literature, borrowing from decades of innovation. However, VIPA-based Brillouin spectroscopy has not yet enjoyed as widespread of an adoption, and therefore, there is a lack of spectrometers developed for this purpose. In this study, we follow the data processing method as discussed in Section 2.3.

Representative Raman and Brillouin spectra for both adipose and muscular tissues are depicted in Fig. 22. Differences between fat and muscular tissues can be distinguished

either from their Raman or Brillouin spectra. Specifically, the fat tissue possess stronger ~2845 cm^{-1} Raman peak, which represents for the asymmetric vibrational modes for the alkane CH_2 bonds.

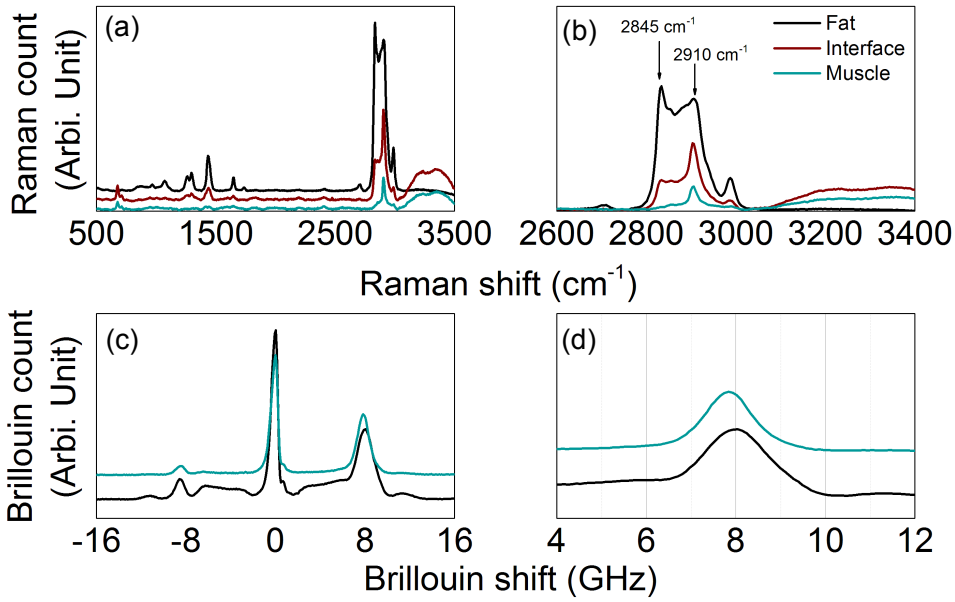

Figure 22 Typical Raman (a-b) and Brillouin (c-d) spectra for several representing positions.

The 2D image of the muscular-fat interface is illustrated in Fig. 23. The image size is 175 μm × 200 μm. For each pixel, we acquired the entire Raman and the Brillouin spectra. The information of the Brillouin spectra, including Brillouin shift and Brillouin linewidth, are given in Fig. 23 (a) and (b), respectively. Nevertheless, for the Raman information, we only plot the amplitude ratio between the Raman peaks at 2845 cm^{-1} and 2910 cm^{-1}. In the next discussions, we will call it as "Raman ratio". For muscular tissues, the Raman peak is mainly composited by the 2910 cm^{-1} component. Therefore, their Raman ratio is relatively lower. For the fat tissues, the Raman ratio is substantially higher than the muscles. Therefore, according to the Raman image, we can clearly identify the regions representing fat and muscular tissues.

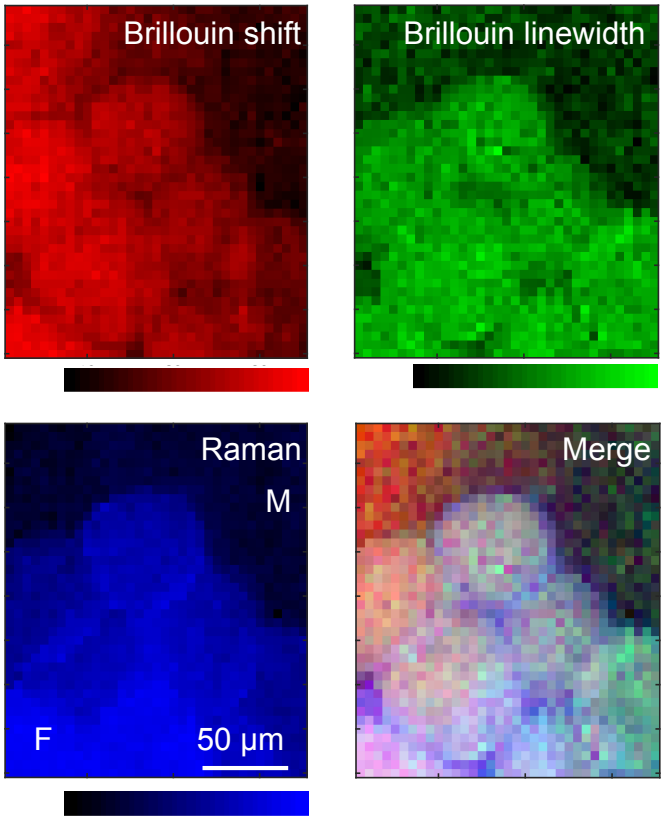

Figure 23 The two-dimensional Raman/Brillouin images for the interface between fat and muscular tissues. The Raman image represents the peak ratio between 2845 cm^{-1} and 2910 cm^{-1} for each pixel. F: Fat tissue; M: Muscular tissue.

We further correlate the Raman results with the Brillouin shift. The correlation result is shown in Fig. 24. Each data point in Fig. 24 represents a pixel shown in Fig. 23. According to the Raman results, the data points are mainly separated into two groups, representing muscular (lower Raman ratio) and adipose tissues (higher Raman ratio), respectively. A weak linear correspondence can be observed between the Brillouin shift and the Raman ratio. However, this correlation cannot be described by a simple function. In this sense, Raman and Brillouin spectroscopy may reveal different source of contrasts.

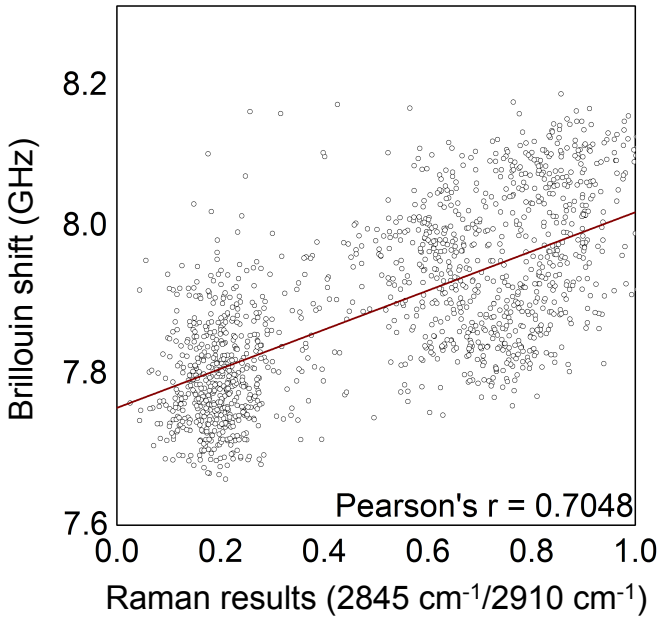

Figure 24 The correlation between the Brillouin shift and the amplitude ratio between the 2845 cm^{-1} and 2910 cm^{-1} Raman peaks. A weak linear correlation could be observed between the Raman ratio and the Brillouin shift. The data is extracted from the 2D image shown in Fig. 23.

2.6.3 Discussions and summary

In this section, we have demonstrated the effectiveness and potential for a dual Raman-Brillouin microscopy system in producing highly accurate measurements and providing complementary chemical and mechanical information. Simultaneous acquisition of Brillouin and Raman spectra from the same focal region allows for an expanded level of sample characterization without sacrificing quality of signal from either modality. Moreover, there is no added time cost for simultaneous acquisition of both spectra, as exposure times for Raman and Brillouin are comparable. For these reasons, this system should find widespread adoption as a very powerful tool throughout science and engineering.

While the images and spectra above illustrate the capabilities of this instrument, better sensitivity and spectral resolution can be achieved through various improvements to the system. For example, replacing the pumping laser with a 780 nm source would allow more laser power to be exerted on the sample. Correspondingly, the signal quality and the signal-to-noise ratio could be enhanced.

The real significance of this dual microscopy system will be realized when it is applied to characterization of biological systems or novel materials. Its ability to simultaneously monitor changes in a system's mechanical and chemical properties makes it an unprecedented diagnostic tool. In this capacity, it is uniquely situated to become a valuable aid for researchers.

CHAPTER III

TISSUE LEVEL APPLICATION: BRILLOUIN SPECTROSCOPY REVEALS CHANGES IN MUSCULAR VISCOELASTICITY IN DROSOPHILA POMT MUTANTS

3.1 Introduction

Muscular dystrophy (MD) is a group of muscle diseases that are frequently associated with defects in the Dystrophin-Glycoprotein Complex (DGC), a multimeric transmembrane protein complex that facilitates communication between the intracellular and extracellular space. It affects ~ 200,000 patients within the U.S. annually. MD symptoms include physiological and developmental defects such as weakness of skeletal muscles and muscle degeneration. One of the critical sign of MD is the abnormal mechanotransduction functionality of the muscle cells, and the consequent active/passive mechanical property change in muscular tissues [205-207]. However, the observations of the correlation between the MD stage and the muscle stiffness remain controversial. It is necessary to measure these properties in vivo and in situ to study how the stiffness of the muscle tissues/cells is regulated in the course of the pathogenesis of MD. To date, separate techniques, including atomic force microscopy (AFM) [96] and optical tweezers [208], have been developed to probe the microscale mechanical properties of living organisms. Nevertheless, these approaches rely on invasive mechanical contact and/or used in a close vicinity of the sample, and, therefore, cannot be used in situ, such as sterile microenvironment. Moreover, various complications, such as the tip-sample interactions, the limited field of view (FOV) and imaging speed, prohibit potential clinical application of AFM [209]. Some non-invasive techniques, including ultrasound elastography[210] and magnetic resonance elastography[79], have been well established during the past decades. However, despite their capabilities of providing the

macroscopic/bulk materials stiffness, these techniques are fundamentally limited by their spatial resolution, and are unable to perform microscopic measurements.

In this chapter, we introduce Brillouin spectroscopy as a non-contact and label-free probing technique for measuring the mechanical properties of muscle tissues. Brillouin scattering originates from the inelastic interaction between the incident electromagnetic wave and the thermal phonons in the material of interest. By measuring the Brillouin shift of the scattered light, investigators are enabled to determine the physical property of the high-frequency acoustic wave, and, therefore, derive the local longitudinal modulus of the sample. In this study, we, for the first time, extended Brillouin spectroscopy to probing the microscopic viscoelasticity of muscle tissues, and demonstrated its capability of screening dystrophy among similar individuals.

3.2 Materials and Methods

The experimental setup is follows Fig. 21. Here we used a 532-nm single-longitudinal mode laser was employed as the pumping source. We also utilized a low numerical aperture objective lens (Olympus, RMS4X, N.A. = 0.1) to achieve a loose focusing spot. In this way, we could avoid the possible subcellular heterogeneity within the muscle tissues. The larger focusing volume also ensures us to get an averaged Brillouin shift.

During the experiment, we labeled some of our samples with green fluorescence protein (GFP). Therefore, the sample's morphology can be monitored by fluorescence emissions. To do so, we incorporated a fluorescence microscope into the dual Brillouin/Raman spectroscope (Fig. 21a, inset). When taking fluorescence images, the sample was illuminated by a 473 nm laser. The 532 nm laser was still focused onto the

sample, although it has been substantially attenuated. The fluorescence image was collected by a CMOS camera.

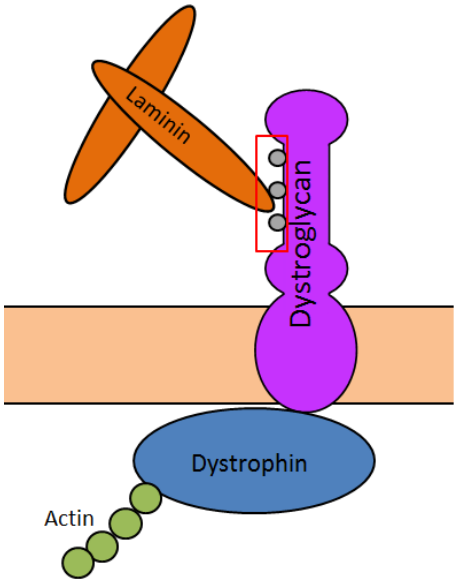

Figure 25 Schematic illustration of Dystrophin Glycoprotein Complex (DGC). Defects in this complex are related to various forms of muscular dystrophy. O-mannosyl glycans (boxed in red) are added to dystroglycan by POMT, and are crucial for interactions with laminin in mammals.

In this study, we employed a Drosophila model of dystroglycanopathies, human congenital muscular dystrophies resulting from abnormal glycosylation of alpha-dystroglycan (Dg) (see Fig. 25). With the assistance of Brillouin spectroscopy, we measured the microscopic muscle elasticity in Drosophila larvae with homozygous defects in either of the Protein O-Mannosyl Transferase (POMT) genes, rotated abdomen (rt) or twisted (tw). These genes are homologues of human POMT1 and POMT2, respectively, and are so named because of the characteristic clockwise rotation of the Drosophila abdomen that arises in these mutants. Although POMT mutations in Drosophila can easily be distinguished by morphology, differences in dystrophic

genotypes are not always so readily apparent in other species, including humans. Functionality of both POMT genes is required to catalyze the addition of the sugar D-mannose to serine and threonine residues of target proteins, a process known as O-mannosylation. Mutations in either tw or rt can cause failure of POMT to O-mannosylate its target proteins, including dystroglycan. Failure to O-mannosylate Dg inhibits interactions between the DGC and the extracellular matrix, and in humans this can lead to the most severe of the congenital muscular dystrophies, Walker-Warburg Syndrome. Different POMT mutations can lead to different phenotypic severities, despite the fact that all tested mutations seem to inhibit O-mannosylation at the same level.

We also measured Brillouin shift in muscle tissue from biopsies of two Golden Retrievers, one normal and one with Duchenne Muscular dystrophy (DMD). Whereas POMT mutations disrupt the extracellular component of the DGC, DMD disrupts the intracellular component by removing dystrophin. In the canine model we were again able to detect decreased elasticity in all dystrophic muscles measured. Taken together our results demonstrate 1) that Brillouin shift can detect elasticity differences in biological systems, 2) that dystrophic muscle tends to be stiffer than its non-dystrophic counterparts in both insect and mammalian models, 3) that Brillouin spectroscopy can distinguish very similar genotypes, and 4) that muscle stiffness arises from disruptions of both intracellular and extracellular components of the DGC.

3.3 Results

We first recorded the morphology of the abdomen tissues of the Drosophila models (see Fig. 26a). Both POMT1 (rt) and POMT2 (tw) are required for O-mannosylation, and inactivation of either abolishes O-mannosylation of Dg. However, different mutations result in varying degrees of severity. Severity of POMT mutations can be easily quantified in adult Drosophila. Mutations in either tw or rt result in a clockwise rotation of the abdominal axis of symmetry, and more severe mutations manifest as larger

rotational angles. We scored the abdominal angles of 20 adult males for wildtype (WT), tw, and rt genotypes and found that on average our tw allele yields ~13° of rotation, whereas our rt alleles result in ~40°. Statistical results are given in Fig. 26(b).

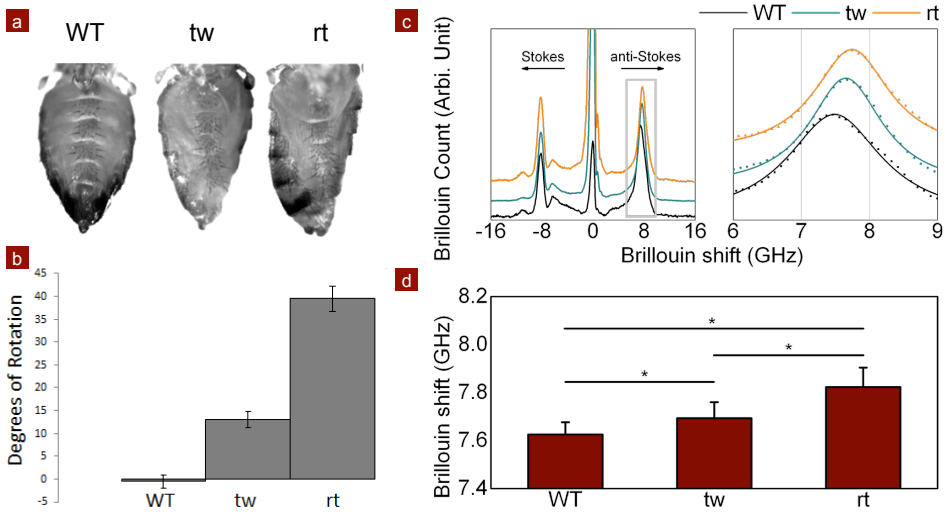

Figure 26 (a) Representative abdomens of WT, tw (POMT2) and rt (POMT1) Drosophila showing rotation. (b) Average rotational angle of WT, tw, and rt abdomens in adult flies. n>20 in all cases. (c) left: Representative Brillouin spectra from WT, tw, and rt larvae. right: boxed region from the left panel representing anti-Stokes shift. The dots represents the actual reading at each camera pixel, and the fitting lines are plotted as well. (d) Statistical comparisons of the Brillouin shift acquired from different genotypes. (*: p<0.000001)

Next, we measured the Brillouin spectra as well as the Raman spectra of the samples. We prepared WT, tw, and rt Drosophila larvae, each expressing a GFP-labled myosin heavy chain which would be abundant in muscle tissue specifically (Fig. 27a). We raised larvae to the late third instar stage, fileted them, and removed fat bodies and entrails. In order to ensure the correct probing position and minimize the interference from other tissues, we took the fluorescence image prior to the Raman/Brillouin measurements. We were thus able to visualize the focal plane of the laser in the context of the muscle being measured. Example fluorescence image is shown in Fig. 27(b). Examples of the raw

Brillouin spectra are shown in Fig. 26(c). The Brillouin peak can be detected within 1 s exposure time. Distinct Brillouin shifts could be observed for different genotypes. In these particular examples, WT muscle tissues showed the least elasticity. The Brillouin shift in rt model was ~ 0.4 GHz higher than the WT model. This indicates ~ 76 m/s difference in sound speed (assume the refractive index of muscle tissue is 1.4), or 230 MPa difference in Brillouin elastic modulus (assume mass density is 1.04 g / mL). The Brillouin shift of tw models was found in between WT and rt models (Fig. 26c). We further extend the experiment to more individuals, and randomly selected the acquisition points on each individual. The statistical analysis suggests that the Brillouin shift for the three genotypes were mutually and significantly different (p<0.000001).

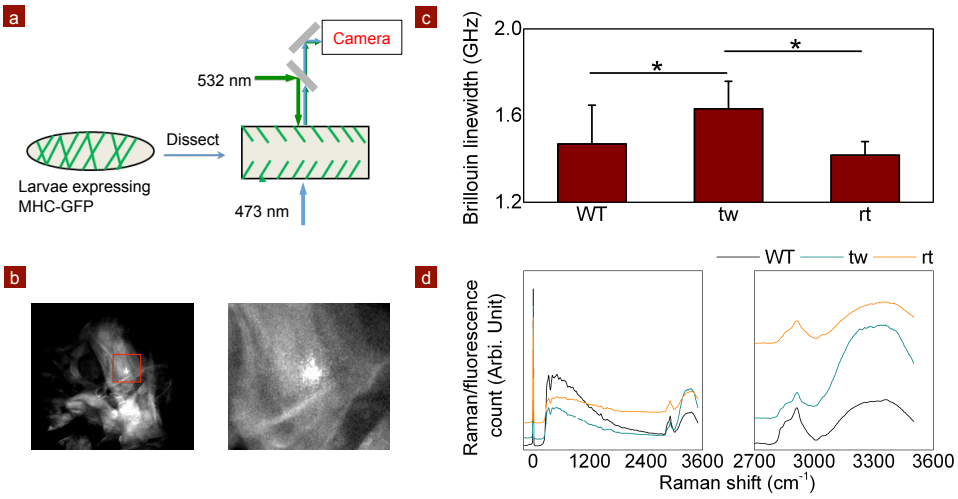

Figure 27 (a) The imaging geometry when taking the fluorescence images. (b) Example fluorescence image of the sample. Here the white spot (inside of the red box) is induced by the 532 nm laser for Brillouin spectroscopy. Nevertheless, its intensity was substantially attenuated. The right panel presents the magnified image within the red box. (c) Statistical results for the Brillouin linewidth. Compared with the other two genotypes, tw samples are slightly more viscous. (*: p<0.05) (d) Typical Raman spectra from GFP-labeled larvae. Since the GFP labels were still partially excited by the 532 nm laser, the Raman spectra at ~ 600 – 1800 cm^{-1} was diminished. Nevertheless, the Raman peak at ~ 2950 cm^{-1} remained clear (see the right panel).

We also examined the Brillouin linewidths of the samples, as it is an indicator of the sample's viscosity [1]. Nevertheless, unlike the Brillouin shift, the linewidths of different genotypes are less correlated to the dystrophy severity (Fig. 27c). Fig. 27(d) shows the typical Raman spectra for each genotype, which are recorded by the Raman detection branch of the setup. Due to the presence of GFP, the visibility of the Raman peaks within the range 600 cm^{-1} – 2500 cm^{-1} was diminished. Nevertheless, the Raman peaks around 3000 cm^{-1} are still visible. We note that the Raman peak at ~ 2910 cm^{-1} was stronger than the peak at ~ 2850 cm^{-1}, indicating the sample was rich in protein instead of lipid. The presence of water also contributed in strong peaks at ~ 3100 – 3400 cm^{-1}. In order to acquire the Raman spectra within 600 – 1800 cm^{-1} range, we did separate experiments without GFP labeling. Examples of Raman spectra will be given in the following text.

Our results so far have shown the ability of Brillouin spectroscopy to distinguish between genotypes in dissected, GFP-labeled larvae. We next sought to use it as a technique to measure elasticity non-invasively and in the absence of molecular labels. This time, we extended the number of genotypes for our measurement. Seven genotypes were taken into consideration, including wildtype (WT), twisted (tw), abnormal glycosylation of alpha-dystroglycan (dg), twdg: twisted + abnormal glycosylation of alpha-dystroglycan, Res: rescue, NegCtr: negative control; oe: over expression (need some explanation about the genotypes). The experiments were performed under semi-intact conditions. Larval heads were removed so they wouldn't move during measurements, but fat bodies and entrails were left in place. The laser has a penetration of ~ 50 μm, and was focused just under the surface of the semi-intact larva, where body wall muscle is. For each genotype, we selected more than 6 individuals, and took more than 5 separate acquisitions on each individual. The Brillouin shift and statistical studies are presented in Fig. 28. Except two pairs (WT v.s. twdg, and NegCtr v.s. DG), all other genotypes are mutually and significantly different. We note that when measuring the "oe" samples, some positions gives ultra-high Brillouin shift (~ 1 GHz greater than the

WT samples). In these experiments, we were not able to visualize the muscles being measured. Nevertheless, we were able to obtain similar Brillouin spectra and conclusion (especially, for the genotypes "WT" and "tw") compared with the previous studies shown in Fig. 26. This demonstrates that Brillouin spectroscopy can distinguish different genotypes in a non-invasive manner, and without the need for tissue labeling.

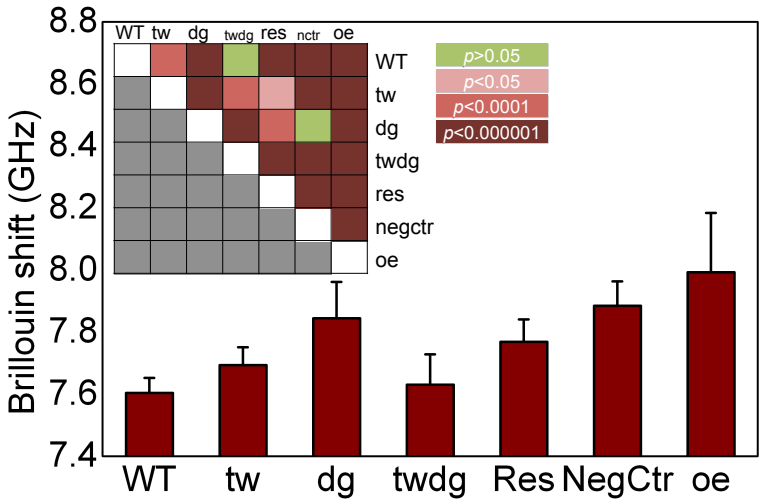

Figure 28 Statistical results for the Brillouin shift acquired from 7 different genotypes. Mean value comparisons are given in the inset. WT: wildtype, tw: twisted, dg: abnormal glycosylation of alpha-dystroglycan, twdg: twisted + abnormal glycosylation of alpha-dystroglycan, Res: rescue, NegCtr: negative control; oe: over expression.

We have again measured the Brillouin linewidth and Raman spectra. Some genotypes had indistinguishable Brillouin linewidth. Meanwhile, for most of the genotypes, their linewidths were significantly different (Fig. 29). Unlike the GFP-labeled muscle tissues, this time, we are enabled to see the Raman spectra within the signature range (i.e., 600 – 1800 cm^{-1}) (see Fig. 29). However, the Raman spectra shape for all seven genotypes were visually similar. A careful calculation reveals that the normalized cross-correlation is greater than 0.99 between any two genotypes, indicating that Raman spectroscopy is insensitive to the genotypes of the Drosophila models.

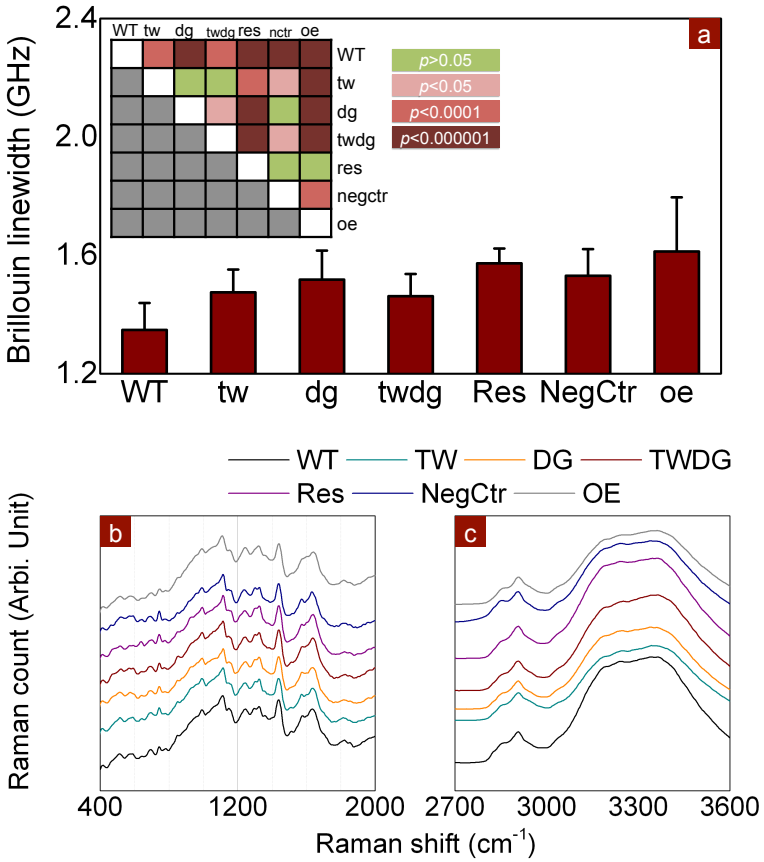

Figure 29 (a) Statistical results for the Brillouin linewidth acquired from the samples shown in Fig. 28. Mean value comparisons are given as well. (b and c) Raman spectra for all the genotypes, including the Raman signature range (600 – 1800 cm^{-1}), and the ~2900 cm^{-1} range. The presence of water resulted in peaks at ~ 3100 – 3400 cm^{-1}. In the Raman signature range, the normalized cross-correlations between any two spectra are greater than 0.99, suggesting that Raman spectra are insufficient to distinguish different genotypes. WT: wildtype, tw: twisted, dg: abnormal glycosylation of alpha-dystroglycan, twdg: twisted + abnormal glycosylation of alpha-dystroglycan, Res: rescue, NegCtr: negative control; oe: over expression.

To further demonstrate the applicability of Brillouin spectroscopy, we measured muscle stiffness in a mammalian model (Golden Retrievers) of Duchenne Muscular Dystrophy (DMD). In this animal model, the affected protein is dystrophin, which acts on the intracellular side of the DGC complex. It is different from the aforementioned Drosophila models, whose glycosylated portion of dystroglycan (i.e., the extracellular portion of the DGC complex) was modified (see Fig. 25). We measured the Brillouin

spectra of several muscles biopsied from the hindlegs of a dystrophic and a healthy Golden Retriever. Specifically, the muscles measured were Cranial Sartorius (CS), Lateral Head of Gastrocnemius (LHG), Long Digital Extensor (LDE) and Vastus Lateralis (VL). For each muscle tissue, we of randomly selected multiple points for Brillouin acquisition ($n \geq 5$). Nevertheless, due to the turbidity of the sample, Mie scattering contributes in a great portion of the scattered photons, and substantially elevated the elastic peak (see Fig. 30). Meanwhile, due to the strong light absorption induced by myoglobin, we lowered our light intensity to avoid any photothermal damages (incident power < 5 mW). However, the signal strength and quality were decreased accordingly.

The experimental results and mean comparisons are plotted in Fig. 31. Interestingly, the overall Brillouin shift for the canine muscle tissues was lower than the Drosophila models. This may be induced by distinct refractive indices, mass density, or longitudinal modulus of the muscle tissues of the two species, and may be reviewed in further studies. Nevertheless, similar to the previous results, dystrophic muscles showed a greater Brillouin shift than their wildtype counterparts in all cases. Besides the LHG samples, the muscle tissues taken from the healthy and the dystrophy canine models are significantly different ($p<0.05$). In this sense, Brillouin spectroscopy can detect stiffening of mammalian muscles as well as insects. Moreover, these results demonstrate that muscle stiffening can be observed when a separate part of the DGC is affected.

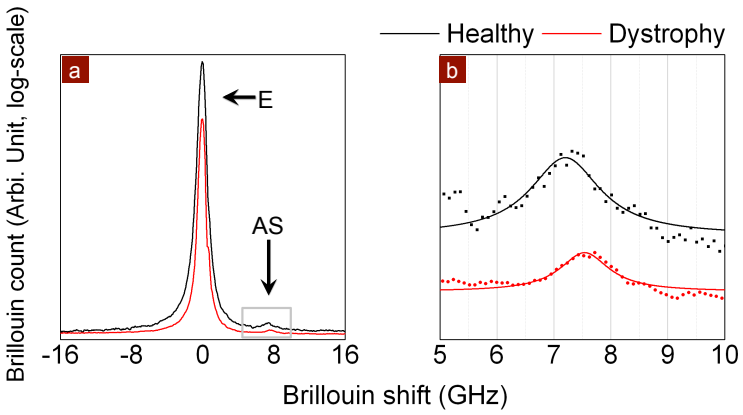

Figure 30 (a) Raw Brillouin spectra taken from Vastus Lateralis (VL) muscle biopsies of a healthy and a dystrophic dog. Due to the turbidity of the sample, the Mie scattering contributed substantial amount of elastically scattered photons. The elastic peak (at the center) was much stronger than the Brillouin peaks (at left and right). (b) Boxed region from (a) representing anti-Stokes shift. The dots represent the actual reading at each camera pixel, and the fitting lines are plotted as well. E: Elastic peak, AS: anti-Stokes peak of the Brillouin signal.

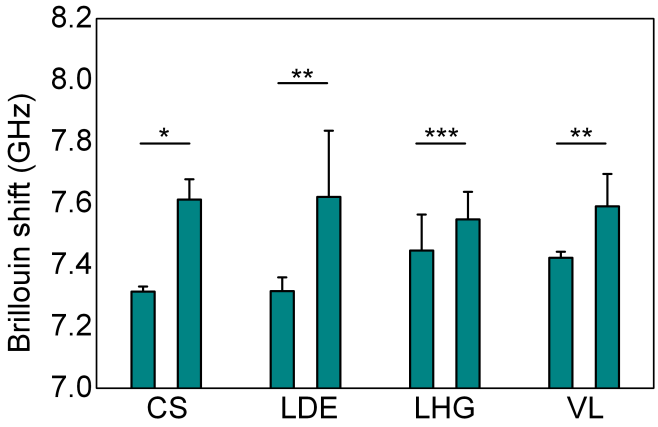

Figure 31 Brillouin spectra taken from muscle biopsies of a healthy (left) and a dystrophic (right) dog. The biopsies were taken from different positions of the dogs. Random probing points were selected ($n \geq 5$). CS: Cranial Sartorius; LDE: Long Digital Extensor; LHG: Lateral Head of Gastrocnemius; VL: Vastus Lateralis. (*: $p<0.0001$, **: $p<0.05$, ***: $p>0.05$)

3.4 Discussions and Summary

In this chapter, we have demonstrated that Brillouin spectroscopy can work as a non-invasive tool for screening muscular dystrophy. Our current results indicate that the muscle tissues taken from dystrophy individuals possess greater Brillouin shift than the tissues taken from healthy individuals. If we assume the refractive index and the mass density of the muscle tissues are identical among different individuals, we can conclude that the dystrophic muscle tissue is stiffer than healthy ones. This conclusion is valid for both insect models and mammalian models. Besides a few exceptions, the difference in Brillouin shift was statistically distinct between the healthy and dystrophy animal models.

Moreover, we have demonstrated that Brillouin spectroscopy can distinguish different types of muscular dystrophy, even in cases where the underlying mechanism is nearly identical (e.g., the "tw" and the "rt" Drosophila models). Meanwhile, we have demonstrated that, under our current experimental condition, Raman spectroscopy is unable to distinguish the healthy and dystrophy individuals, and is also unable to tell the difference between different dystrophy types. The experimental results suggest that Brillouin spectroscopy could be developed into a unique and useful diagnostic technique for pre-clinical and clinical applications. Due to the optical nature of Brillouin spectroscopy, all examination can be accomplished in a non-contact and non-invasive manner. It would be advantageous as it could remove the need for muscle biopsies. However, at the current stage there are some limitations that would need to be addressed prior to development for clinical settings.

First, while we have demonstrated the non-invasive function of this technique in Drosophila models, our mammalian system still required a biopsy. The optical setup needs to be scaled to the size of larger animals in order to accommodate them.

Additionally, while the laser was able to penetrate the relatively transparent larval cuticle, it remains unknown to what degree skin and hair might interfere with measurements in intact mammals. In order to enhance the penetration depth and avoid possible thermal damage, we may take advantage of the so-called "biological window" [211] by selecting an NIR pumping source (e.g., 780 nm, [112, 212]).

Second, in the context of mammalian tissue our system yielded a Brillouin signal that, while detectable, was very weak. We believe this may be due to the myoglobin in the muscle, which absorbs strongly at 532 nm. This is especially true for mammalian models. Due to the ultra strong absorption, the incident laser power was substantially lowered, resulting in weak signal strength. Again, we believe a longer wavelength laser may solve this problem, as myoglobin absorbance quickly drops off beyond about 580 nm.

In summary, we have demonstrated that Brillouin spectroscopy is a novel approach to probing the viscoelasticity of the muscle tissues. Moreover, we have demonstrated the distinct muscular elasticity under different dystrophy status. To the contrary, the viscosity measurements were less conclusive. This demonstration warranted further pre-clinical or clinical applications on MD screening and diagnosis.

CHAPTER IV

WHOLE-BODY LEVEL APPLICATION: WATCHING EMBRYONIC DEVELOPMENT IN A NEW LIGHT: ELASTICITY SPECIFIC IMAGING WITH DUAL BRILLOUIN/RAMAN MICROSPECTROSCOPY

4.1 Introduction

Morphogenesis, the biological process of developing shape, is fundamentally a biomechanical process. Cells bring about changes in embryonic form by generating patterned forces and by differentiating the tissue mechanical properties that harness these forces in specific ways [213]. In this sense, cells and tissues differentiation are greatly impacted by microscopic variations of the microenvironments' viscoelastic properties.

In this chapter, we take zebrafish embryos, a model for epithelial and mesenchymal morphogenesis, as an example to demonstrate the appliability of Brillouin spectroscopy in the field of developmental biology. At the beginning of its gastrulation, the zebrafish embryo consists of a mesenchymal cell population that will constitute the embryo proper (the deep cell layer), an epithelial covering constituting the first embryonic skin (the enveloping layer, or EVL) and the extraembryonic yolk syncytial layer (YSL). Gastrulation proceeds via epiboly, or the spreading of the embryo to envelope the yolk. Epiboly requires cytoskeletal elements in the YSL, which generate force that is transmitted through the EVL. A contractile actomyosin ring in the YSL drives flow-friction and circumferential constriction mechanisms to drive EVL epiboly [214], but the relationship of these processes to DCL gastrulation is not understood. Importantly, the relationship of cytoskeletal-generated force and the viscoelastic properties of these different cell populations is not known and is difficult to study outside the embryo. We

expect Brillouin microscopy will enable previously unattainable views of the biomechanical properties of all cell populations of a gastrulating embryo.

In this study, by taking advantage of Brillouin spectroscopy, we demonstrated the applicability of Brillouin spectroscopy in the field of developmental biology. Specifically, we probed the viscoelasticity properties of different compartments of living zebrafish embryos, including yolk-sac, skin, spine and heart. We have also made a two-dimensional image of the embryos. Moreover, with the assistance of dual Raman/Brillouin setup, we collected Raman spectra simultaneously while acquiring the Brillouin spectra.

4.2 Materials and Methods

In this study, we follow the optical setup set forth in Chapter 2 (Fig. 21). We also coupled the setup with the bright field optical microscope in order to collect the optical image of the sample (see Fig. 21a, inset). Prior to each spectroscopic acquisition, we utilized the optical microscope setup to determine the position of the focusing spot. In this case, the sample was illuminated by an LED source (Mightex Inc., FCS-0540-000, wavelength: ~530 – 590 nm). The 532 nm laser was still focused onto the sample. An appropriate neutral density filter was inserted in the beam path of the laser so the camera would not be saturated. The image was collected by a CMOS camera (Mightex Inc., BCE-C050-U).

In this experiment, we utilized wildtype zebrafish embryos. The embryo was mounted in 1.2% low-melt agarose in 1X fishwater on a glass slide in order to prohibit its movements. The Tricaine solution was also added on top of the agarose after it firmed around the embryo, ensuring the embryo remained anesthetized. After the needed data

was collected from an embryo, it was euthanized in an ice water bath and stored in the freezer to await proper disposal.

4.3 Experimental Results and Discussions

Fig. 32 illustrates examples of the Raman and Brillouin spectra acquired from different positions on a 48-hours-old zebrafish model. Four representing positions, including tail fin, head and two separate points in yolk sac, were selected. Those points were noted in Fig. 32(a) as well. Fig. 32 (b) and (c) show the acquired Brillouin spectra for the representing points. The integration for each measurement was 5 seconds. For all the cases, Brillouin peaks are visible. More importantly, the Brillouin shift shows heterogeneity within the embryo's body: the two yolk sac positions gave greater Brillouin shift (~ 8.50 GHz) compared to the other two points. Moreover, the tail fin's Brillouin was ~ 7.52 GHz, which was very close to water. This may be induced by the limited thickness of the fin, as it cannot fully fill the focal volume created by the objective lens. We also collected the Raman spectra for each point. The Raman spectra for yolk-sac show many peaks, both in the CH bond vibrational region (2800 – 3000 cm^{-1}), and in the signature region (600 – 1800 cm^{-1}), indicating that the yulk sac was composed by a variety of organic components (e.g., protein). Further analysis on the Raman spectra is required. Unlike the yolk-sac, the head gave a relatively simple Raman spectrum. Nevertheless, it still show a peak at ~ 2900 cm^{-1}, indicating the existence of the organic components. However, its signature region was almost featureless. This may be resulted by the limited concentration of the organic components.

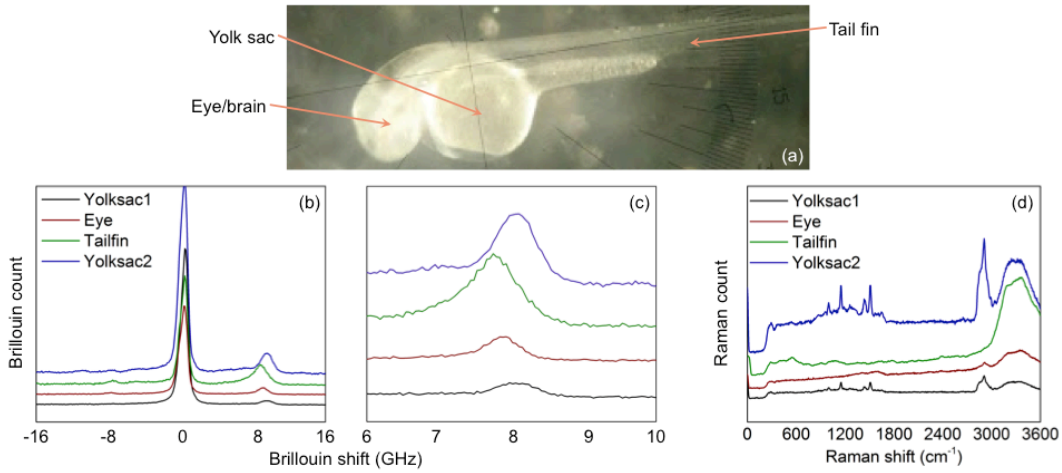

Figure 32 (a) Illustration of the regions employed the experiment; (b-c) Examples of the Brillouin spectra acquired from different regions as indicated in (a); (d) Examples of the Raman spectra acquired from different regions.

We made a statistical analysis of the Brillouin shift acquired from different regions. To do so, we adopted 5 zebrafish embryos, and selected 5 random points in each region of interest (head, yolk sac, and tail fin). The statistical result suggests that the Brillouin shift for those three regions were significantly different from each other (p<0.05, see Fig. 33).

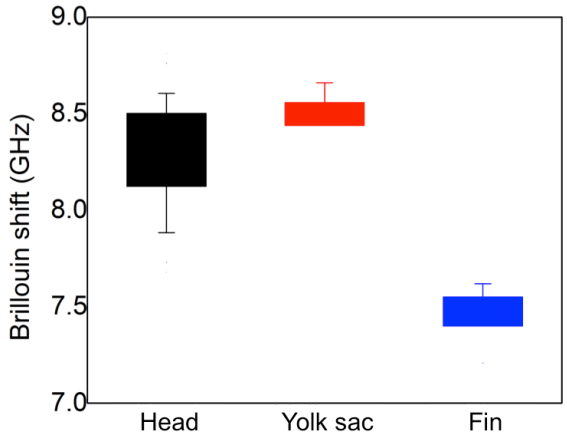

Figure 33 Statistical comparisons between the Brillouin shifts acquired from three regions: head, yolk sac and fin. The Brillouin shifts in these three regions were significantly different from each other (p<0.05, one-way ANOVA, Tukey's test).

Next, we tested the possibility of multi-dimensional imaging. To perform the experiment, we adopted a 10-hours-old embryo. In order to prohibit movements, the embryo was mounted in 1.2% low-melt agarose in fishwater on a glass slide. The glass slide was attached to a 2D translational stage (Micos Inc., model SMC MT-40 2D). The step size was set at 50 μm. The images are presented in Fig. 34. Fig. 34(a) presents the image obtained by the optical microscopy using the instruments shown in Fig. 21(a). Fig. 34(b) illustrates the Brillouin image for the embryo. Although the image is noisy, the morphology of the embryo could be identified. The positions of the yolk sac and the head can be recognized. Fig. 34 (c) illustrates the corresponding Raman image. Here, we plot the amplitude of the Raman peak at ~ 2910 cm^{-1} for each pixel. A morphological correspondence between the Raman and the Brillouin could be identified.

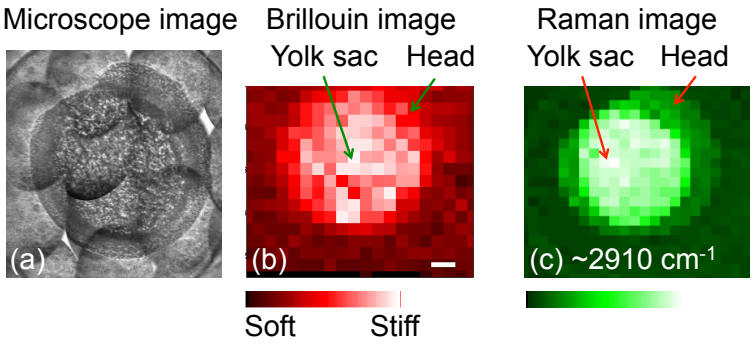

Figure 34 The images acquired from a 10-hours-old zebrafish embryo. (a) The optical microscope image. Due to the limited field of view provided by the objective lens, this is combined by multiple smaller images. (b) The Brillouin image of the same embryo. Here the step size was set as 50 μm.

We also performed a time-lapse imaging for the fish. We kept the zebrafish embryo alive after the test shown in Fig. 34. We performed multi-dimensional imaging at 14 hrs, 35 hrs and 48 hrs post federalization. The images are given in Fig. 35. The growth of the head and spin can be clearly observed as a function of time.

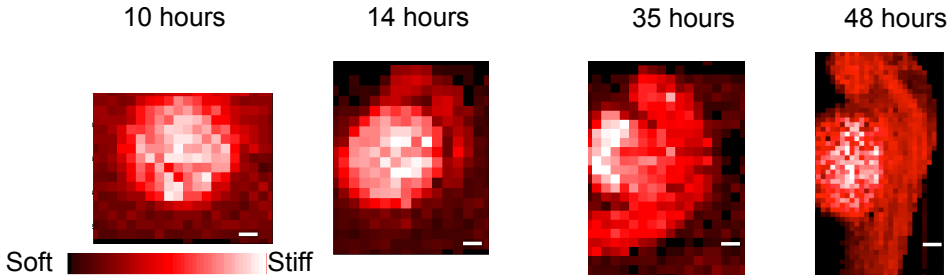

Figure 35 The images acquired from a zebrafish embryo at different ages (10, 14, 35 and 48 hrs.). The embryo kept growing after the images were taken. Scale bar: 200 μm.

We performed a more careful comparison between the Raman and the Brillouin spectra for the 48-hours-old embryo (see Fig. 36). The black background in each image refers to the surrounding medium, i.e., the mixture of agarose and water. During the scanning, we collected both the Raman and the Brillouin spectra. Multiple peaks could be identified from the Raman spectra. However, we only chose to map the distribution of the 2910 cm^{-1} and the 1550 cm^{-1} Raman peaks. Both Brillouin and Raman spectra portray the morphology of the embryo. However, the images obtained by the two imaging modalities are not purely identical, suggesting the Brillouin image is capable of describing information about the embryo in addition to Raman images.

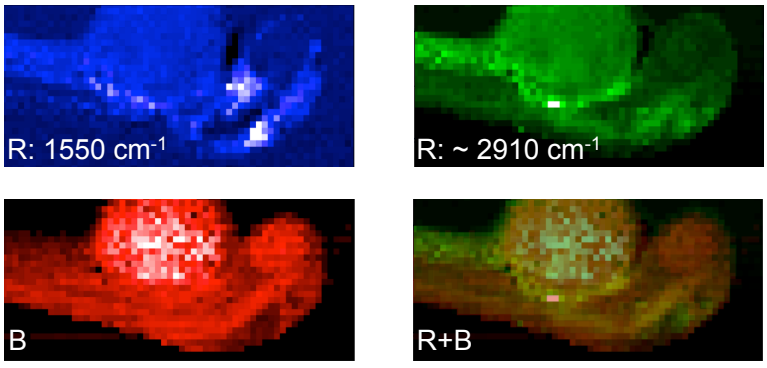

Figure 36 The Raman image (upper left and upper right), the Brillouin image (lower left) and the combination of the Brillouin and the Raman image (lower right) of a 48-hours-old zebrafish embryo. Brillouin image scale bar: 7.3 GHz – 8.5 GHz.

Fig. 37 presents the correlation between the ~2910 cm^{-1} Raman peak with the Brillouin shift. Each data point in Fig. 37 represents a pixel shown in Fig. 36. A weak linear correspondence can be observed between the Brillouin shift and the 2910 cm^{-1} Raman peak amplitude. Similar with the results shown in Fig. 24, the correlation between the Brillouin and Raman results cannot be described by a simple function. Therefore, again, Raman and Brillouin spectroscopy may reveal different source of contrasts.

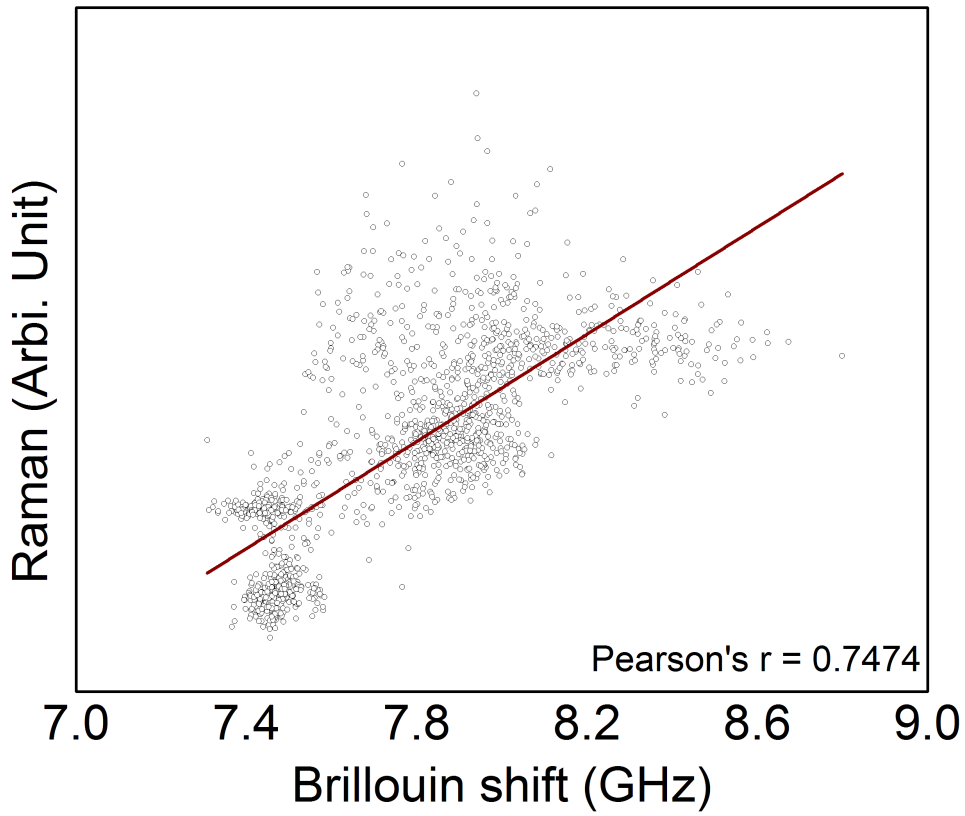

Figure 37 The correlation between the 2910 cm^{-1} Raman peak amplitude and the Brillouin shift (for Fig. 36d).

4.4 Summary

In this study, we proved that Brillouin spectroscopy could be utilized on probing whole body imaging applications. Specifically, with the assistance of Brillouin spectroscopy, we measured the viscoelasticity properties of different compartments of living zebrafish embryos, including yolk-sac, skin, spine and heart. Moreover, we also demonstrated the applicability of Brillouin microscopy in generating 2D images of living zebrafish embryos. In this sense, the whole-body Brillouin imaging is possible, and may bring investigators a new dimension in understanding the biological developmental process. With the assistance of the further developments in the experimental instrumentation (e.g., [104, 215-217]), we anticipate the wide application of Brillouin spectroscopy in the field of developmental biology and biomechanics.

CHAPTER V

APPLICATION ON ARTIFICIAL BIO-COMPATIBLE MATERIALS: IN SITU ASSESSMENT OF LOCAL HETEROGENEITY IN MECHANICAL PROPERTIES OF A BULK HYDROGEL NETWORK

5.1 Introduction

Unprecedented challenge and opportunity exist in developing new biomaterials for next-generation technological innovation including bioenergy, bioelectronics, basic biology, medical diagnostics, cancer research, and regenerative medicine. The complex relationships between biomaterial macro-function, physical properties and nanoscale materials interactions have emerged as a field ripe for development across the scientific community. Specifically, recent progress in nanotechnology has stimulated the development of multifunctional biomaterials for tissue engineering applications.[218-221] The physical properties of nanocomposite biomaterials play key roles in controlling cell fate, which underlines therapeutic success.[222-224] Conventional mechanical tests, including uniaxial compression and tension, dynamic mechanical analysis and shear rheology, require mechanical forces to be directly exerted onto the sample and therefore may not be suitable for *in situ* measurements or continuous monitoring of mechanical stiffness.[225-227]

In this chapter, we employ spontaneous Brillouin spectroscopy as a viscoelasticity-specific probing technique. We demonstrate for the first time that the dual Brillouin/Raman spectroscopy can be utilized as a non-invasive in situ technique to simultaneously investigate the mechanical and chemical properties of nanocomposite hydrogels. In this study, the sub-micron resolution of Brillouin spectroscopy enables assessment of the hydrogel's viscoelasticity at the mesolength scale (submicron, micro

and macro). The mechanical properties obtained from Brillouin spectroscopy were compared with conventional material characterization techniques, i.e., quasi-static shear rheology. By taking advantage of the non-contact nature of Brillouin spectroscopy, it is possible to determine mechanical properties of biological tissues and biomaterials under *in situ* and *in vivo* conditions.

5.2 Materials and Methods

To mimic different tissue stiffness, we synthesized polymeric hydrogels from denaturalized collagen (gelatin) by varying polymer concentration (Fig. 38a). Briefly, amine group present on gelatin backbone was modified with methacrylic anhydride to obtain photocrosslinkable gelatin methacrylate (GelMA), using previously reported methods.[228, 229] Covalently crosslinked GelMA hydrogels (3, 5, 10 and 15 %wt/v) were obtained upon UV exposure in presence of photoinitiator (Irgacure 2959).

Polymer hydrogels were prepared by covalently crosslinking them in the presence of UV light. Briefly, 3, 5, 10 and 15% GelMA were dissolved in 0.25% photoinitiator solution (Ciba® IRGACURE® 2959, Ciba Specialty -Chemical, USA) at 60˚C. The pre-polymer mix was then subjected to UV exposure (320-500 nm) (Omnicure S200, Lumen Dynamics, Canada) at an intensity of 1.44 W/cm^2 for 90 seconds to obtain covalently cross-linked hydrogels. Hydroxyapatite nanopowder purchased from Sigma Aldrich, USA was used to fabricate nanocomposite hydrogels. Briefly, 10% (w/v) solution of nHAp stock was prepared in distilled water and allowed to uniformly disperse under sonication for 15 minutes. 5% (w/v) solution of GelMA was prepared in photoinitiator solution and appropriate volume of nHAp stock was added to make the final volume up to 0.5, 1, 1.5, 2, 2.5, 3, 3.5, 4% respectively. The nanocomposite solution was then cross-linked under UV exposure at 1.44 W/cm^2 for 90 seconds to obtain nanocomposite hydrogels.

Scanning electron microscopy was performed to study the pore size distribution and wall thickness of polymer hydrogels / nanocomposites. Samples for SEM characterization were frozen in liquid nitrogen prior to lyophilisation for 36 hours. Completely dried samples were broken with forceps to expose the cross-section and mounted onto carbon taped SEM stubs. Samples were sputter-coated with Au/Pd (~31 nm) prior to imaging under SEM (JEM 5000 SEM, Nikon instruments) at an acceleration voltage of 10 kV. Pore size distribution and wall thickness of the samples were calculated using ImageJ (National Institute of Health, USA).

The viscoelastic properties of the polymer hydrogels and nanocomposites were analyzed using a MCR rheometer (Anton Paar, USA) equipped with a 10mm flat geometry. Time dependent storage and loss moduli (G' and G") were obtained by subjecting the material to 1% strain at 10 rad/sec. The UV light was turned on after 30 seconds and kept on until the moduli were stabilized (180 seconds). Strain sweep was performed where the material was subjected to 0.1-10% strain at 10 rad/sec and the respective stress response was obtained from the sample.

5.3 Results

The microscopic morphology of the hydrogels was investigated using SEM and all the hydrogel samples showed highly porous and interconnected network (Fig. 38b). The pore sizes range from 3 to 10 μm among all the samples (Fig. 39a). Interestingly enough, the wall thickness of the pores showed a positive correlation with the polymer concentration. The increase in wall thickness is attributed to higher wt% of polymer in the hydrogel network. It is expected that the increase in pore wall should reinforce the hydrogel network and result in an increase in mechanical stiffness.

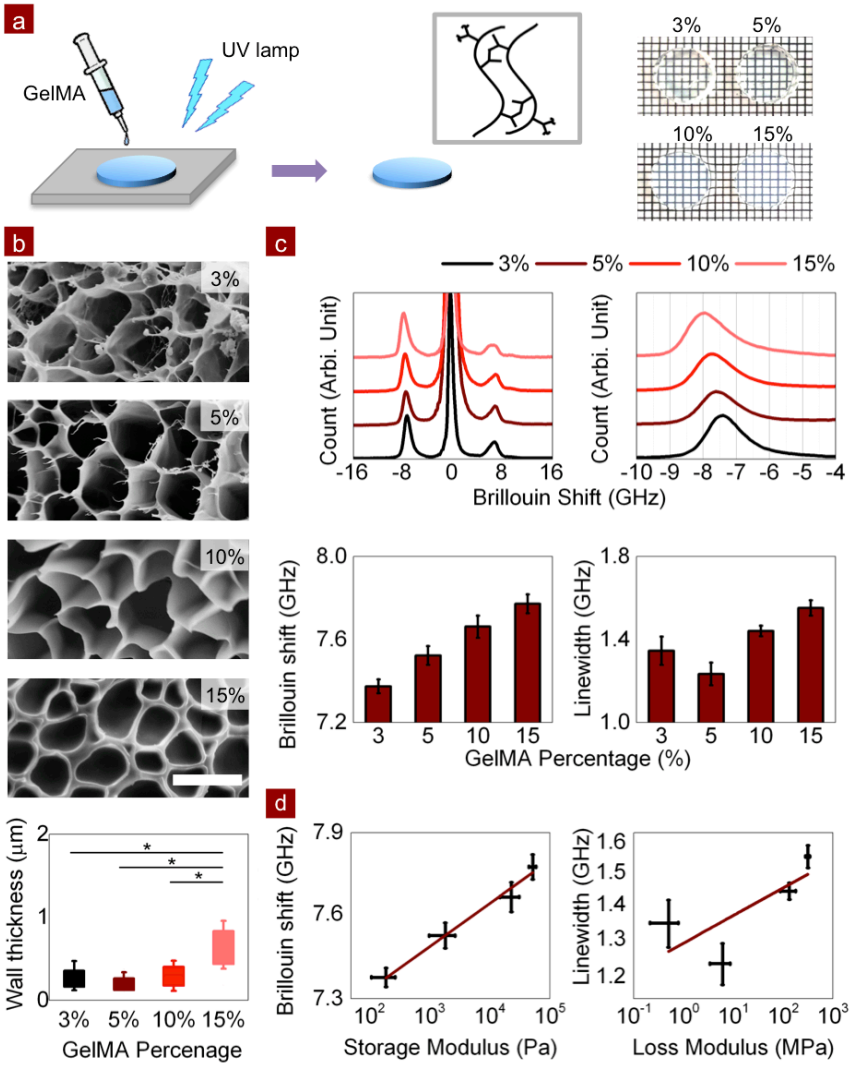

Figure 38 Investigating mechanical properties of polymeric hydrogel using Brillouin spectroscopy. (a) Covalently crosslinked hydrogels were fabricated from gelatin methacrylate (GelMA) by exposing the prepolymer solution to UV radiation. (b) Structural characterization of GelMA hydrogels indicates presence of highly porous and interconnected network (Scale bar = 10μm). The increase in polymer concentration results in an increase in the pore wall thickness. (c) Brillouin spectra for hydrogel samples with different polymer concentration. The effect of polymer concentration on Brillouin shift and linewidth was shown. (d) A positive correlation between the Brillouin shift and the storage/loss modulus was observed.

Next, we determined the viscoelastic and chemical properties of the hydrogel network using our dual Brillouin/Raman system. Examples of Brillouin and Raman spectra are given in Figs. 38 (c) and 39 (b-c), respectively. A typical Brillouin spectrum consists of

three peaks: one elastic peak located in the center, and two Brillouin peaks, including the Stokes and anti-Stokes components, located on left and the right side of the elastic peak (Fig. 38c). The Stokes peaks are zoomed in for better comparison in the right panel (Fig. 38c), to highlight the correlation between the GelMA concentration and the Brillouin shift. To quantify this correlation, we made a statistical study based on 25 measurements on 5 separate hydrogel samples. A positive correlation between the GelMA concentration and the Brillouin shift was observed and plotted in Fig. 38 (c) as well. Nevertheless, the Brillouin linewidth, which is associated with the sample's viscosity, does not strictly correlate with the GelMA's concentration (Fig. 38c, the lower right panel).

In order to connect the Brillouin spectroscopy with the conventional mechanical probing techniques, we also used shear-rheology to characterize the hydrogel network. The viscoelastic properties of hydrogel network can be defined by storage modulus (*G'*) and loss modulus (*G"*). Both the storage and loss moduli of the polymeric network increases with an increase in the GelMA concentration (Figs. 38d and 40). This is expected as the increased polymer concentration could enhance the crosslinking density. Moreover, the increase of the wall thickness of the hydrogel network may also contribute in enhancing the samples' stiffness.

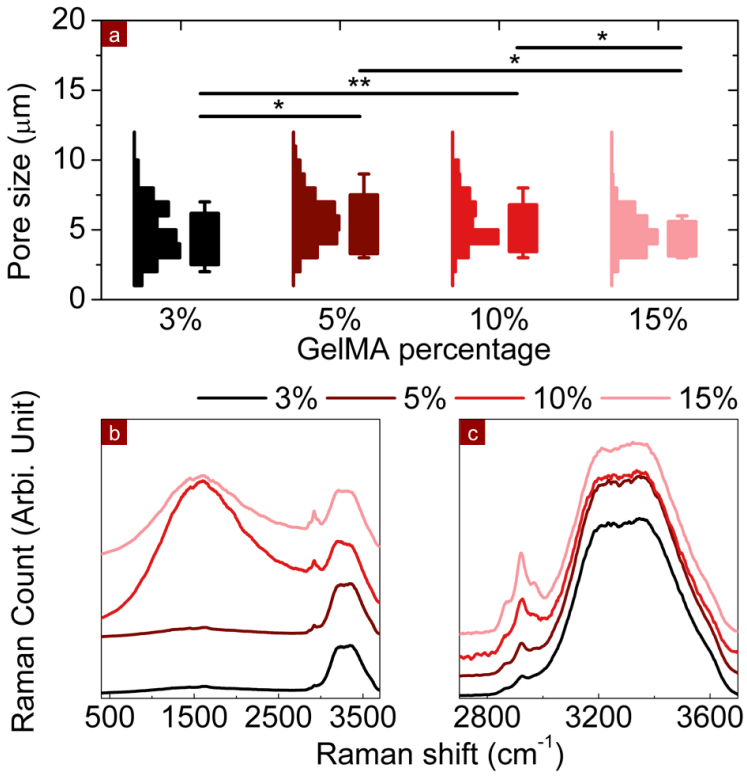

Figure 39 Additional characterizations for the pure GelMA samples. (a) Pore size distribution of pure GelMA hydrogels (Box: Mean ± standard deviation, whisker: 5% - 95%, *: p<0.01, **: p<0.05). The pore sizes are measured from SEM images. (b) The Raman spectra for different pure GelMA samples. (c) Raman spectra range from 2700 – 3700 cm^{-1} (The slow-varying fluorescence backgrounds have been subtracted). The Raman peaks located within this region indicates the presence of GelMA and water.

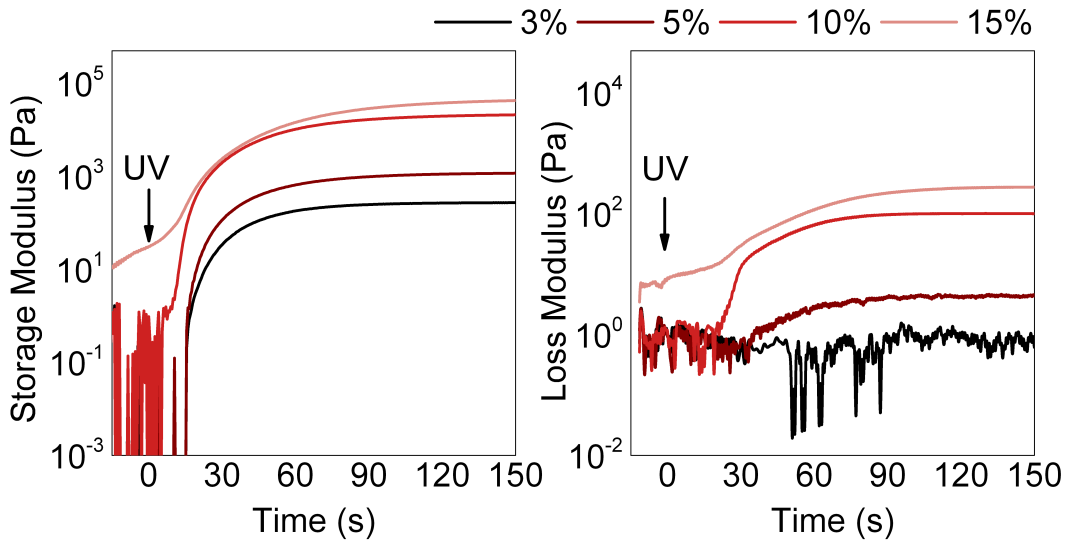

Figure 40 Time-dependent measurement of storage and loss modulus for pure GelMA samples. The data were collected by the rheometer. The gelation process was initiated by UV cross-linking. GelMA solutions with different mass percentage were tested. The x-axis (time) indicates the time elapsed from the beginning of the UV-cross-linking.

A positive correlation between the hydrogel modulus and Brillouin shifts was observed (Fig. 38d). Unlike static/quasi-static techniques such as shear rheology, Brillouin spectroscopy offers the sample's elastic modulus in high-frequency regime (~1-10 GHz). Due to the acoustic dispersion, the corresponding elastic modulus is much higher than those derived from conventional quasi-static techniques. Nevertheless, Brillouin moduli can be connected with conventional elastic moduli through an empirical power law: $M'_B = 10^b (M'_S)^a$ [45, 230]. Here, M'_B and M'_S are the Brillouin and quasi-static elastic moduli, respectively. a and b are material-dependent coefficients which need to be calibrated separately. Overall, we demonstrated that the mechanical stiffness of polymeric hydrogels could be determined using Brillouin spectroscopy in a non-invasive manner.

In order to further extend this technique towards the mineralized engineered tissue, we engineered hydroxyapatite nanoparticles (nHAp)-reinforced GelMA hydrogels. nHAp is a naturally occurring mineral component predominantly obtained in mineralized tissue

such as bone, dental enamel, and dentin. To mimic mineralized tissue, nHAp was incorporated (0 - 4 %wt/v) within the GelMA hydrogel prior to the photocrosslinking (Fig. 41a). The microstructures of nanocomposite hydrogels were characterized using SEM (Fig. 41 b & c). Similar to the pure GelMA hydrogels, porous and interconnected structures was observed in all the nanocomposite hydrogels. The microscopic morphology, including the wall thickness and the pore size of nanocomposite hydrogels, was dependent on nHAp concentration (Figs. 41c and 42a). To validate the presence of nHAp within the hydrogel network, we analyzed Raman spectra for the nanocomposite hydrogels (Figs. 41a and 42 b-c). Due to the strong autofluorescence emissions from the samples, we only illustrate a typical Raman shift for phosphate (ν_4 PO_4^- ~ 960 cm^{-1}) contributed by nHAp, amines (2600-3000 cm^{-1}) contributed by GelMA and OH bonds (~3100-3400 cm^{-1}) mainly brought by water molecules. Among the nanocomposite samples, we identified a positive correlation between the nHAp concentration and the phosphate peak (960 cm^{-1}) strength. At higher nHAp concentrations (> 3%wt/v), the amplitude of Raman peaks was weakened due to the increased turbidity of the sample.

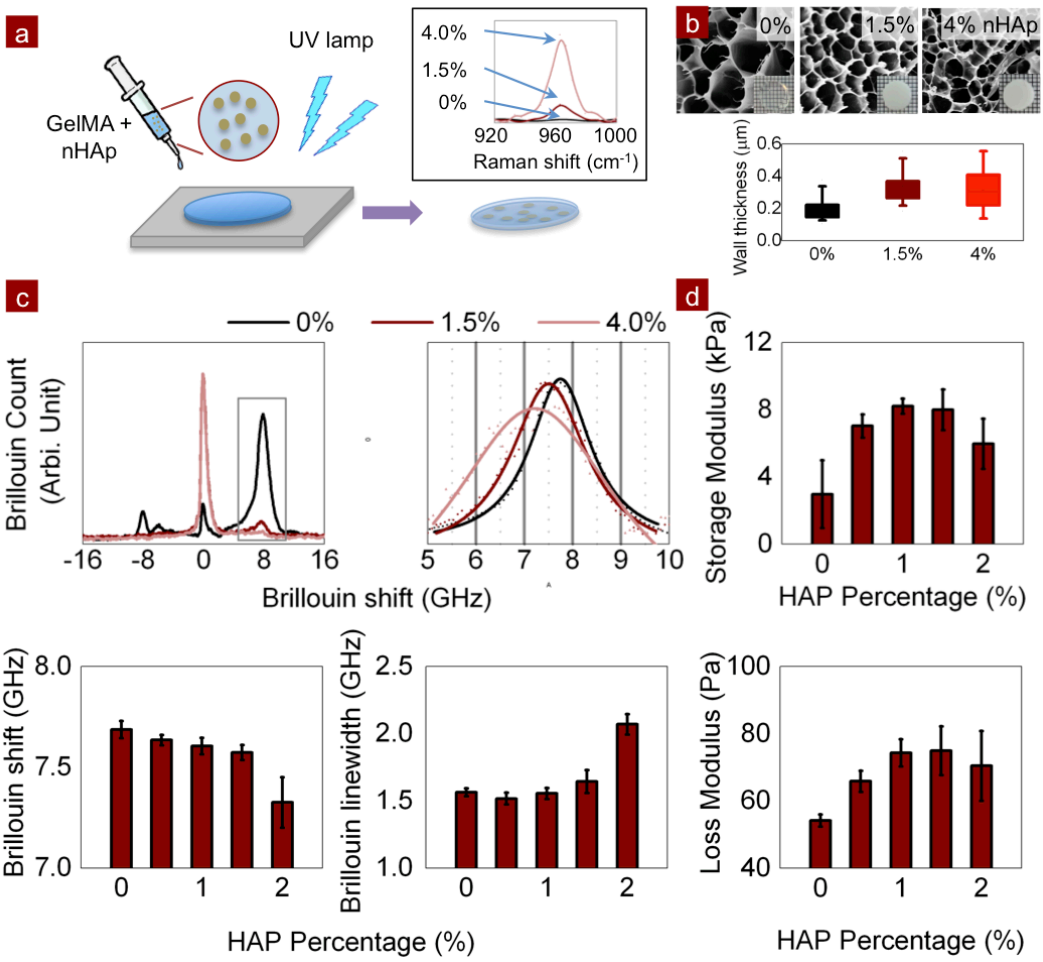

Figure 41 Investigating mechanical properties of nanocomposite hydrogels using Brillouin spectroscopy. (a) Fabrication process of nanocomposite hydrogel and inset show Raman spectra confirming presence of nHAp nanoparticles (~ 960 cm^{-1}, indicator of PO_4^-); (b) SEM images for nanocomposites with different nHAp concentrations and its effect on the wall thickness and pore sizes; (c) Left: Brillouin spectra, shifts, and line widths as a function of nHAp concentration; Right: the close up view of the anti-Stokes peaks, the elastic-scattering-induced background is removed; (d) correlation between the Brillouin spectroscopy results and the rheology results.

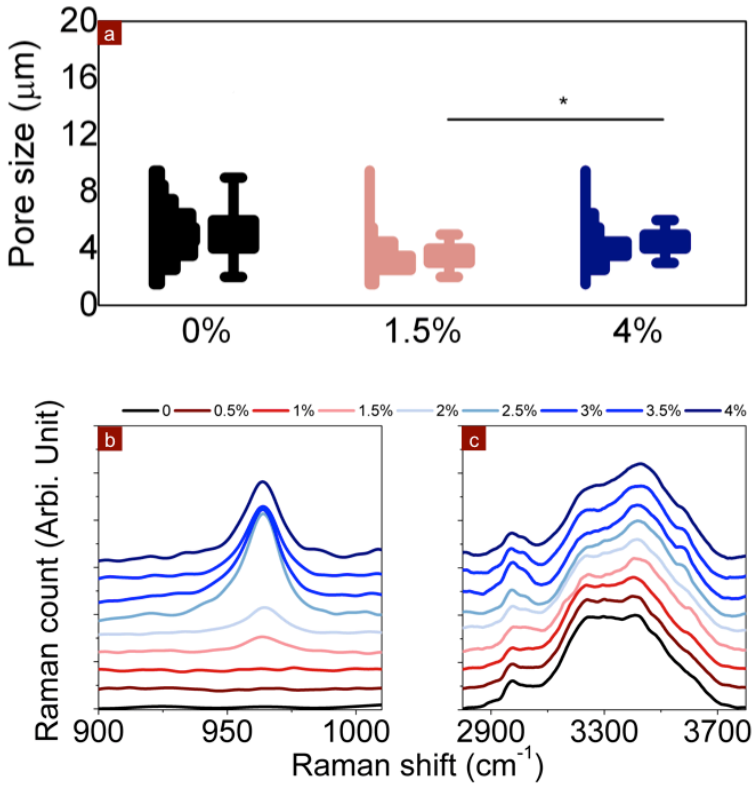

Figure 42 Additional characterizations for the nanocomposite hydrogel samples. (a) The pore size distribution (Box: Mean ± standard deviation, whisker: 5% - 95%). The pore sizes are measured from SEM images. (b) The Raman spectra for different pure GelMA+HAP samples. Here we choose to present the Raman peak at ~ 960 cm^{-1}, an indicator of HAP nanoparticles. Part of these data are included in Fig. 38. (c) Raman spectra range from 2800 – 3800 cm^{-1} (The slow-varying fluorescence backgrounds have been subtracted). The Raman peaks located within this region indicates the presence of GelMA and OH bonds. The slow varying autoflurorescence backgrounds have been removed in (b) and (c).

The Brillouin spectra for nanocomposite hydrogels were recorded and used to investigate the viscoelastic property of the hydrogel network. Due to the strong elastic light scattering from nHAp nanoparticles, the amplitude of elastic peaks of the nanocomposite was substantially elevated (Fig. 41d). The amplitude of the spectral wings of those elastic peaks was comparable to the one of Brillouin peaks. Therefore, when processing the Brillouin spectra, the background subtraction was necessary (Fig. 43). By locating the center of Brillouin peaks, the Brillouin frequency shifts were identified with a high accuracy. Nevertheless, the linewidth of the Brillouin shift was

affected by the limited signal strength, and was much broader than their pure GelMA counterparts (Figs. 41d, 43-44).

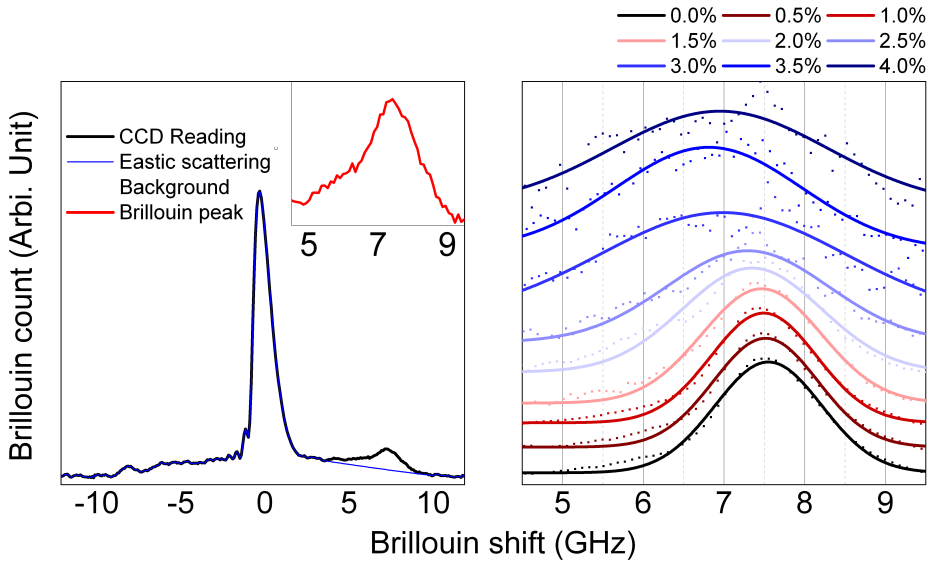

Figure 43 Examples of the Brillouin spectra for the nanocomposite hydrogel samples. Left: the raw Brillouin spectra of a GelMA + HAP sample (GelMA: 5%, HAP: 2.5 %). Compared with pure GelMA samples, the overall background for GelMA + nHAp samples was elevated due to the strong elastic scattering. When processing the data, we subtracted the slow varying background, and used Lorentz functional to fitting the peaks (the inset in the left panel). Right: The Brillouin spectra for the nanocomposite hydrogel samples with different nHAp concentrations. A consistent negative correlation between the Brillouin shift and the nHAp concentration can be observed. Detailed statistical comparison is given in Fig. 41.

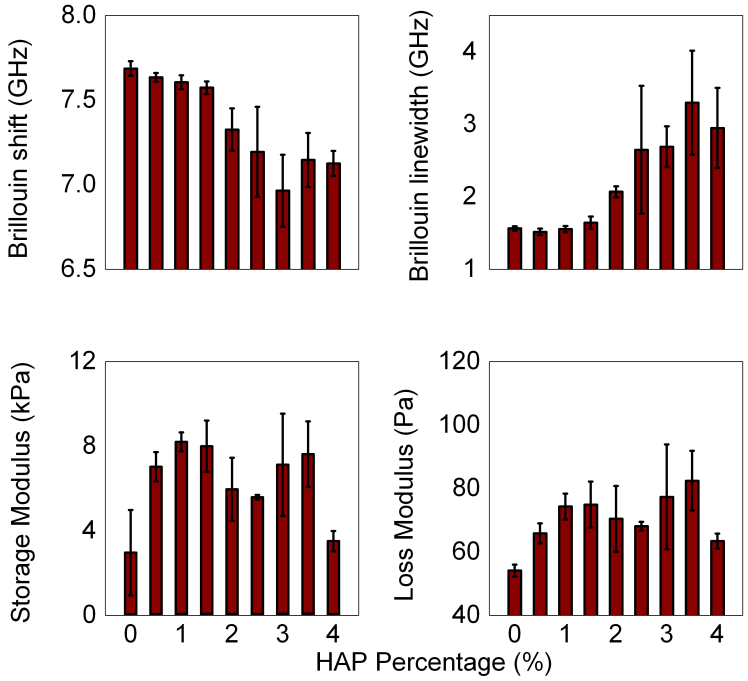

Figure 44 Additional characterization for the nanocomposite hydrogel samples. Here we utilized Brillouin spectroscopy (a and b) as well as the shear rheology (c and d). Part of the data is presented in Fig. 41. The Brillouin shift exhibit a monotonic negative correlation with the nanoparticle's concentration. Meanwhile, the Brillouin linewidth increases when the nHAp's concentration is elevated. Unlike the Brillouin shift results, the shear rheology shows a complex relationship with the nHAp's concentration.

A negative correlation between the nHAp concentration and the Brillouin shift is observed (Fig. 41e), indicating that the addition of nHAp results in a decrease in microscopic elasticity of the hydrogel network. This might be possible, since the presence of nHAp acts as physical filler and disrupts the formation of polymeric network. Moreover, nHAp is opaque and can adsorb the UV light during the crosslinking process. Therefore, when nHAp's concentration is elevated, the crosslinking efficacy may be reduced.

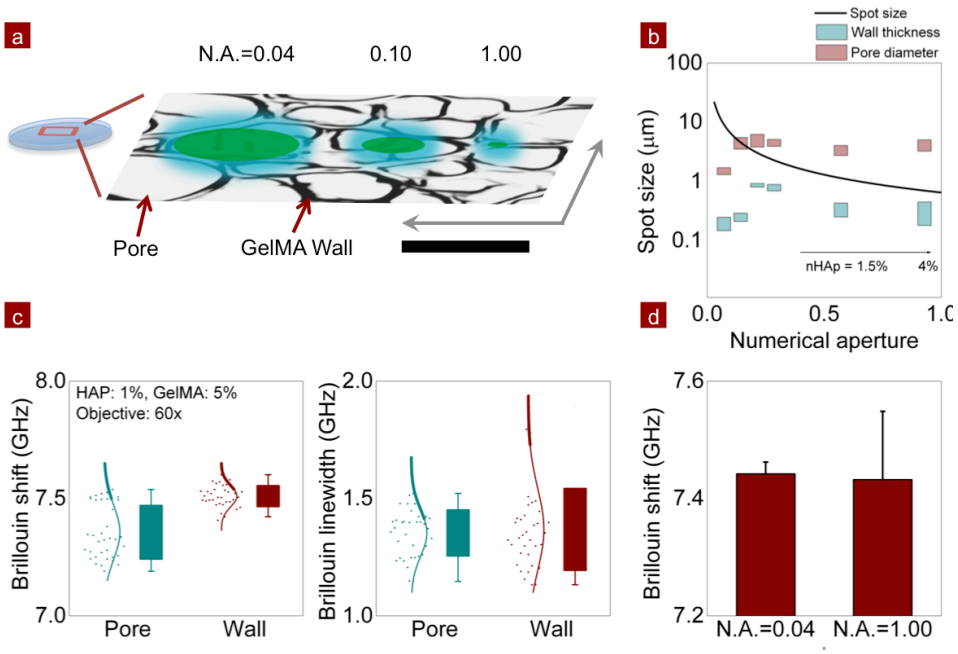

Figure 45 (a) Illustration of the relationship between numerical aperture and the corresponding focusing spot size; (b) Solid line: the focusing spot size as a function of the numerical aperture of the objective lens; Boxes: The measured wall thickness for pure GelMA and GelMA + nHAp samples are plotted as a reference. The left four pairs of boxes are measured from pure GelMA samples, the right three pairs of boxes are measured from nanocomposite hydrogel samples; (c) The Brillouin shift and linewidth for spots randomly selected from the sample; The numerical aperture of the objective was 1.00. (d) The statistics results of the Brillouin shift acquired from random points with different objective lens. The results corresponding to the higher numerical aperture objective lens gives a stronger fluctuation.

The quasi-static elastic modulus obtained from shear rheology is presented in Figs. 41(f) ad 44(c-d). The quasi-static storage and loss moduli exhibit a positive correlation with the nHAp concentration when it is lower than 2%. At higher nHAp concentration, no significant change in the storage and loss moduli was observed. At higher concentration, nHAp hinder the kinetic chain growth and interfere with the polymerization process supporting earlier results.[231, 232] This is different from the monotonic negative correlation between Brillouin shift and the nHAp's concentration. This contradiction may be prompted by the sample's heterogeneity in mechanical properties at different length scales. For example, in this study we used an objective lens (N.A.=0.25) that resulted in smaller spot diameter (< 5 μm) and subsequently lower probing light into a

microscopic volume. Therefore, the Brillouin shift obtained from the nanocomposite hydrogel could only provide the viscoelasticity information of microscopic region (< 5 μm), probably solely induced by the wall or the pore of the hydrogel network. The rheology technique, on the other hand, measured the samples' stiffness at the macroscopic (~ 10 cm) length scale. Thus, the elastic modulus is averaged over the entire volume of the sample. This result suggests that nanocomposite hydrogels show heterogeneous mechanical properties at different length scales.

To further validate the heterogeneity of the nanocomposite hydrogels, we acquired the values of Brillouin shift using objective lenses with different numerical apertures. The Brillouin spectroscopy is originated from the interactions between the incident photons and the internal phonons within the sample.[37, 133] Therefore, when probing inhomogeneous samples, the size of the focusing spot, a definition of the interaction volume, plays an important role in determining the Brillouin shift (Fig. 45a).[186] To investigate the relationship between spot size and Brillouin shift, we utilized two objective lenses with distinct numerical apertures (NA = 0.04 and 1.00) (Fig. 45b). Their corresponding focusing spot size is ~ 12 μm and ~ 0.5 μm, respectively. Based on the SEM images, it is expected that the larger spot size (NA = 0.04) will provide the averaged information over an area of 10 μm, including the walls and the pore region, whereas the smaller spot size (NA = 1.00) with spot size <1 μm, will cover only the walls or the pore centers (Fig. 45 a-b). To validate this hypothesis, we randomly selected 36 points on the nancomposite hydrogels (1% nHAp). The acquired Brillouin shift results are plotted in Figs. 45(c) and 46. When utilizing smaller focusing spot size, the Brillouin shift was more loosely distributed. The statistical comparison is given in Fig. 45(d). For low NA (~0.04) lens, the Brillouin shift was 7.4421 ± 0.0200 GHz and for high NA (~1.00) lens, the Brillouin shift was 7.4322 ± 0.1164 GHz. The averaged Brillouin shift acquired by the two objective lenses did not exhibit significant difference (p>0.05, Fig. 45d). However, the standard deviations of these two datasets were greatly different: the distribution of Brillouin shift of the datasets acquired by the high NA lens

is ~ 5 times more loosely distributed than the dataset collected by the low NA lens. This indicates that Brillouin shift is highly sensitive to the microscopic position in the nanocomposite hydrogel networks. This phenomenon also confirms that the nanocomposite hydrogels show heterogeneous mechanical properties. According to these results, Brillouin shifts depend on the spot size and thus highlight the ability of this technique to determine heterogeneous mechanical stiffness in nanocomposite hydrogel network.

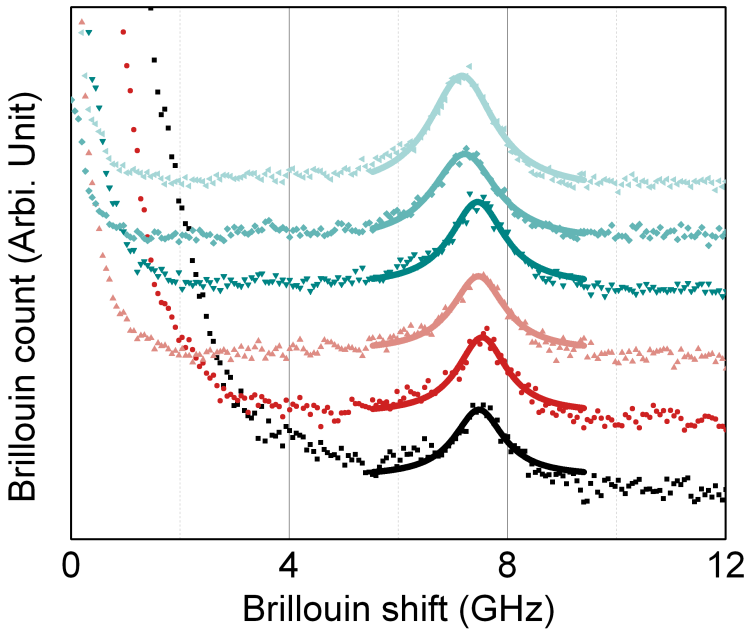

Figure 46 Examples of the raw Brillouin spectra for nanocomposite hydrogels (GelMA: 5%, nHAp: 1%). The Brillouin spectra were obtained by a high N.A. lens (N.A.=1.00) at 6 randomly selected positions. Fluctuations in Brillouin shift could be observed among the probing positions located in different positions.

5.4 Discussions and Summary

In conclusion, we have demonstrated that Brillouin spectroscopy is a unique approach in probing the heterogeneous viscoelasticity of biomaterials. The non-contact and noninvasive nature of Brillouin spectroscopy highlights can be used for *in situ* and *in vivo* applications to monitor tissue regeneration or cancer diagnostic or therapeutics. As a proof of principle, we have investigated the mechanical stiffness of pure polymeric hydrogels and nanocomposite hydrogels using Brillouin spectroscopy. For the pure polymeric hydrogels, Brillouin shifts were in agreement with the storage modulus of the hydrogel network obtained via conventional rheology. However, for hydrogels loaded with nanoparticles, a heterogeneous distribution of mechanical stiffness at micrometer length scale was observed. Unlike macroscopic characterizations, Brillouin spectroscopy provide new tool to probe the viscoelasticity of the hydrogel in mesolength scale, which ranges from sub-micron to tens of microns, which would help us better understanding the biomaterials' microscopic mechanical properties. This technique may facilitate future fabrication and *in situ* inspection of biomaterials for various biomedical and biotechnological applications.

CHAPTER VI

CELLULAR/SUBCELLULAR LEVEL APPLICATION: SUBCELLULAR MEASUREMENTS OF MECHANICAL AND CHEMICAL PROPERTIES USING DUAL RAMAN-BRILLOUIN MICROSPECTROSCOPY [*]

6.1 Introduction

Cellular- and subcellular-level optical spectroscopic techniques have become powerful tools in cell biology, as they provide a non-invasive approach capable of revealing cellular and subcellular compartments that cannot be visualized using conventional bright-field microscopes. Depending on the endogenous physical/chemical properties of interest, various spectroscopic approaches can be adopted. For example, nonlinear Raman microscopy enables imaging of molecular compositions, especially lipid membranes and proteins, at a subcellular level [12]. Second harmonic generation microscopy, a molecular-sensitive imaging technique, is widely utilized in imaging the stress fibers in cells [233] or extracellular matrices [234]. Photoacoustic microscopy (PAM) is capable of probing samples' optical absorbability. Recent advances in PAM enable acquisition of images with submicron lateral resolution and mapping of subcellular structures [235]. Many other techniques, including higher-order harmonic generation [236], stimulated Raman photoacoustic microscopy [198], and fluorescence-based techniques [237-239], also provide valuable physical/chemical information with subcellular spatial resolution.

---

[*] Reprinted with permission from "Subcellular measurements of mechanical and chemical properties using dual Raman‐Brillouin microspectroscopy" by Zhaokai Meng, Sandra C Bustamante Lopez, Kenith E Meissner, Vladislav V Yakovlev, 2015. Journal of Biophotonics, 9, 201-207, Copyright 2015 by WILEY‐VCH Verlag.

To date, non-invasive subcellular imaging techniques utilize a number of contrast mechanisms. However, one important physical property, viscoelasticity, cannot be imaged by any of the current optical techniques in a non-contact/non-invasive manner. Nevertheless, separate invasive techniques, including atomic force microscopy (AFM) [96] and optical tweezers [208], suggest that cellular level viscoelasticity is an important indicator of a cell's health state. Moreover, microscopic elasticity is usually distinct from its macroscopic counterpart [96-98], suggesting that probing on the microscale cannot be substituted by macroscopic techniques such as ultrasound elastography [78].

In this chapter, we demonstrate the capability of making cellular/subcellular measurements. To extend Brillouin spectroscopy into cellular/subcellular measurements, an objective lens with high numerical aperture (N.A.) is needed. Compared with tissue-level, or whole-body applications, two major hurdles emerge from this implementation. First, the smaller focal spot size leads to a smaller light-matter interaction volume and, consequently, lower signal strength. Second, since Brillouin shift depends on the scattering geometry, the linewidth of the Brillouin peaks is expected to broaden accordingly when a high N.A. objective lens is employed. This phenomenon complicates the retrieval of the Brillouin frequency shifts [240]. A recent numerical study revealed that the Brillouin linewidth is not significantly broadened when back-scattering geometry was adopted [186]. In this report, we take advantage of advanced instrumentation as described in Chapter 2, and extend Brillouin spectroscopy to probe single native and functionalized red blood cells (RBCs) at the microscale. Functionalized RBCs are being studied for long-term drug delivery [241] and blood analyte sensing [242] applications. Because the functionalized RBCs must stay in circulation for extended periods of time, knowing the mechanical properties and understanding how the properties are impacted by the functionalization process is critical to exploiting RBCs for healthcare applications. Raman spectra were also acquired using a conventional Raman spectrometer for each pixel as a reference.

6.2 Materials and Methods

The optical arrangement employed in this chapter follows the description set forth in Chapter 2. Here, we utilized a Nikon Fluor 60x objective lens (N.A. = 1.00) to achieve a tight focusing spot. In order to enable the acquisition of multidimensional images, we placed the sample on a computer-controlled translational stage (Thorlabs Inc, Model: MLS203-1). Theoretically, the image resolution is limited by the numerical aperture of the objective lens. In our setup, the spatial and axial resolutions of the Brillouin acquisition branch could approach ~ 400 nm and ~ 1 μm, respectively. Nevertheless, the scanning step size would dominate the image resolution if it were greater than the theoretical resolution. The pumping power at the sample was less than 40 mW for all the measurements. The sample cell's morphology and membrane integrity was maintained during the course of experiments. Prior to each spectroscopic acquisition, we utilized an optical microscope setup to determine the position of the focusing spot (Fig. 2.14a, inset).

In the set of experiments described here, we utilized two types of bovine RBCs the native RBCs and the RBCs encapsulating fluorescein isothiocyanate (FITC). The latter sample was loaded with FITC dye following published procedures [242]. Briefly, native RBCs were diluted in a hypotonic solution containing FITC-glygly, which initiates pore formation and allows cargo entrance inside the RBCs. Then the cell membrane was restored using a hypertonic buffer. Both the native and FITC-loaded RBCs were stored in Phosphate-buffered saline prior to analysis. Cells were inserted between a microscope slide and a cover slip, and the sample slide was placed on the translational stage for data collection.

6.3 Results and Discussions

We performed initial tests on native RBCs. An example of the bright field microscope images is shown in Fig. 47 (a). The 532 nm laser spot was also included. In this image, two RBCs can be identified. We randomly picked one RBC and acquired both Raman and Brillouin spectra at three different positions: 1. The liquid buffer in the vicinity of the RBC; 2. The cell's edge, which is mainly composed by lipid membrane and hemoglobin; and 3. The cell's center, which also contains lipid membrane and hemoglobin, but is much thinner than the cell edge [243]. These three positions are labeled in Fig. 2 (b). The Brillouin and Raman spectra are given in Fig. 47 (c) and (d), respectively.

The Brillouin spectra shown in Fig. 47 (c) contain three peaks. The center peaks (at 0 GHz) are resulted from elastic scattering processes. The other two peaks represent the Stokes (left) and anti-Stokes (right) Brillouin scattering processes, respectively. In this particular experimental setup, the shapes of the Stokes peaks were affected by an absorption band of the iodine cell. Therefore, when retrieving the Brillouin shifts, we only consider the anti-Stokes peak. The right panel of Fig. 47 (b) gives a closer view of the anti-Stokes peaks. Lorentzian fitting was applied to all peaks. In this particular test, the Brillouin shift for buffer liquid (7.50 GHz) is close to pure water (7.46 GHz). The other two regions possess greater Brillouin shift (7.60 and 7.92 GHz) compared to the buffer. The uncertainties of the Lorentzian fitting were 0.04, 0.03 and 0.05 GHz for the buffer, cell center, and cell edge, respectively. Depending on the position we focused on, the Brillouin shift of the cell also exhibits a fluctuation: the cell center gave a smaller shift than the cell edge. The corresponding Brillouin elastic modulus could be determined to be 2.25 GPa (buffer), 2.33 GPa (cell center) and 2.60 GPa (cell edge), respectively. Here, we assume the refractive index of the RBCs and the buffer liquid are 1.37 and 1.33, respectively [244]. The RBC's mass density (ρ) is assumed to be 1100 kg/m^3 [245]. The Brillouin modulus can be connected to the conventional static/quasi-

static elastic modulus through a power law: $M'_B = 10^b (M'_S)^a$ [45, 230]. Here, M'_B and M'_S are the Brillouin and quasi-static elastic moduli, respectively. a and b are material-dependent coefficients need to be calibrated separately. Based on this relationship, we get $\Delta M'_B/M'_B = a\Delta M'_L/M'_L$. Considering the uncertainties in our acquisition ($\Delta M'_B/M'_B \approx 0.6\%$), the Brillouin spectroscopy is capable of detecting ~18% change in conventional elastic modulus (assume a=0.032, following Scarcelli et al. [45]).

In these experiments, the linewidth of the Brillouin peaks was difficult to determine due to limited signal-to-noise ratio and was not analyzed. In order to enhance the signal quality and avoid possible thermal damage, we may take advantage of the so-called "biological window" [211] by selecting an NIR pumping source (e.g., 780 nm, [112, 212]) and increase the pumping power in future studies. Recent studies also imply the feasibility of surface enhanced Brillouin scattering using engineered metallic nano-substrates [142, 246]. We expect further elevation of Brillouin signal strength with this strategy.

The Raman spectra are shown in Fig. 47 (d) and enable another dimension of sample characterization. We illustrated the whole Raman spectra (0 – 2000 cm^{-1}) for each point. Multiple interferes, including the RBCs' autofluorescence emission and the Raman/fluorescence emissions of the glass slide, were picked up by the optical setup. Therefore, the overall reading of the spectra is elevated. Nevertheless, contrasts at ~ 1450 cm^{-1} and 1600 cm^{-1} still emerges. These peaks are indicators of hemoglobin, a protein molecule uniformly distributed in RBCs for carrying oxygen and CO_2 [243, 247]. The presence of hemoglobin is an indicator verifying our focusing position. The cell edge shows the strongest 1600 cm^{-1} peak, probably due to the increased RBC thickness near the cell edge. The thickness of the cell center (usually, < 1 μm [243]) is too thin to fill the entire focusing volume. Therefore, the hemoglobin's Raman peak at cell center was weaker than the cell edge. We also note that no explicit 1600 cm^{-1} peak can be observed in the buffer liquid. Based on the results shown in Fig. 47 (c) and (d), a

positive correlation between the Brillouin shift and the amplitude of the ~1600 cm^{-1} Raman peak can be identified. This result suggests that the elevation of Brillouin shift may be induced by the presence of hemoglobin. We note that the similar positive correlation between protein concentration and fluid elasticity has been reported in previous studies (e.g., [109, 150, 248]). The Brillouin shift may also be connected with the presence of lipid membrane. However, our current Raman data is insufficient to validate this hypothesis.

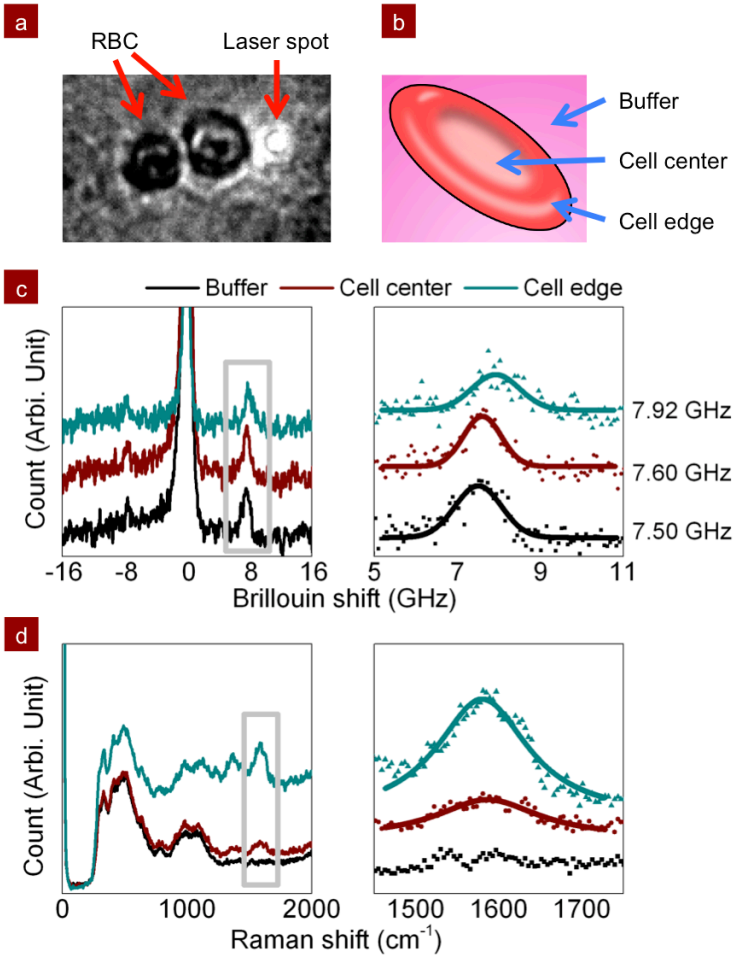

Figure 47 (a-b) The probing geometry of the test; (c) Examples of Brillouin spectra for different spots as indicated in (b); (d) Examples of Raman spectra for the spots shown in (b). The peak at ~ 1600 cm^{-1} is an indicator hemoglobin. All the data is collected from a native RBC. Integration time: 5 s, excitation power: up to 35 mW.

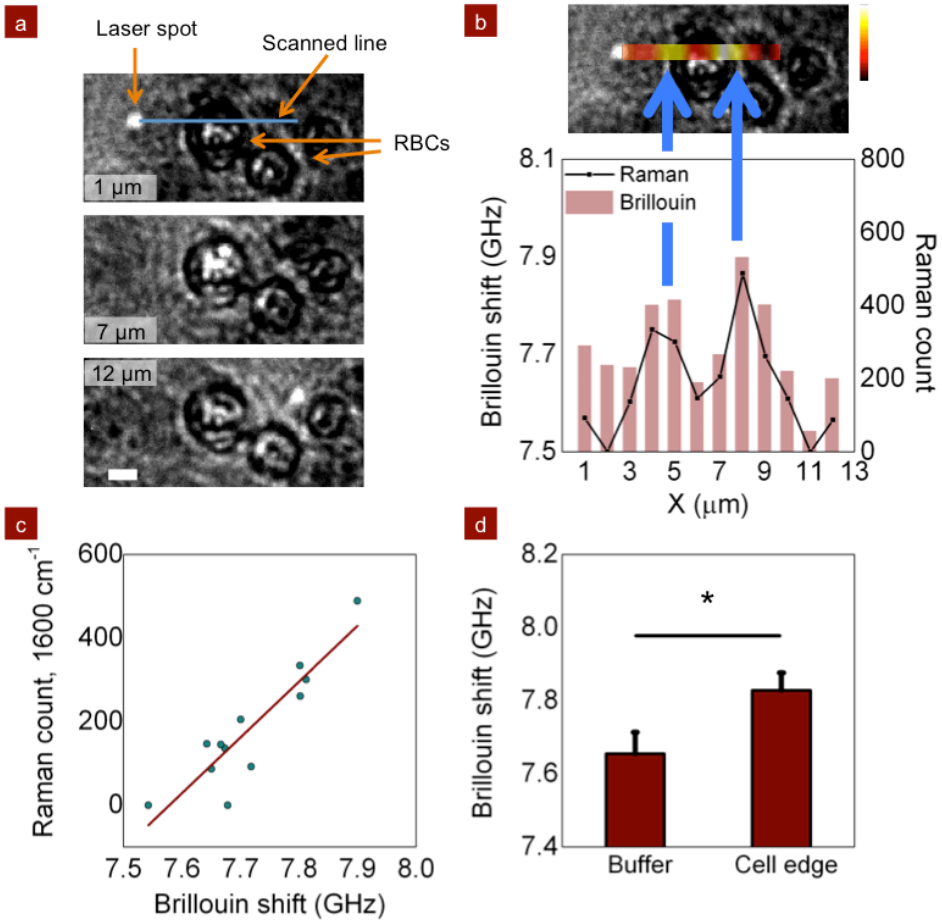

Figure 48 (a) The microscope images were taken prior to, during, and after the Brillouin/Raman acquisitions. 1, 7, and 12 μm refer to the relative position of the translational stage when taking these images. Scale bar: 2 μm; (b) The retrieved Brillouin shift and 1600 cm^{-1} Raman peak amplitude as a function of its relative position; (c) Linear correlation analysis between the Brillouin shift and the 1600 cm^{-1} Raman peak (Pearson's r = 0.9026); (d) Statistical analysis and comparison between the Brillouin shift of the buffer liquid and cell edge (one-way ANOVA, *: p<0.005). Integration time: 5 s, excitation power: up to 35 mW.

We also probed the Brillouin shift and Raman spectrum along a straight line across an RBC (Fig. 48). The probing geometry is shown in Fig. 48 (a). The microscope images were taken prior to, during, and after the Brillouin/Raman acquisitions. The diameter of the sample RBC was ~5.2 μm. When taking the data, we used the piezo translational stage to control the position of the sample. The length of the scanned line was 12 μm, and the stepsize was 1 μm. Fig. 48 (b) compiles the Brillouin shifts for all the data

points. The Raman peak height at 1600 cm^{-1} is also included. Although not as dramatic as Fig. 47, we see a similar result: the edge of the cell gives greater Brillouin shift while the surrounding buffer and cell center give lower Brillouin shift. With a peak-fitting algorithm (based on Lorentz function), the widths of the cell edge are found to be 0.82 μm (left) and 2.74 μm (right), respectively. This asymmetric geometry may be induced by the limited spatial resolution of the imaging system. In our current system, the lateral resolution is limited by the scanning step size (1 μm). It can be further improved with a finer scanning in future studies. The Raman acquisition again suggests a positive correlation between the existence of hemoglobin and the Brillouin shift. The linear correlation analysis is given in Fig. 48 (c). Statistical results also suggest that the difference between the buffer and cell edges is significant (Buffer: 7.65 ± 0.06 GHz, Cell edge: 7.83 ± 0.05 GHz; $p < 0.005$, one-way ANOVA; results are plotted in Fig. 48d). However, the difference between the Brillouin shifts for cell centers and the buffer were not statistically significant. This may be an artifact induced by the limited confocality of the system. Compared with human RBCs, bovine RBCs are ~ 30% smaller but possess the similar geometry. Given the central thickness of human RBCs to be ~ 0.9 μm (in normal plasma osmolality, 300 mOsm), the thinnest part of the bovine RBC should be ~ 0.6 μm only [249, 250]. On the other hand, the axial resolution in our imaging system is ~ 1 μm. When taking the Brillouin/Raman acquisitions at the cell center, the sample cell could only fill up to ~ 60 % of the entire focusing volume. The buffer liquid contributed to a portion of the Brillouin shift. This artifact is less likely to emerge when measuring cell edges, as the thickness (~ 1.8 μm) is sufficient to fill the entire focusing volume.

In this experiment, the scanning procedure was limited by the adherence strength between the RBCs and the glass slide. Unfortunately, the RBCs were difficult to spatially fix for extended time duration. Therefore, we only performed a one-dimensional scanning over the sample RBC. Nevertheless, systematic intracellular Brillouin shift fluctuations have been demonstrated in Fig. 47. With better signal quality, two-dimensional images could be collected in future studies. The cell lifetime could also

be substantially elongated with appropriate environment control (temperature, pH and CO_2 level, etc.). In this way, multi-dimensional scanning could be performed over an extended duration.

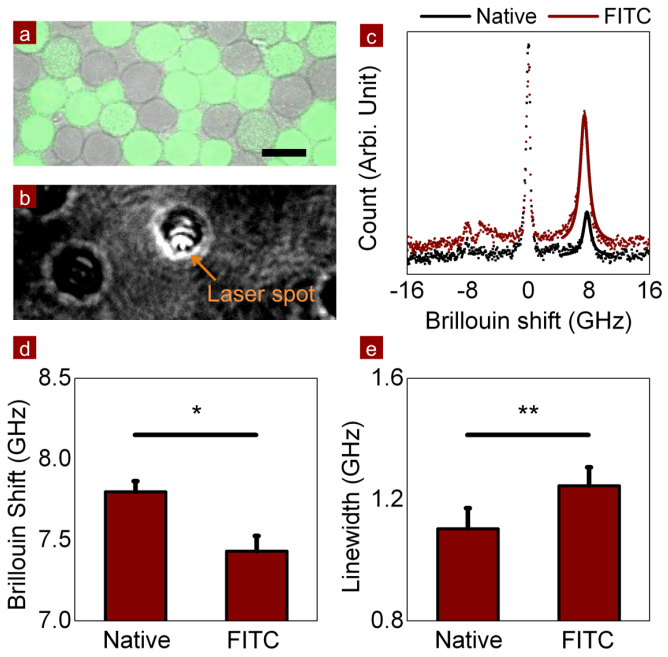

Figure 49 (a) Bright field fluorescence image of the FITC-labeled RBCs (scale bar: 5 μm); (b) Bright field optical microscope images for the FITC-labeled RBCs and the measurement geometry; (c) Examples of the Brillouin spectra for two types of the cells; (d-e) Statistical studies of the Brillouin shift and linewidth for the native and FTIC RBCs (one-way ANOVA, *: p<0.005, **: p<0.05). Integration time: 5 s, excitation power: up to 35 mW.

In addition to native RBCs, we also assessed the Brillouin shift for RBCs functionalized with FITC. The functionalization process removed ~95% of the hemoglobin and, thus, altered the morphology and composition of the cell. A representative fluorescence image of the functionalized RBCs is shown in Fig. 49. The excitation and emission wavelengths were 495 nm and 519 nm, respectively. For comparison with native RBCs, the laser spot was focused at the cell's edge as shown in Fig. 49(b). The raw Brillouin spectra from both the native and functionalized RBCs are plotted in Fig. 49(c). The Brillouin frequency shifts were distinct for the two cell types. In order to enable

statistical studies, we extended the measurements to 25 different cells in each group. The statistical results are presented in Fig. 49 (d) and (e). The averaged Brillouin frequency shift for the functionalized RBCs is ~300 MHz smaller than the control (functionalized: 7.43 ± 0.09 GHz, native: 7.80 ± 0.07 GHz). Compared to the data shown in Fig. 47, improved signal quality enables us to further test the Brillouin linewidth of the acquired spectra. The line-width increased by ~ 150 MHz after functionalization, suggesting an elevation in the cells' viscosity (functionalized: 1.25 ± 0.06 GHz, native: 1.10 ± 0.07 GHz, Brillouin loss modulus difference: ~ 59 MPa). Similar to the results presented in Figs. 47 and 48, the correlation between hemoglobin and Brillouin shift emerged again; further validates the hypothesis that the presence of hemoglobin may help to strengthen the cell's elasticity.

6.4 Summary

In this study, we demonstrated the proof-of-principle that Brillouin microspectroscopy can be employed to study the microscopic elasticity of individual cells. Intracellular elasticity fluctuations have been identified on native RBCs with Brillouin shifts from the cells edges being greater than those from the cell centers. The Brillouin shift is found to be positively correlated to the presence of hemoglobin. Experimental results also suggest that the fluorophore functionalization alters the Brillouin frequency shift of the RBCs, i.e. affects its elasticity. By introducing multidimensional scanning, we anticipate the wide use of Brillouin microspectroscopy in subcellular imaging and cell biology.

CHAPTER VII

COHERENT BRILLOUIN SPECTROSCOPY AND MICROSCOPY: HIGH-SPEED ELASTICITY IMAGING/SENSING USING NONLINEAR BRILLOUIN IMAGING/SENSING VIA TIME-RESOLVED OPTICAL (BISTRO) MEASUREMENTS [*]

7.1 Introduction

In previous chapters, we have demonstrated that the detection and analysis of spontaneous thermal phonons by means of spontaneous Brillouin spectroscopy is a promising emerging technique to gain a fundamental understanding of biological function on cellular, tissue and whole-body level [94, 95, 251]. More importantly, spontaneous Brillouin spectroscopy is capable of probing a target's mechanical properties in a non-contact and non-invasive manner, which is essential in biomedical imaging/sensing applications. Therefore, Brillouin spectroscopy provides a viable pathway to viscoelastic characterization on a microscopic scale without any mechanical perturbations.

However, the signal strength of spontaneous Brillouin spectroscopy is fundamentally limited by a weak interaction of the incident phonons within a biological sample. When taking microscopic measurements, the throughput of the system is defined by its acquisition speed. Therefore, spontaneous Brillouin spectroscopy cannot be efficiently

---

[*] Reprinted with permission from "Flow cytometry using Brillouin imaging and sensing via time-resolved optical (BISTRO) measurements" by Zhaokai Meng, Georgi I Petrov, Vladislav V Yakovlev, 2014. Analyst, 140, 7160-7164, Copyright 2015 by Royal Society of Chemistry.

implemented for flow cytometry applications (>1000 cells per second), which may be beneficial for diagnosing blood cell diseases or cancers due to the distinct elastic properties of healthy and diseased/tumor cells [252, 253].

Coherent Brillouin spectroscopy offers a new dimension to Brillouin imaging and sensing by involving parametric interaction of optical and acoustic waves. Similar to coherent Raman spectroscopy and many other multiphoton imaging techniques, an excitation volume is confined to a focal volume of the incident laser beams, and a transition from nonlinear Brillouin spectroscopy to nonlinear Brillouin microscopy is seamless [1, 58, 63, 216, 254, 255]. Specifically, impulsive stimulated Brillouin spectroscopy (ISBS) introduced by Moog et al. [255] and Kinoshita et al. [64] provides a much stronger signal strength.

In this chapter, we followed the basic framework of Kinoshita et al. [64]. We employed a 532 nm pulsed laser as the pump and a 780 nm continuous-wave laser as the probe. In the previous instrumentation implementations, the relative angle between the pump and probe beam has to be precisely tuned, as the angle between the probe beam and the optically generated acoustic wave should strictly follow the Bragg condition [64, 254, 256]. In this study, we introduced an external transmission grating to prepare the angle between the pump and the probe. In doing it this way, the Bragg condition are automatically satisfied, and the alignment and long-term maintenance of the optical setup is greatly simplified [215]. We coined a term BISTRO measurements (Brillouin Imaging and Sensing via Time-Resolved Optical measurements) reflecting both the physical principle behind this technique and the rapid assessment of Brillouin spectra. As a proof-of-principle, we validated this new experimental arrangement for microscopic imagingas well as flow cytometry applications. Material-specific BISTRO spectra exhibited an excellent correlation with spontaneous Brillouin spectra and were able to retrieve the correct information about the speed of sound in all studied materials. The experimental results also demonstrated the robustness of the setup, since no

realignment was necessary through the whole set of experiments. The utilization of flow capillaries enabled BISTRO's future applications in the field of fluid/cell cytometry.

7.2 Experimental Approach

A schematic sketch of the underlying principle of the experimental setup is illustrated in Fig. 50. The BISTRO measurement relies on the transient acoustic grating generated by the pump lasers. The grating-formation diagram is shown in Fig. 50 (a). Two pump laser pulses at the wavelength λ are intersected within the sample at an angle θ. Due to the photostriction or photothermal effect, a spatially varying number density distribution, which follows the sinusoidal optical interference pattern produced by the two pumping beams, is created [257]. Since the sample's index of refraction depends on the number density, a transient optical diffraction grating is formed. A pair of counter-propagating acoustic waves, whose wavelength matches the interference pattern of the two pumping beams, is formed. In this case, the wavelength of the acoustic wave is given by $\mathrm{d}' = \lambda_1/2\sin(\theta_1')$.

The counter-propagating acoustic waves will last for some time, causing a time-dependent, spatially periodic variation in the material density. As a result, the illuminated region of the sample behaves like a time-dependent Bragg diffraction grating, which can be monitored by time-dependent Bragg diffraction using a probe laser (see Fig. 50b). Once the geometric relation between the acoustic wave and the probe laser satisfies the Bragg's condition, i.e., $\sin\theta'_2 = \lambda_2/2\mathrm{d}'$, the probe beam will be diffracted by the acoustic wave. By evaluating a time-varying diffracted signal, the properties of the acoustic wave, including its frequency and speed, can be extracted. The longitudinal modulus of the sample can be calculated accordingly.

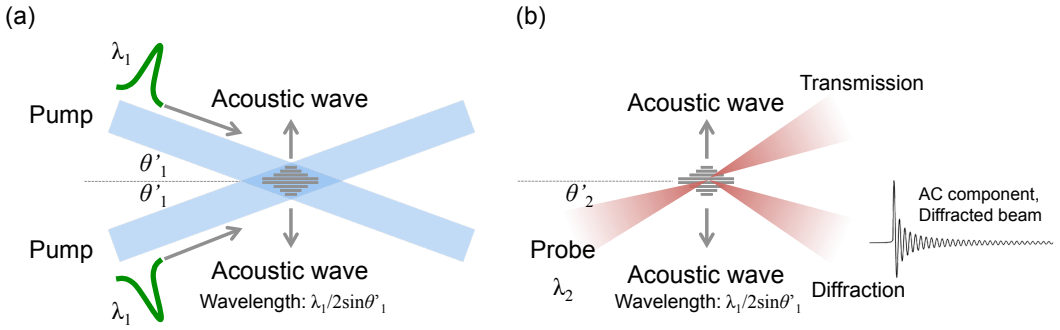

Figure 50 The principle of the BISTRO experiment: (a) The pumping process, and (b) the probe process.

The experimental setup of the BISTRO system is given in Figure 51. We employed two independent lasers to serve as the pump and the probe. At first, a 532 nm nanosecond pulsed laser was utilized as a pump laser (IPG Photonics Inc., Model: GLPR-10). The pulse duration was 1 ns, and the energy per pulse was up to 16 μJ. The repetition rate of the pump laser was adjustable in the broad range, but, for the purpose of these experiments, it was set at 20 kHz unless otherwise specified. The probe laser was a single-wavelength diode laser (wavelength: 780 nm, Newport Inc., TLB-6900). The output power of the 780 nm probing laser was ~ 5 mW. The total laser power utilized in this study was up to ~ 350 mW.

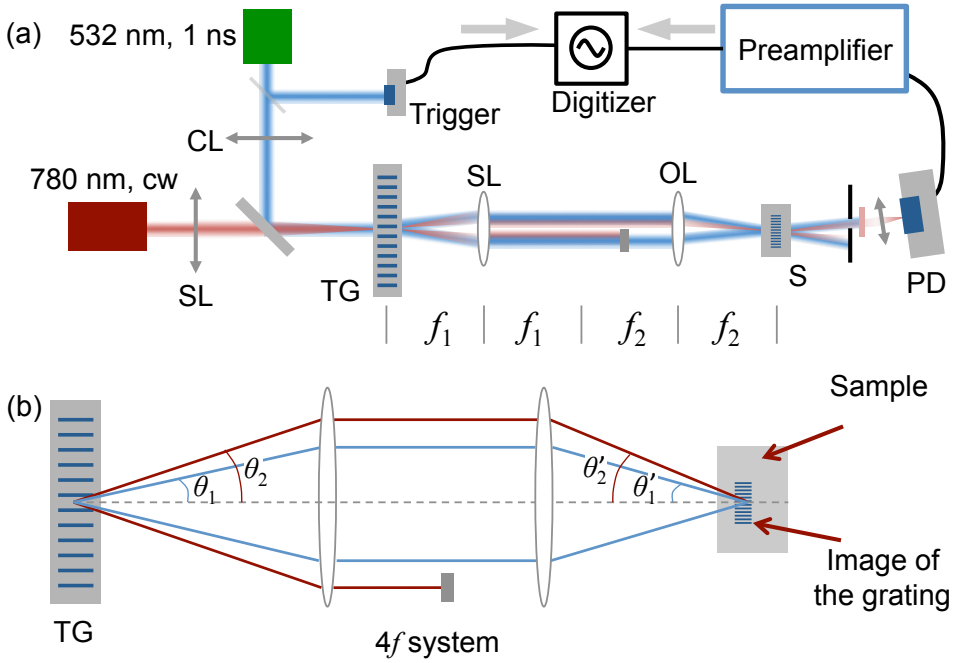

Figure 51 (a) The basic optical setup for the described experiment. CL: cylindrical lens; SL: spherical lens; TG: transmission grating; OL: objective lens; S: sample. (b) The image of the transmission grating was written in the sample via the 4*f* system, which includes the spherical lens and the objective lens.

The pump and probe laser sources were combined by a dichroic mirror and sent to a transmission grating (Holo/Or Ltd., DS-006-Q-Y-A, 41.67 lines/mm). A cylindrical lens was inserted in the optical path of the pump laser to focus the pump beam on the transmission grating into a line instead of a point. The orientation of this line focus was perpendicular to the strips of the grating. The probe laser was focused at the center of the line focus of the pump beam. Both the pump and the probe beams got diffracted off this grating, and we utilized the +1st and -1st orders of this diffraction. The diffraction angle for the pump beam can be calculated: $\sin\theta = \lambda/\mathrm{d}$, where d = 24 μm is the grating period and λ=532 nm the optical wavelength pf the pump beam. The pump and the probe beams were diffracted and propagated in different directions due to their distinct wavelengths. The diffracted beams were then sent to a 4*f* imaging system, which was formed by a spherical lens (f_1 = 15 mm) and an objective lens (10X Olympus Plan Achromat Objective Lens, N.A. = 0.25, working distance = 10.6 mm). We treated the

objective lens as a simple lens with a focal length f_2. The +1st and -1st orders of the diffracted pump laser beam intersect at the focusing point of the objective lens and form an interference pattern [63, 254, 258]. Taking into account the angular magnification of the system, the intersect angle (in air) could be calculated as: $\sin\theta'_1 = (f_2/f_1)\sin\theta_1$.

Acoustic waves are generated the intersecting pumping beams. The wavelength of the acoustic wave will be: $d' = \lambda_1/2\sin\theta'_1 = (f_2/f_1)d$. The 4*f* imaging system transfers the transmission grating into the interference pattern on the sample. The lateral magnification this image is f_2/f_1.

On the other hand, the probe laser beam was focused by the objective lens and transmitted through the transient acoustic grating. The incident angle of the probe beam can be calculated as: $\sin\theta'_2 = (f_1/f_2)(\lambda_2/d) = \lambda_2/(\lambda_1\sin\theta'_1) = \lambda_2/2d'$. As a result, the Bragg condition was automatically satisfied [256]. The probe beam was diffracted by the transient acoustic grating in the focusing region and detected by a fast photodiode.

In this particular study, we focused on the application of fluid cytometry and multi-dimensional imaging. For the fluid cytometry application, we microfluidically pump various simple liquids through a microchannel (Translume Inc, Model: YSF-100250-L8-500-250-500, illustrated in Fig. 52a). The microchannel was adjusted in such a way that it overlapped with the focusing stripe of the pump laser. Therefore, an acoustic grating could be generated inside of the microchannel. When making multi-dimensional imaging, the sample was attached to a translational stage. By scanning the translational stage, the viscoelasticity of the sample can be mapped in all three dimensions. At this point, this translational stage was the major limiting factor in scanning speed. In future studies, the mirrors described in Fig. 52 (a) will be replaced with galvo scanning mirrors to accomplish much faster imaging. The imaging geometry is shown in Fig. 52 (b-c).

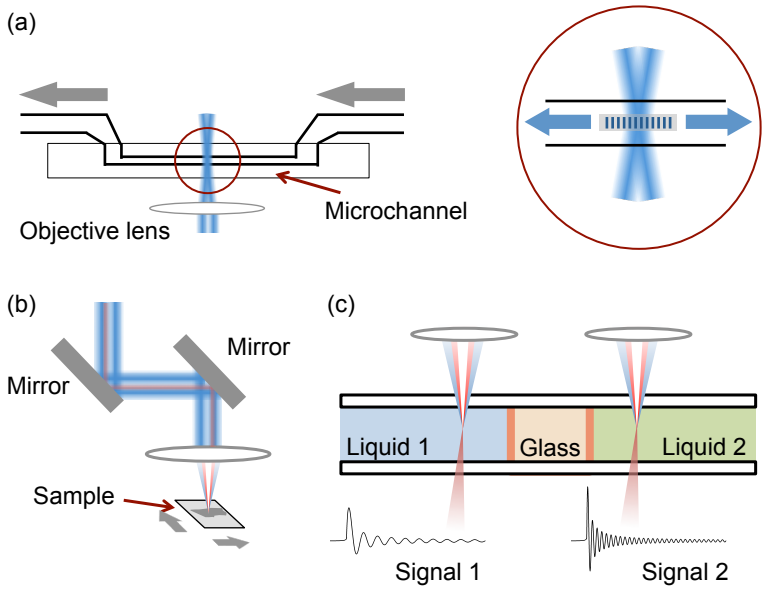

Figure 52 The experimental arrangement for flow cytometry and multidimensional imaging applications. (a) The flow cytometry application: The geometric relationship between the objective lens and the micro-fluid channel; (b-c) The multi-dimensional imaging application; (b) The geometric relationship between the objective lens, pump/probe beams and the sample. The mirrors can be replaced by galvo mirrors in order to accelerate the imaging speed; (c) The close-up illustration of the focal point. Based on the sound speed, different types of liquids will provide BISTRO signals at different frequency.

7.3 Demonstrative Results

Fig. 53 illustrates a typical oscilloscope output when the measurements were acquired from a bulk sample. In this study, the sample was placed in a stationary cuvette. The data presented in Fig. 53 were directly taken from the screenshot of the oscilloscope. A typical dataset was averaged over 128 pump pulses. The AC component of the detector's output was amplified by a high-frequency preamplifier (SRS445A, up to 625x gain, Stanford Research Systems) and was digitized by an oscilloscope (Rigol DS 6202, 600 MHz bandwidth). The recorded signal was ~ 10 mV (peak to peak voltage). A typical oscillation lasts for about 300 ns, which suggests that those measurements can be

potentially taken every 1 microsecond without any loss of the signal's integrity. The real-time FFT analysis results are also included in the figure. Here we only plot the magnitude of the FFT results. Other peaks, including environmental noises, were observed in the FFT spectra; however, we were interested in the sample-specific peak.

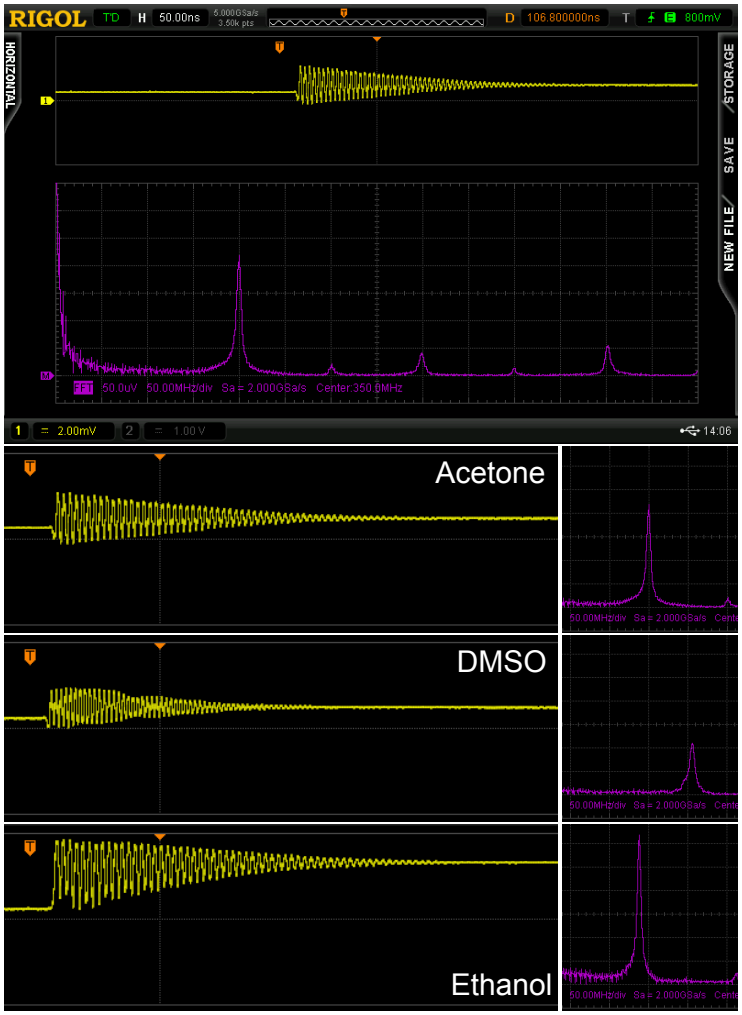

Figure 53 The experimental results for different simple liquids. When taking the data, the liquids were contained in quartz cuvettes. The data were acquired and analyzed in real time by an 8-bit oscilloscope (Rigol, Model: DS 6202, 600 MHz bandwidth).

Fig. 54 illustrates an example of the signal acquired from the flow cytometry arrangement (shown in Fig. 52a). During this measurement, we pumped an acetone solution through the microchannel, then collected and analyzed the temporal profile of

the diffracted probe laser. The signal was ~ 100 times weaker than from bulk samples. When taking the data, we averaged over 1024 measurements for each sample. Considering the repetition rate of the pulsed laser (20 kHz), the integration time for one measurement was about 50 ms. Due to the limited vertical resolution limit of the oscilloscope (8-bit), the quality of the signal was insufficient for accurate analysis. By taking advantage of commercially available high-speed, 12-16 bit resolution signal digitizers, better signal quality can be obtained in the future measurements. The signal envelop difference between the result shown in Fig. 54 and Fig. 53 may be induced by the interaction between the acoustic wave and the microchannel.

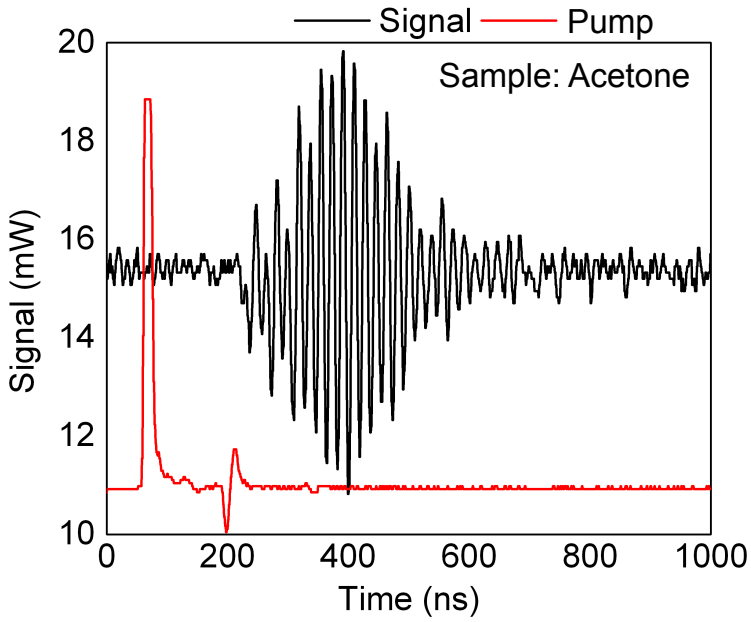

Figure 54 The temporal relationship of the pump and the output probe intensities.

Next, we extend the measurement to a variety of liquid types. The results are presented in Fig. 55. Fig. 55 (a) illustrates the temporal relationship between the pump and the output probe beams. The results of the FFT analysis of the output probe signals are displayed in Fig. 55 (b). Here we only plot the magnitude of the FFT results. Multiple peaks, including environmental noises, could be identified in the FFT spectra; however, we are interested in the sample-specific peaks only. For liquids with known sound speed,

we can calculate the wavelength of the stimulated phonons with the assistance of the ISBS frequency. For example, the ISBS frequency for methanol was 102.058 MHz. Considering the sound speed of methanol is 1100.50 m/s [259], the wavelength of the stimulated phonon is 21.57 μm. The similar stimulated acoustic wavelength can be found in other liquids. For example, by combining the ISBS frequency (139.288 MHz) and the sound speed (1482.00 m/s) for water, the acoustic wavelength was determined as 21.28 μm. According to these results, the lateral magnification factor of the 4*f* system can be determined as 0.90, and the equivalent focal length of the objective lens is f_2 = 13.49 mm. When testing unknown liquids, based on their ISBS frequency, we were able to calculate the sound speed (V) as well as the longitudinal modulus (ρV^2; ρ: mass density).

We further test some strategies for enhancing the signal strength. In this study, we upgraded the pump laser by replacing it with a picosecond 1064 nm laser (pulse duration: 10 ps, power: up to 300 mW). Two immediate benefits can be gained from this substitution. Firstly, by squeezing the pulse duration of the pump beam, the instantaneous pump intensity can be drastically increased. Therefore, the strength of the stimulated phonons was greatly enhanced. Secondly, compared with the visible laser source, the photothermal effect brought by the NIR sources is much lower. In this way, more laser power was allowed to exert onto the sample without inducing any damage. In Fig. 56, an example of the signal obtained from toluene is shown for illustration. This signal was taken following a single pump pulse. Similar with the previous experiments, the sample was contained in a microchannel. However, the signal strength was ~ 1,000 times stronger than for the nanosecond laser based system. Moreover, such measurements can be performed at an MHz-rate, making video-rate imaging and high-speed cytometry possible.

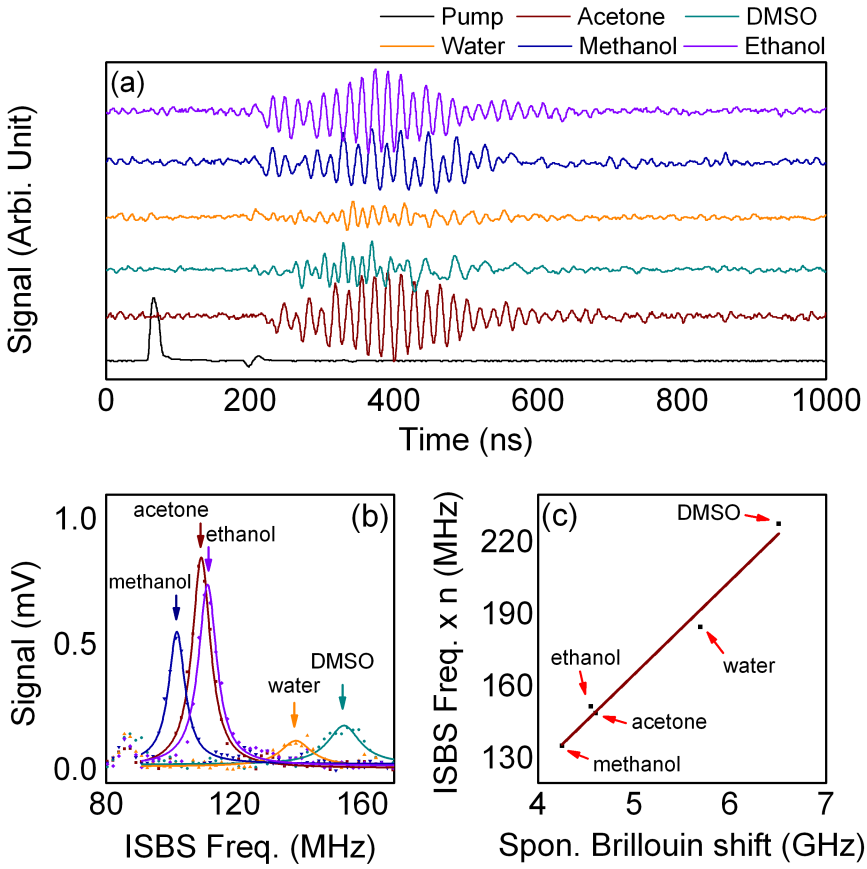

Figure 55 (a) The temporal relationship between the pump and the output probe intensities; (b) The results of the FFT analysis of the BISTRO signal; (c) Correlation between the spontaneous Brillouin shifts and the BISTRO frequency. The data for spontaneous Brillouin shift are taken from Boyd [1], and the excitation wavelength is 694 nm. The BISTRO frequencies are corrected for the corresponding refractive indices.

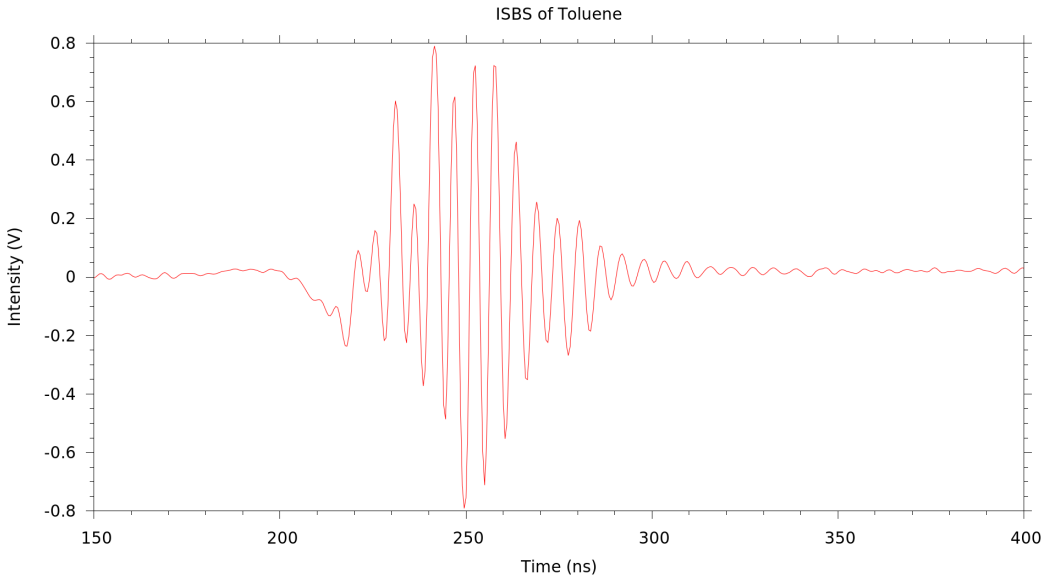

Figure 56 The time-dependent Brillouin signal obtained from toluene using 1064 nm 10-ps laser as the pump source.

Next, with the assistance of the 10-ps 1064 nm laser, we applied the BISTRO system for 2D imaging applications. Our test sample was made out of four distinct liquids (upper left: ethanol, lower left: methanol, upper right: water and lower right: DMSO). The liquids were separated by a glass (as shown in Fig. 52c). The scanning process was accomplished by a translational stage, as shown in Fig. 52 (b). Distinct Brillouin frequency shifts can be measured for different regions. The lateral spatial resolution of the BISTRO technique was limited ~ 20 μm, which was defined by the wavelength of the stimulated phonons. By slightly modifying the optical configuration and by using faster electronics for signal acquisition and digitization, a finer spatial resolution can be attained.

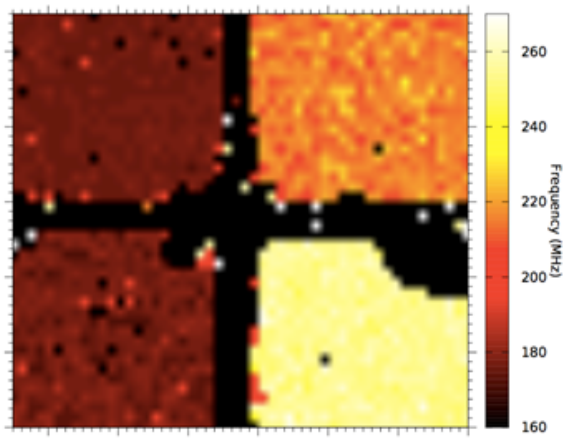

Figure 57 An example of the 2D image collected using the BISTRO system. The sample was from four different materials, which were characterized by distinct viscoelastic moduli.

7.4 Discussions and Summary

In this chapter, we demonstrated that the concept of Brillouin Imaging and Sensing via Time-Resolved Optical (BISTRO) measurements could be employed as a tool for assessing local viscoelasticity. The sample was excited using a nanosecond pulsed laser, and an acoustic transmission grating was created inside the sample via photostriction effect. In this way, a series of stimulated phonons would be formed and start to propagate immediately after its formation. By taking advantage of a cw probe laser, the propagation of the stimulated phonons could be monitored in the temporal domain. As a result, the sample's sound speed and associated mechanical properties can be retrieved from these measurements. The integration time for a single measurement takes about 50 ms, 20 times faster than spontaneous Brillouin acquisitions for the same signal-to-noise ratio (SNR).

Recent advances in atomic force microscopy (AFM) and optical tweezers have revealed the elasticity difference between healthy and diseased cells. For example, with the help

of AFM, Cross et al. proved that, in microscopic scale, cancerous cells taken from lung, breast, and pancreas cancer patients are considerably softer than their benign counterparts [94]. Using optical tweezers, the similar elasticity differences can also be monitored between healthy and diseased red blood cells (sickle cell disease) [208]. However, all current detections are based on individual cells. The efficiencies of these techniques fundamentally impede their clinical applicability. Therefore, with the limited amount of samples (e.g., circulating tumor cells [252], CTCs), the elasticity of the cells cannot be statistically studied. As a high throughput elasticity-specific probing technique, our current BISTRO flow cytometry setup is capable of distinguishing cells possessing with distinct mechanical properties and is expected to be applied in cell sorting and disease diagnosis.

The system can be further improved in, at least, two ways. Firstly, by lowering the wavelength of the simulated phonons, the spatial resolution can be improved. In our current system, the wavelength was longer than 20 μm, which set the lower limit of the system's spatial resolution. The theoretical expression of the acoustic wavelength can be written as: $\Lambda=(f_2/f_1)$d. Therefore, in order to obtain shorter wavelength, we may either decrease the focal length ratio between the two lenses (f_2/f_1), or elevate the line density of the transmission grating.

Secondly, the system's signal quality can be improved by upgrading the pump laser and the signal acquisition devices. In this particular study, the signal quality and SNR are both less than 10 for certain samples (e.g., water and DMSO). By taking advantage of picosecond pulsed lasers, we keep the same pump energy while enhance the strength of the stimulated acoustic wave. Moreover, a pump source with a longer wavelength (e.g., 800 – 1100 nm) can further elevate the damaging threshold of the sample. Once an NIR pump source is adopted, the SNR of the system could be further enhanced with higher pump power. Meanwhile, the currently used preamplifier may also contaminate the

signal quality. Signal digitizers with higher bit resolution could remove the necessity of the multi-stage preamplifiers, and, therefore, enhance the signal quality.

There is still much room to further optimize BISTRO system with respect to the signal quality and acquisition speed. Nevertheless, with the assistance of the picosecond pump source, we have demonstrated that the signal strength can be drastically enhanced, making MHz-rate detection possible.

In summary, we demonstrated that the nonlinear impulsive stimulated Brillouin spectroscopy could be applied as a tool for probing samples' viscoelasticity. This result enables investigators to probe the mechanical properties of the samples in a cell specific flow cytometry setup. We anticipate the wide use of this experimental arrangement in future investigations of cell mechanics.

CHAPTER VIII

CONCLUSIONS

Brillouin scattering has risen from theoretical inception to an important spectroscopic and imaging tool in many fields such as physics and biology. The study of the Brillouin scattering/spectroscopy has vastly progressed since 2005 from single point spectroscopy to a new imaging modality with a transverse resolution to be ~20 μm [133]. During the last decade, important steps forward have been achieved in this field. An important contribution was achieved by Scarcelli and Yun who first applied the novel imaging technique to the study of the elasticity properties of the eye lens and cornea [5]. A significant enhancement of the integration times of the Brillouin spectrum was obtained by the application of the VIPA etalon and the technological advances in high sensitivity CCD cameras. Moreover, Meng et al. and Antonacci et al. have developed separate strategies to eliminate the parasite elastic background accompanied with the Brillouin signal [105, 107], and further improved the signal quality of a typical VIPA-based Brillouin spectrometer. With the assistance of this improvement, investigators are enabled to probe the Brillouin shift from turbid and highly scattering samples, including biological samples.

Several biomedical applications have been designed and performed after the establishment of the background-free Brillouin spectrometer. We began from tissue-level applications. We have demonstrated that Brillouin spectroscopy is a novel approach to probing the viscoelasticity of the muscle tissues, and have demonstrated the distinct muscular elasticity under different dystrophy status. These discoveries warranted further pre-clinical or clinical applications on MD screening and diagnosis. We further extended the dual Brillouin/Raman microscopy into whole-body imaging applications. Specifically, we performed a whole-body imaging on zebrafish embryos during its

different developmental stages. The experimental result warrants the wide application of Brillouin spectroscopy in the field of developmental biology and biomechanics.

In order to overcome the difficulties brought by the weak signal of spontaneous Brillouin process, we have further introduced the coherent Brillouin spectroscopy. The BISTRO system has been designed and tested. Its capability in fluid cytometry and multidimensional imaging applications have been demonstrated.

The pioneering efforts of many groups over the years have drastically improved signal acquisition techniques and have overcome many of the problems that plagued Brillouin scattering spectroscopy that once made it of little concern to biologists. Indeed, some of the most impressive biological applications of Brillouin scattering have only been demonstrated in the last decade. We believe that Brillouin scattering applications will be greatly expanded and will one day be routinely used in biology and medicine.

REFERENCES

1. R. W. Boyd, *Nonlinear optics*, Academic press, 2003.

2. J. Ophir, S. K. Alam, B. S. Garra, F. Kallel, E. E. Konofagou, T. Krouskop, C. R. Merritt, R. Righetti, R. Souchon, and S. Srinivasan, "Elastography: imaging the elastic properties of soft tissues with ultrasound," Journal of Medical Ultrasonics **29**, 155-171 (2002).

3. E. M. Strohm, E. S. Berndl, and M. C. Kolios, "High frequency label-free photoacoustic microscopy of single cells," Photoacoustics **1**, 49-53 (2013).

4. T. Dehoux, M. A. Ghanem, O. Zouani, J.-M. Rampnoux, Y. Guillet, S. Dilhaire, M.-C. Durrieu, and B. Audoin, "All-optical broadband ultrasonography of single cells," Scientific reports **5** (2015).

5. G. Scarcelli, and S. H. Yun, "Confocal Brillouin microscopy for three-dimensional mechanical imaging," Nature Photonics **2**, 39-43 (2007).

6. C. L. Evans, and X. S. Xie, "Coherent anti-stokes Raman scattering microscopy: chemical imaging for biology and medicine," Annual review of analytical chemistry (Palo Alto, Calif.) **1**, 883-909 (2008).

7. C. W. Freudiger, W. Min, B. G. Saar, S. Lu, G. R. Holtom, C. W. He, J. C. Tsai, J. X. Kang, and X. S. Xie, "Label-Free Biomedical Imaging with High Sensitivity by Stimulated Raman Scattering Microscopy," Science **322**, 1857-1861 (2008).

8. S. Keren, C. Zavaleta, Z. Cheng, A. de la Zerda, O. Gheysens, and S. S. Gambhir, "Noninvasive molecular imaging of small living subjects using Raman spectroscopy," Proceedings of the National Academy of Sciences of the United States of America **105**, 5844-5849 (2008).

9. P. Nandakumar, A. Kovalev, and A. Volkmer, "Vibrational imaging based on stimulated Raman scattering microscopy," New Journal of Physics **11**, 033026 (2009).

10. S. Schlücker, "SERS Microscopy: Nanoparticle Probes and Biomedical Applications," ChemPhysChem **10**, 1344-1354 (2009).

11. Y. Ozeki, and K. Itoh, "Stimulated Raman scattering microscopy for live-cell imaging with high contrast and high sensitivity," Laser Physics **20**, 1114-1118 (2010).

12. B. G. Saar, C. W. Freudiger, J. Reichman, C. M. Stanley, G. R. Holtom, and X. S. Xie, "Video-Rate Molecular Imaging in Vivo with Stimulated Raman Scattering," Science **330**, 1368-1370 (2010).

13. M. N. Slipchenko, H. Chen, D. R. Ely, Y. Jung, M. T. Carvajal, and J.-X. Cheng, "Vibrational imaging of tablets by epi-detected stimulated Raman scattering microscopy," Analyst **135**, 2613-2619 (2010).

14. V. V. Yakovlev, G. I. Petrov, G. D. Noojin, C. Harbert, M. Denton, and R. Thomas, "Ex-CARS: exotic configuration for coherent anti-Stokes Raman scattering microspectroscopy utilizing two laser sources," Journal of Biophotonics **3**, 653-659 (2010).

15. V. V. Yakovlev, H. F. Zhang, G. D. Noojin, M. L. Denton, R. J. Thomas, and M. O. Scully, "Stimulated Raman photoacoustic imaging," Proc. Natl. Acad. Sci. U. S. A. **107**, 20335-20339 (2010).

16. G. Bergner, D. Akimov, S. Schlucker, H. Bartelt, B. Dietzek, and J. Popp, "Tunable optical setup with high flexibility for spectrally resolved coherent anti-Stokes Raman scattering microscopy," Laser Physics Letters **8**, 541-546 (2011).

17. I. Rajapaksa, and H. K. Wickramasinghe, "Raman spectroscopy and microscopy based on mechanical force detection," Appl. Phys. Lett. **99** (2011).

18. V. V. Yakovlev, G. I. Petrov, H. F. Zhang, G. D. Noojin, P. A. Thomas, M. L. Denton, B. A. Rockwell, and R. J. Thomas, "Chemically Specific Imaging Through Stimulated Raman Photoexcitation and Ultrasound Detection: Minireview," Australian Journal of Chemistry **65**, 260-265 (2012).

19. Z. Meng, "Microscopic coherent Raman imaging using low-cost continuous wave (cw) lasers," Laser Physics Letters **10**, 065701 (Accepted).

20. G. Mie, "Pioneering mathematical description of scattering by spheres," Ann. Phys **25**, 337 (1908).

21. L. Brillouin, "Diffusion de la lumière et des rayons X par un corps transparent homogène. Influence de l'agitation thermique," Ann. Phys.(Paris) **17**, 88-122 (1922).

22. C. V. Raman, and K. S. Krishnan, "The optical analogue of the Compton effect," Nature **121**, 711-711 (1928).

23. H. C. Van De Hulst, *Light scattering by small particles*, Courier Corporation, 1957.

24. M. I. Mishchenko, L. D. Travis, and D. W. Mackowski, "T-matrix computations of light scattering by nonspherical particles: a review," Journal of Quantitative Spectroscopy and Radiative Transfer **55**, 535-575 (1996).

25. P. Yang, Q. Feng, G. Hong, G. W. Kattawar, W. J. Wiscombe, M. I. Mishchenko, O. Dubovik, I. Laszlo, and I. N. Sokolik, "Modeling of the scattering and radiative properties of nonspherical dust-like aerosols," Journal of Aerosol Science **38**, 995-1014 (2007).

26. Z. Meng, P. Yang, G. W. Kattawar, L. Bi, K. Liou, and I. Laszlo, "Single-scattering properties of tri-axial ellipsoidal mineral dust aerosols: A database for application to radiative transfer calculations," Journal of Aerosol Science **41**, 501-512 (2010).

27. L.-M. Wong Kee Song, and N. E. Marcon, "Fluorescence and Raman spectroscopy," Gastrointestinal Endoscopy Clinics of North America **13**, 279-296 (2003).

28. F. Patolsky, G. F. Zheng, and C. M. Lieber, "Fabrication of silicon nanowire devices for ultrasensitive, label-free, real-time detection of biological and chemical species," Nature Protocols **1**, 1711-1724 (2006).

29. C. Heinrich, A. Hofer, A. Ritsch, C. Ciardi, S. Bernet, and M. Ritsch-Marte, "Selective imaging of saturated and unsaturated lipids by wide-field CARS-microscopy," Optics Express **16**, 2699-2708 (2008).

30. A. Owyoung, and E. D. Jones, "Stimulated Raman spectroscopy using low-power cw lasers," Optics Letters **1**, 152-154 (1977).

31. E. Ploetz, S. Laimgruber, S. Berner, W. Zinth, and P. Gilch, "Femtosecond stimulated Raman microscopy," Applied Physics B: Lasers and Optics **87**, 389-393 (2007).

32. Y. Ozeki, F. Dake, S. i. Kajiyama, K. Fukui, and K. Itoh, "Analysis and experimental assessment of the sensitivity of stimulated Raman scattering microscopy," Opt. Express **17**, 3651-3658 (2009).

33. A. Zumbusch, G. R. Holtom, and X. S. Xie, "Three-dimensional vibrational imaging by coherent anti-Stokes Raman scattering," Physical Review Letters **82**, 4142-4145 (1999).

34. M. v. Smoluchowski, "Molekular-kinetische Theorie der Opaleszenz von Gasen im kritischen Zustande, sowie einiger verwandter Erscheinungen," Annalen der Physik **330**, 205-226 (1908).

35. A. Einstein, "Theorie der Opaleszenz von homogenen Flüssigkeiten und Flüssigkeitsgemischen in der Nähe des kritischen Zustandes," Annalen der Physik **338**, 1275-1298 (1910).

36. L. I. Mandelstam, "Light Scattering by Inhomogeneous Media," Zh. Russ. Fiz-Khim. Ova. **58**, 381 (1926).

37. L. Brillouin, "Diffusion de la lumière et des rayons X par un corps transparent homogène. Influence de l'agitation thermique," Ann. Phys. (Paris) **17**, 88-122 (1922).

38. E. Gross, and A. Terenin, "Fine Structure of Optically Excited Spectrum Lines," Nature **116**, 280 (1925).

39. E. Gross, "Change of Wave-length of Light due to Elastic Heat Waves at Scattering in Liquids," Nature **126**, 201-202 (1930).

40. E. Gross, "Splitting of the Frequency of Light scattered by Liquids and Optical Anisotropy of Molecules," Nature **126**, 603-604 (1930).

41. E. Gross, "The Splitting of Spectral Lines at Scattering of Light by Liquids," nature **126**, 400 (1930).

42. E. Gross, "Modification of light quanta by elastic heat oscillations in scattering media," Nature **129**, 722-723 (1932).

43. L. Deng, X. Trepat, J. P. Butler, E. Millet, K. G. Morgan, D. A. Weitz, and J. J. Fredberg, "Fast and slow dynamics of the cytoskeleton," Nature materials **5**, 636-640 (2006).

44. A. Jaishankar, and G. H. McKinley, "Power-law rheology in the bulk and at the interface: quasi-properties and fractional constitutive equations," in *Proc. R. Soc. A*(The Royal Society, 2012), p. rspa20120284.

45. G. Scarcelli, P. Kim, and S. H. Yun, "In vivo measurement of age-related stiffening in the crystalline lens by Brillouin optical microscopy," Biophysical journal **101**, 1539-1545 (2011).

46. Y. R. Shen, and N. Bloembergen, "Theory of stimulated Brillouin and Raman scattering," Physical Review **137**, A1787 (1965).

47. P. Maker, and R. Terhune, "Study of optical effects due to an induced polarization third order in the electric field strength," Physical Review **137**, A801 (1965).

48. R. Begley, A. Harvey, and R. L. Byer, "Coherent anti‐Stokes Raman spectroscopy," Appl. Phys. Lett. **25**, 387-390 (1974).

49. G. Eckhardt, R. Hellwarth, F. McClung, S. Schwarz, D. Weiner, and E. Woodbury, "Stimulated Raman scattering from organic liquids," Physical Review Letters **9**, 455 (1962).

50. R. Hellwarth, "Analysis of stimulated Raman scattering of a giant laser pulse," Applied Optics **2**, 847-853 (1963).

51. S. De Silvestri, J. Fujimoto, E. Ippen, E. B. Gamble, L. R. Williams, and K. A. Nelson, "Femtosecond time-resolved measurements of optic phonon dephasing by impulsive stimulated raman scattering in α-perylene crystal from 20 to 300 K," Chemical physics letters **116**, 146-152 (1985).

52. S. Ruhman, A. G. Joly, and K. A. Nelson, "Coherent molecular vibrational motion observed in the time domain through impulsive stimulated Raman scattering," Quantum Electronics, IEEE Journal of **24**, 460-469 (1988).

53. A. M. Weiner, G. P. Wiederrecht, K. A. Nelson, and D. Leaird, "Femtosecond multiple-pulse impulsive stimulated Raman scattering spectroscopy," JOSA B **8**, 1264-1275 (1991).

54. M. Levenson, and J. Song, "Raman-induced Kerr effect with elliptical polarization," JOSA **66**, 641-643 (1976).

55. J. Bergmann, K. Kneipp, and H. Ponath, "Raman‐induced Kerr effect with elliptical polarization in optically active and anisotropic crystals," physica status solidi (b) **86**, 215-223 (1978).

56. D. Heiman, R. Hellwarth, M. Levenson, and G. Martin, "Raman-induced Kerr effect," Physical Review Letters **36**, 189 (1976).

57. Y. Dong, L. Chen, and X. Bao, "Characterization of the Brillouin grating spectra in a polarization-maintaining fiber," Optics express **18**, 18960-18967 (2010).

58. R. Y. Chiao, C. H. Townes, and B. P. Stoicheff, "Stimulated Brillouin scattering and coherent generation of intense hypersonic waves," Physical Review Letters **12**, 592 (1964).

59. H. Boersch, and H. Eichler, "Beugung an einem mit stehenden Lichtwellen gepumpten Rubin," ZEITSCHRIFT FUR ANGEWANDTE PHYSIK **22**, 378-& (1967).

60. H. Eichler, "Laser-induced grating phenomena," Journal of Modern Optics **24**, 631-642 (1977).

61. T. Haga, M. Higuchi, K. Abe, and T. Shigenari, "Optical heterodyned coherent Brillouin spectroscopy (OHD-BIKES) using continuous-wave (cw) dye lasers," Japanese Journal of Applied Physics **28**, 1199 (1989).

62. A. Jacobson, and Y. Shen, "Coherent Brillouin spectroscopy," Appl. Phys. Lett. **34**, 464-467 (1979).

63. K. A. Nelson, and M. D. Fayer, "Laser induced phonons: A probe of intermolecular interactions in molecular solids," The Journal of Chemical Physics **72**, 5202-5218 (1980).

64. S. Kinoshita, Y. Shimada, W. Tsurumaki, M. Yamaguchi, and T. Yagi, "New high‐resolution phonon spectroscopy using impulsive stimulated Brillouin scattering," Review of Scientific Instruments **64**, 3384-3393 (1993).

65. J. M. Brown, L. J. Slutsky, K. A. Nelson, and L. T. Cheng, "Velocity of sound and equations of state for methanol and ethanol in a diamond-anvil cell," Science **241**, 65-67 (1988).

66. L.-T. Cheng, and K. A. Nelson, "Ferroelectric phase transition in RbH 2 PO 4: Picosecond time-resolved impulsive stimulated Brillouin scattering experiments," Physical Review B **37**, 3603 (1988).

67. A. R. Duggal, J. A. Rogers, and K. A. Nelson, "Real‐time optical characterization of surface acoustic modes of polyimide thin‐film coatings," Journal of applied physics **72**, 2823-2839 (1992).

68. J. A. Johnson, K. J. Manke, D. G. Veyssett, A. A. Maznev, K. J. Ramos, D. E. Hooks, and K. A. Nelson, "Photoacoustic determination of the speed of sound in single crystal cyclotrimethylene trinitramine at acoustic frequencies from 0.5 to 15 GHz," Journal of Applied Physics **110** (2011).

69. P. T. Macklem, "Viewpoint: emergent phenomena and the secrets of life," Journal of Applied Physiology (2008).

70. B. Geiger, J. P. Spatz, and A. D. Bershadsky, "Environmental sensing through focal adhesions," Nature reviews Molecular cell biology **10**, 21-33 (2009).

71. A. Bershadsky, M. Kozlov, and B. Geiger, "Adhesion-mediated mechanosensitivity: a time to experiment, and a time to theorize," Curr Opin Cell Biol **18**, 472-481 (2006).

72. A. D. Bershadsky, N. Q. Balaban, and B. Geiger, "Adhesion-dependent cell mechanosensitivity," Annu Rev Cell Dev Biol **19**, 677-695 (2003).

73. S. Liang, M. J. Slattery, and C. Dong, "Shear stress and shear rate differentially affect the multi-step process of leukocyte-facilitated melanoma adhesion," Experimental cell research **310**, 282-292 (2005).

74. M. J. Slattery, S. Liang, and C. Dong, "Distinct role of hydrodynamic shear in leukocyte-facilitated tumor cell extravasation," American Journal of Physiology-Cell Physiology **288**, C831-C839 (2005).

75. D. Ingber, "Mechanobiology and diseases of mechanotransduction," Annals of medicine **35**, 564-577 (2003).

76. D. E. Ingber, "Mechanical control of tissue morphogenesis during embryological development," International Journal of Developmental Biology **50**, 255 (2006).

77. M. Fatemi, and J. F. Greenleaf, "Ultrasound-stimulated vibro-acoustic spectrography," Science **280**, 82-85 (1998).

78. J. Ophir, I. Cespedes, H. Ponnekanti, Y. Yazdi, and X. Li, "Elastography: a quantitative method for imaging the elasticity of biological tissues," Ultrasonic imaging **13**, 111-134 (1991).

79. R. Muthupillai, D. Lomas, P. Rossman, J. Greenleaf, A. Manduca, and R. Ehman, "Magnetic resonance elastography by direct visualization of propagating acoustic strain waves," Science **269**, 1854-1857 (1995).

80. A. Manduca, T. E. Oliphant, M. Dresner, J. Mahowald, S. Kruse, E. Amromin, J. P. Felmlee, J. F. Greenleaf, and R. L. Ehman, "Magnetic resonance elastography: non-invasive mapping of tissue elasticity," Medical image analysis **5**, 237-254 (2001).

81. C. U. Devi, R. M. Vasu, and A. Sood, "Design, fabrication, and characterization of a tissue-equivalent phantom for optical elastography," Journal of biomedical optics **10**, 044020-044020-044010 (2005).

82. K. Daoudi, A.-C. Boccara, and E. Bossy, "Detection and discrimination of optical absorption and shear stiffness at depth in tissue-mimicking phantoms by transient optoelastography," Appl. Phys. Lett. **94**, 154103 (2009).

83. C. H. Liu, M. N. Skryabina, J. Li, M. Singh, E. N. Sobol, and K. V. Larin, "Measurement of the temperature dependence of Young's modulus of cartilage by phase-sensitive optical coherence elastography," Quantum Electronics **44**, 751 (2014).

84. S. Wang, and K. V. Larin, "Optical coherence elastography for tissue characterization: a review," Journal of biophotonics **8**, 279-302 (2015).

85. J. Schmitt, "OCT elastography: imaging microscopic deformation and strain of tissue," Optics Express **3**, 199-211 (1998).

86. C. Sun, B. Standish, and V. X. D. Yang, "Optical coherence elastography: current status and future applications," Journal of Biomedical Optics **16**, 043001-043001-043012 (2011).

87. C. H. Li, G. Y. Guan, X. Cheng, Z. H. Huang, and R. K. K. Wang, "Quantitative elastography provided by surface acoustic waves measured by phase-sensitive optical coherence tomography," Optics Letters **37**, 722-724 (2012).

88. M. Radmacher, "Measuring the elastic properties of biological samples with the AFM," Engineering in Medicine and Biology Magazine, IEEE **16**, 47-57 (1997).

89. N. Sasaki, and S. Odajima, "Stress-strain curve and Young's modulus of a collagen molecule as determined by the X-ray diffraction technique," Journal of biomechanics **29**, 655-658 (1996).

90. D. H. Kruger, P. Schneck, and H. R. Gelderblom, "Helmut Ruska and the visualisation of viruses," The Lancet **355**, 1713-1717 (2000).

91. M. P. E. Wenger, L. Bozec, M. A. Horton, and P. Mesquida, "Mechanical properties of collagen fibrils," Biophysical journal **93**, 1255-1263 (2007).

92. D. T. Butcher, T. Alliston, and V. M. Weaver, "A tense situation: forcing tumour progression," Nature Reviews Cancer **9**, 108-122 (2009).

93. G. Scarcelli, S. Kling, E. Quijano, R. Pineda, S. Marcos, and S. H. Yun, "Brillouin microscopy of collagen crosslinking: noncontact depth-dependent analysis of corneal elastic modulus," Investigative ophthalmology & visual science **54**, 1418-1425 (2013).

94. S. E. Cross, Y.-S. Jin, J. Rao, and J. K. Gimzewski, "Nanomechanical analysis of cells from cancer patients," Nature Nanotechnology **2**, 780-783 (2007).

95. S. Suresh, "Biomechanics and biophysics of cancer cells," Acta Materialia **55**, 3989-4014 (2007).

96. J. Guck, S. Schinkinger, B. Lincoln, F. Wottawah, S. Ebert, M. Romeyke, D. Lenz, H. M. Erickson, R. Ananthakrishnan, and D. Mitchell, "Optical Deformability as an Inherent Cell Marker for Testing Malignant Transformation and Metastatic Competence," Biophysical Journal **88**, 3689-3698 (2005).

97. T. A. Krouskop, T. M. Wheeler, F. Kallel, B. S. Garra, and T. Hall, "Elastic moduli of breast and prostate tissues under compression," Ultrasonic imaging **20**, 260-274 (1998).

98. P. Wellman, R. D. Howe, E. Dalton, and K. A. Kern, "Breast tissue stiffness in compression is correlated to histological diagnosis," Harvard BioRobotics Laboratory Technical Report (1999).

99. P. Benassi, R. Eramo, A. Giugni, M. Nardone, and M. Sampoli, "A spectrometer for high-resolution and high-contrast Brillouin spectroscopy in the ultraviolet," Review of Scientific Instruments **76**, 013904-013904-013907 (2005).

100. T. Matsuoka, K. Sakai, and K. Takagi, "Hyper‐resolution Brillouin–Rayleigh spectroscopy with an optical beating technique," Review of Scientific Instruments **64**, 2136-2139 (1993).

101. J. Sandercock, "Simple stabilization scheme for maintenance of mirror alignment in a scanning February-Perot interferometer," Journal of Physics E: Scientific Instruments **9**, 566 (1976).

102. G. Scarcelli, and S. H. Yun, "Multistage VIPA etalons for high-extinction parallel Brillouin spectroscopy," Optics express **19**, 10913-10922 (2011).

103. K. V. Berghaus, S. H. Yun, and G. Scarcelli, "High Speed Sub-GHz Spectrometer for Brillouin Scattering Analysis," Journal of Visualized Experiments, e53468-e53468 (2015).

104. K. Berghaus, J. Zhang, S. H. Yun, and G. Scarcelli, "High-finesse sub-GHz-resolution spectrometer employing VIPA etalons of different dispersion," Optics Letters **40**, 4436-4439 (2015).

105. Z. Meng, A. J. Traverso, and V. V. Yakovlev, "Background clean-up in Brillouin microspectroscopy of scattering medium," Opt Express **22**, 5410-5415 (2014).

106. Z. Meng, and V. V. Yakovlev, "Optimizing signal collection efficiency of the VIPA-based Brillouin spectrometer," Journal of Innovative Optical Health Sciences **8**, 1550021 (2014).

107. G. Antonacci, G. Lepert, C. Paterson, and P. Török, "Elastic suppression in Brillouin imaging by destructive interference," Appl. Phys. Lett. **107**, 061102 (2015).

108. G. Scarcelli, R. Pineda, and S. H. Yun, "Brillouin Optical Microscopy for Corneal Biomechanics," Investigative Ophthalmology & Visual Science **53**, 185-190 (2012).

109. Z. Steelman, Z. Meng, A. J. Traverso, and V. V. Yakovlev, "Brillouin spectroscopy as a new method of screening for increased CSF total protein during bacterial meningitis," Journal of Biophotonics **8**, 408-414 (2015).

110. G. Antonacci, R. M. Pedrigi, A. Kondiboyina, V. V. Mehta, R. de Silva, C. Paterson, R. Krams, and P. Török, "Quantification of plaque stiffness by Brillouin microscopy in experimental thin cap fibroatheroma," Journal of the Royal Society Interface **12**, 20150843 (2015).

111. Z. Meng, S. C. Bustamante-Lopez, K. E. Meissner, and V. V. Yakovlev, "Subcellular measurements of mechanical and chemical properties using dual Raman-Brillouin microspectroscopy," Journal of Biophotonics **9**, 201-207 (2016).

112. A. J. Traverso, J. V. Thompson, Z. A. Steelman, Z. Meng, M. O. Scully, and V. V. Yakovlev, "Dual Raman-Brillouin Microscope for Chemical and Mechanical Characterization and Imaging," Analytical Chemistry **87**, 7519-7523 (2015).

113. Z. Meng, and V. V. Yakovlev, "Precise determination of Brillouin scattering spectrum using VIPA spectrometer and CCD camera," Applied Spectroscopy **Accepted** (2015).

114. Z. Meng, G. I. Petrov, and V. V. Yakovlev, "Microscopic coherent Raman imaging using low-cost continuous wave lasers," Laser Physics Letters **10**, 065701 (2013).

115. Z. Meng, G. I. Petrov, and V. V. Yakovlev, "Continuous-wave stimulated Raman scattering (cwSRS) microscopy," Applied Physics B **112**, 99-103 (2013).

116. G. I. Petrov, Z. Meng, and V. V. Yakovlev, "Electronically tunable coherent Raman spectroscopy using acousto-optics tunable filter," Optics Express **23**, 24669-24674 (2015).

117. Z. Meng, G. I. Petrov, and V. V. Yakovlev, "Pure electrical, highly-efficient and sidelobe free coherent Raman spectroscopy using acousto-optics tunable filter (AOTF)," Scientific Reports **6** (2016).

118. Z. Meng, G. I. Petrov, S. Cheng, J. A. Jo, K. K. Lehmann, V. V. Yakovlev, and M. O. Scully, "Lightweight Raman spectroscope using time-correlated photon-counting detection," Proceedings of the National Academy of Sciences **112**, 12315-12320 (2015).

119. I. L. Fabelinskii, *Molecular scattering of light* (Springer Science & Business Media, 2012).

120. D. S. Bedborough, and D. Jackson, "Brillouin scattering study of gelatin gel using a double passed Fabry-Perot spectrometer," Polymer **17**, 573-576 (1976).

121. R. Harley, D. James, A. Miller, and J. W. White, "Phonons and elastic moduli of collagen and muscle," Nature **267**, 285-287 (1977).

122. S. Cusack, and A. Miller, "Determination of the elastic constants of collagen by Brillouin light scattering," Journal of molecular biology **135**, 39-51 (1979).

123. J. Randall, and J. M. Vaughan, "Brillouin scattering in systems of biological significance," Philosophical Transactions of the Royal Society a-Mathematical Physical and Engineering Sciences **293**, 341-348 (1979).

124. J. M. Vaughan, and J. T. Randall, "Brillouin scattering, density and elastic properties of the lens and cornea of the eye," Nature **284**, 489-491 (1980).

125. C. Hellmich, "Microelasticity of bone," Cism Cour L, 289-331 (2005).

126. J.-P. LePesant, L. Powers, and P. S. Pershan, "Brillouin light scattering measurement of the elastic properties of aligned multilamella lipid samples," Proceedings of the National Academy of Sciences **75**, 1792-1795 (1978).

127. G. Maret, R. Oldenbourg, G. Winterling, K. Dransfeld, and A. Rupprecht, "Velocity of high frequency sound waves in oriented DNA fibres and films determined by Brillouin scattering," Colloid and Polymer Science **257**, 1017-1020 (1979).

128. M. B. Hakim, S. Lindsay, and J. Powell, "The speed of sound in DNA," Biopolymers **23**, 1185-1192 (1984).

129. W. Doster, B. Simon, G. Schmidt, and W. Mayr, "Compressibility of lysozyme in solution from time‐resolved Brillouin difference spectroscopy," Biopolymers **24**, 1543-1548 (1985).

130. N. Berovic, N. Thomas, R. Thornhill, and J. Vaughan, "Observation of Brillouin scattering from single muscle fibres," European Biophysics Journal **17**, 69-74 (1989).

131. L. Genberg, Q. Bao, S. Gracewski, and R. Miller, "Picosecond transient thermal phase grating spectroscopy: a new approach to the study of vibrational energy relaxation processes in proteins," Chemical physics **131**, 81-97 (1989).

132. L. Richard, L. Genberg, J. Deak, H. L. Chiu, and R. D. Miller, "Picosecond phase grating spectroscopy of hemoglobin and myoglobin: energetics and dynamics of global protein motion," Biochemistry **31**, 10703-10715 (1992).

133. K. J. Koski, and J. L. Yarger, "Brillouin imaging," Appl. Phys. Lett. **87** (2005).

134. M. Shirasaki, "Large angular dispersion by a virtually imaged phased array and its application to a wavelength demultiplexer," Optics Letters **21**, 366-368 (1996).

135. M. Shirasaki, "Virtually imaged phased array," Fujitsu Scientific & Technical Journal **35**, 113-125 (1999).

136. B. Audoin, C. Rossignol, N. Chigarev, M. Ducousso, G. Forget, F. Guillemot, and M.-C. Durrieu, "Picosecond acoustics in vegetal cells: Non-invasive in vitro measurements at a sub-cell scale," Ultrasonics **50**, 202-207 (2010).

137. C. Rossignol, N. Chigarev, M. Ducousso, B. Audoin, G. Forget, F. Guillemot, and M. Durrieu, "In Vitro picosecond ultrasonics in a single cell," Appl. Phys. Lett. **93**, 3901 (2008).

138. A. Maznev, K. J. Manke, C. Klieber, K. A. Nelson, S. Baek, and C.-B. Eom, "Coherent Brillouin spectroscopy in a strongly scattering liquid by picosecond ultrasonics," Optics letters **36**, 2925-2927 (2011).

139. B. Stephanidis, S. Adichtchev, P. Gouet, A. McPherson, and A. Mermet, "Elastic properties of viruses," Biophysical Journal **93**, 1354-1359 (2007).

140. R. Hartschuh, S. Wargacki, H. Xiong, J. Neiswinger, A. Kisliuk, S. Sihn, V. Ward, R. Vaia, and A. Sokolov, "How rigid are viruses," Physical Review E **78**, 021907 (2008).

141. T. A. Kelf, W. Hoshii, P. H. Otsuka, H. Sakuma, I. A. Veres, R. M. Cole, S. Mahajan, J. J. Baumberg, M. Tomoda, and O. Matsuda, "Mapping gigahertz vibrations in a plasmonic–phononic crystal," New Journal of Physics **15**, 023013 (2013).

142. Z. Meng, V. V. Yakovlev, and Z. Utegulov, "Surface-enhanced Brillouin scattering in a vicinity of plasmonic gold nanostructures," in *SPIE BiOS*(International Society for Optics and Photonics, 2015), pp. 93400Z-93400Z-93408.

143. W. Johnson, S. Kim, Z. Utegulov, J. Shaw, and B. Draine, "Optimization of arrays of gold nanodisks for plasmon-mediated Brillouin light scattering," The Journal of Physical Chemistry C **113**, 14651-14657 (2009).

144. M. Fukui, O. Tada, V. So, and G. Stegeman, "Enhanced Brillouin scattering involving surface plasmon polaritons," Journal of Physics C: Solid State Physics **14**, 5591 (1981).

145. H. El Bashir, M. Laundy, and R. Booy, "Diagnosis and treatment of bacterial meningitis," Archives of disease in childhood **88**, 615-620 (2003).

146. A. R. Tunkel, and W. M. Scheld, "Treatment of bacterial meningitis," Current infectious disease reports **4**, 7-16 (2002).

147. K. Stuertz, I. Merx, H. Eiffert, E. Schmutzhard, M. Mäder, and R. Nau, "Enzyme immunoassay detecting teichoic and lipoteichoic acids versus cerebrospinal fluid culture and latex agglutination for diagnosis of Streptococcus pneumoniae meningitis," Journal of clinical microbiology **36**, 2346-2348 (1998).

148. B. Karlsson, and C. Alling, "A comparative study of three approaches to the routine quantitative determination of spinal fluid total proteins," Clinica Chimica Acta **105**, 65-73 (1980).

149. M. C. Brouwer, G. E. Thwaites, A. R. Tunkel, and D. van de Beek, "Dilemmas in the diagnosis of acute community-acquired bacterial meningitis," The Lancet **380**, 1684-1692 (2012).

150. S. H. Wang, L. P. Lee, and J. S. Lee, "A linear relation between the compressibility and density of blood," The Journal of the Acoustical Society of America **109**, 390-396 (2001).

151. Z. Meng, and V. V. Yakovlev, "Probing microscopic mechanical properties of hard tissues with Brillouin spectroscopy," in *SPIE BiOS*(International Society for Optics and Photonics, 2015), pp. 930342-930342-930347.

152. Z. Meng, and V. V. Yakovlev, "Brillouin spectroscopy characterizes microscopic viscoelasticity associated with skin injury," in *SPIE BiOS*(International Society for Optics and Photonics, 2015), pp. 93210C-93210C-93216.

153. Z. Meng, B. Basagaoglu, and V. V. Yakovlev, "Atherosclerotic plaque detection by confocal Brillouin and Raman microscopies," in *SPIE BiOS*(International Society for Optics and Photonics, 2015), pp. 93033N-93033N-93037.

154. Z. Meng, C. Chitrakar, A. K. Gaharwar, and V. V. Yakovlev, "Reinforcement of osteogenesis with nanofabricated hydroxyapatite and GelMA nanocomposite," in *SPIE BiOS*(International Society for Optics and Photonics, 2015), pp. 930340-930340-930347.

155. R. Vacher, and L. Boyer, "Brillouin scattering: a tool for the measurement of elastic and photoelastic constants," Physical Review B **6**, 639 (1972).

156. V. Mazzacurati, and G. Ruocco, "The super-gratings: How to improve the limiting resolution of grating spectrometers," Optics Communications **76**, 185-190 (1990).

157. H. Tanaka, and T. Sonehara, "New method of superheterodyne light beating spectroscopy for Brillouin scattering using frequency-tunable lasers," Physical Review Letters **74**, 1609 (1995).

158. G. Simonsohn, and F. Wagner, "High-resolution Rayleigh–Brillouin correlation spectroscopy," Optics letters **14**, 110-112 (1989).

159. S. Lindsay, M. Anderson, and J. Sandercock, "Construction and alignment of a high performance multipass vernier tandem Fabry–Perot interferometer," Review of Scientific Instruments **52**, 1478-1486 (1981).

160. P. Jacquinot, "The luminosity of spectrometers with prisms, gratings, or Fabry-Perot etalons," JOSA **44**, 761-765 (1954).

161. J. R. Sandercock, "Trends in Brillouin scattering - studies of opaque materials, supported films, and central modes," Topics in Applied Physics **51**, 173-206 (1982).

162. D. Walton, J. Vanderwal, H. Xia, and P. Zhao, "The use of area detectors in Brillouin spectroscopy," Review of scientific instruments **67**, 2727-2731 (1996).

163. K. Liang, Y. Ma, J. Huang, H. Li, and Y. Yu, "Precise measurement of Brillouin scattering spectrum in the ocean using F–P etalon and ICCD," Applied Physics B **105**, 421-425 (2011).

164. K. Koski, J. Müller, H. Hochheimer, and J. Yarger, "High pressure angle-dispersive Brillouin spectroscopy: A technique for determining acoustic velocities and attenuations in liquids and solids," Review of scientific instruments **73**, 1235-1241 (2002).

165. S.-i. Itoh, "Very rapid nonscanning Brillouin spectroscopy using fixed etalons and multichannel detectors," Japanese Journal of Applied Physics **37**, 3134 (1998).

166. J.-H. Ko, and S. Kojima, "Nonscanning Brillouin spectroscopy applied to solid materials," Review of scientific instruments **73**, 4390-4392 (2002).

167. S. Xiao, A. M. Weiner, and C. Lin, "A dispersion law for virtually imaged phased-array spectral dispersers based on paraxial wave theory," Quantum Electronics, IEEE Journal of **40**, 420-426 (2004).

168. S. Xiao, and A. M. Weiner, "An eight-channel hyperfine wavelength demultiplexer using a virtually imaged phased-array(VIPA)," IEEE photonics technology letters **17**, 372-374 (2005).

169. G. Scarcelli, and S. H. Yun, "Confocal Brillouin microscopy for three-dimensional mechanical imaging," Nat Photon **2**, 39-43 (2008).

170. P. Piironen, and E. Eloranta, "Demonstration of a high-spectral-resolution lidar based on an iodine absorption filter," Optics Letters **19**, 234-236 (1994).

171. J. Simmons, and J. Hougen, "Atlas of the l2 Spectrum from 19 000 to 18 000 cm-i," Journal of Research of the National Bureau of Standards - A, Physics and Chemistry **81A**, 80 (1977).

172. G. E. Devlin, J. L. Davis, L. Chase, and S. Geschwind, "Absorption of Unshifted Scattered Light by a Molecular I< inf> 2</inf> Filter in Brillouin and Raman Scattering," Appl. Phys. Lett. **19**, 138-141 (1971).

173. P. Schoen, and D. Jackson, "The iodine filter in Raman and Brillouin spectroscopy," Journal of Physics E: Scientific Instruments **5**, 519 (1972).

174. K. F. Wall, and R. K. Chang, "Separation of the low-frequency mode from the inelastic continuum scattering of a SERS active electrode," Chemical physics letters **129**, 144-148 (1986).

175. P. J. Horoyski, and M. L. W. Thewalt, "Fourier transform Raman and Brillouin Spectroscopy using atomic vapor filters," Applied spectroscopy **48**, 843-847 (1994).

176. A. E. Siegman, *Lasers* (University Science Books, 1986).

177. V. Syal, S. Chauhan, and R. Gautam, "Ultrasonic velocity measurements of carbohydrates in binary mixtures of DMSO + H2O at 25° C," Ultrasonics **36**, 619-623 (1998).

178. P. Fratzl, H. Gupta, E. Paschalis, and P. Roschger, "Structure and mechanical quality of the collagen–mineral nano-composite in bone," Journal of Materials Chemistry **14**, 2115-2123 (2004).

179. A. P. Yalin, "Gas phase and plasma diagnostics based on resonant atomic vapor filters," in *Mechanical and Aerospace Engineering*(Princeton University, Princeton, NJ, 2000).

180. A. Vega, A. M. Weiner, and C. Lin, "Generalized grating equation for virtually-imaged phased-array spectral dispersers," Applied optics **42**, 4152-4155 (2003).

181. S. Xiao, A. M. Weiner, and C. Lin, "Experimental and theoretical study of hyperfine WDM demultiplexer performance using the virtually imaged phased-array (VIPA)," Lightwave Technology, Journal of **23**, 1456-1467 (2005).

182. J. Xu, X. Ren, W. Gong, R. Dai, and D. Liu, "Measurement of the bulk viscosity of liquid by Brillouin scattering," Applied optics **42**, 6704-6709 (2003).

183. J. Huang, Y. Ma, B. Zhou, H. Li, Y. Yu, and K. Liang, "Processing method of spectral measurement using FP etalon and ICCD," Optics Express **20**, 18568-18578 (2012).

184. G. Scarcelli, and S. H. Yun, "In vivo Brillouin optical microscopy of the human eye," Optics Express **20**, 9197-9202 (2012).

185. E. S. Fry, Y. Emery, X. Quan, and J. W. Katz, "Accuracy limitations on Brillouin lidar measurements of temperature and sound speed in the ocean," Appl Opt **36**, 6887-6894 (1997).

186. G. Antonacci, M. R. Foreman, C. Paterson, and P. Török, "Spectral broadening in Brillouin imaging," Appl. Phys. Lett. **103**, 221105 (2013).

187. J. Simmons, and J. Hougen, "Atlas of the l2 Spectrum from 19 000 to 18 000 cm-i," Journal of Research of the National Bureau of Standards **81**, 1-56 (1977).

188. S. Gerstenkorn, and P. Luc, "Atlas du spectre d'absorption de la molecule d'iode 14800-20000 cm-1," Paris: Editions du Centre National de la Recherche Scientifique (CNRS), 1978 **1** (1978).

189. W. Gao, Z. Lv, Y. Dong, and W. He, "A new approach to measure the ocean temperature using Brillouin lidar," Chinese Optics Letters **4**, 428-431 (2006).

190. Z. Steelman, Z. Meng, A. J. Traverso, and V. V. Yakovlev, "Brillouin spectroscopy as a new method of screening for increased CSF total protein during bacterial meningitis," Journal of Biophotonics **9999** (2014).

191. J. Wang, Y. Zhang, T. H. Xu, Q. M. Luo, and D. Zhu, "An innovative transparent cranial window based on skull optical clearing," Laser Physics Letters **9**, 469 (2012).

192. H. G. Danielmeyer, "Aperture Corrections for Sound‐Absorption Measurements with Light Scattering," The Journal of the Acoustical Society of America **47**, 151-154 (1970).

193. M. H. Manghnani, S. N. Tkachev, P. V. Zinin, C. Glorieoux, P. Karvankova, and S. Veprek, "Elastic properties of nc-TiN/a-Si3N4 and nc-TiN/a-BN nanocomposite films by surface Brillouin scattering," J. Appl. Phys. **97**, 054308-054301-054304 (2005).

194. S. Reiß, G. Burau, O. Stachs, R. Guthoff, and H. Stolz, "Spatially resolved Brillouin spectroscopy to determine the rheological properties of the eye lens," Biomedical optics express **2**, 2144 (2011).

195. C. Raman, and K. Krishnan, "The optical analogue of the Compton effect," Nature **121**, 711 (1928).

196. C. L. Evans, and X. S. Xie, "Coherent anti-stokes Raman scattering microscopy: chemical imaging for biology and medicine," Annual Review of Analytical Chemistry **1**, 883-909 (2008).

197. B. G. Saar, G. R. Holtom, C. W. Freudiger, C. Ackermann, W. Hill, and X. S. Xie, "Intracavity wavelength modulation of an optical parametric oscillator for coherent Raman microscopy," Optics express **17**, 12532-12539 (2009).

198. V. V. Yakovlev, H. F. Zhang, G. D. Noojin, M. L. Denton, R. J. Thomas, and M. O. Scully, "Stimulated Raman photoacoustic imaging," Proceedings of the National Academy of Sciences **107**, 20335-20339 (2010).

199. C. W. Freudiger, W. Min, G. R. Holtom, B. Xu, M. Dantus, and X. S. Xie, "Highly specific label-free molecular imaging with spectrally tailored excitation-stimulated Raman scattering (STE-SRS) microscopy," Nature photonics **5**, 103-109 (2011).

200. R. Arora, G. I. Petrov, V. V. Yakovlev, and M. O. Scully, "Detecting anthrax in the mail by coherent Raman microspectroscopy," Proceedings of the National Academy of Sciences **109**, 1151-1153 (2012).

201. B. H. Hokr, J. N. Bixler, G. D. Noojin, R. J. Thomas, B. A. Rockwell, V. V. Yakovlev, and M. O. Scully, "Single-shot stand-off chemical identification of powders using random Raman lasing," Proceedings of the National Academy of Sciences **111**, 12320-12324 (2014).

202. J.-L. H. Demers, F. W. L. Esmonde-White, K. A. Esmonde-White, M. D. Morris, and B. W. Pogue, "Next-generation Raman tomography instrument for non-invasive in vivo bone imaging," Biomedical Optics Express **6**, 793-806 (2015).

203. J.-L. H. Demers, S. C. Davis, B. W. Pogue, and M. D. Morris, "Multichannel diffuse optical Raman tomography for bone characterization in vivo: a phantom study," Biomedical Optics Express **3**, 2299-2305 (2012).

204. F. Palombo, M. Madami, N. Stone, and D. Fioretto, "Mechanical mapping with chemical specificity by confocal Brillouin and Raman microscopy," Analyst **139**, 729-733 (2014).

205. C. Pasternak, S. Wong, and E. L. Elson, "Mechanical function of dystrophin in muscle cells," The Journal of Cell Biology **128**, 355-361 (1995).

206. A. Kumar, N. Khandelwal, R. Malya, M. Reid, and A. Boriek, "Loss of dystrophin causes aberrant mechanotransduction in skeletal muscle fibers," FASEB journal: official publication of the Federation of American Societies for Experimental Biology **18**, 102-113 (2004).

207. L. Lacourpaille, F. Hug, A. Guével, Y. Péréon, A. Magot, J. Y. Hogrel, and A. Nordez, "Non‐invasive assessment of muscle stiffness in patients with duchenne muscular dystrophy," Muscle & nerve **51**, 284-286 (2015).

208. M. M. Brandão, A. Fontes, M. L. Barjas-Castro, L. C. Barbosa, F. F. Costa, C. L. Cesar, and S. T. O. Saad, "Optical tweezers for measuring red blood cell elasticity: application to the study of drug response in sickle cell disease," European Journal of Haematology **70**, 207-211 (2003).

209. G. Bao, and S. Suresh, "Cell and molecular mechanics of biological materials," Nature Materials **2**, 715-725 (2003).

210. K. Kim, C. G. Jeong, and S. J. Hollister, "Non-invasive monitoring of tissue scaffold degradation using ultrasound elasticity imaging," Acta biomaterialia **4**, 783-790 (2008).

211. R. Weissleder, "A clearer vision for in vivo imaging," Nature Biotechnology **19**, 316-316 (2001).

212. J. N. Bixler, B. H. Hokr, M. L. Denton, G. D. Noojin, A. D. Shingledecker, H. T. Beier, R. J. Thomas, B. A. Rockwell, and V. V. Yakovlev, "Assessment of tissue heating under tunable near-infrared radiation," J Biomed Opt **19**, 070501 (2014).

213. C. J. Miller, and L. A. Davidson, "The interplay between cell signalling and mechanics in developmental processes," Nature Reviews Genetics **14**, 733-744 (2013).

214. M. Behrndt, G. Salbreux, P. Campinho, R. Hauschild, F. Oswald, J. Roensch, S. W. Grill, and C.-P. Heisenberg, "Forces driving epithelial spreading in zebrafish gastrulation," Science **338**, 257-260 (2012).

215. Z. Meng, G. I. Petrov, and V. V. Yakovlev, "Flow cytometry using Brillouin imaging and sensing via time-resolved optical (BISTRO) measurements," Analyst **140**, 7160-7164 (2015).

216. C. W. Ballmann, J. V. Thompson, A. J. Traverso, Z. Meng, M. O. Scully, and V. V. Yakovlev, "Stimulated Brillouin Scattering Microscopic Imaging," Scientific Reports **5** (2015).

217. I. Remer, and A. Bilenca, "Background-free Brillouin spectroscopy in scattering media at 780 nm via stimulated Brillouin scattering," Optics Letters **41**, 926 (2016).

218. H. Yang, and Y. Xia, "Bionanotechnology: enabling biomedical research with nanomaterials," Advanced Materials **19**, 3085-3087 (2007).

219. Y. Xia, "Nanomaterials at work in biomedical research," Nat. Mater. **7** (2008).

220. T. Dvir, B. P. timko, D. S. Kohane, and R. Langer, "Nanotechnological strategies for engineering complex tissues," Nat. Nanotechnol. **6** (2010).

221. P. Kerativitayanan, J. K. Carrow, and A. K. Gaharwar, "Nanomaterials for Engineering Stem Cell Responses," Advanced Healthcare Materials, DOI: 10.1002/adhm.201500272 (2015).

222. N. Wang, J. P. Butler, and D. E. Ingber, "Mechanotransduction across the cell surface and through the cytoskeleton," Science **260**, 1124-1127 (1993).

223. B. K. K. Teo, S. T. Wong, C. K. Lim, T. Y. Kung, C. H. Yap, Y. Ramagopal, L. H. Romer, and E. K. Yim, "Nanotopography modulates mechanotransduction of stem cells and induces differentiation through focal adhesion kinase," ACS Nano **7**, 4785-4798 (2013).

224. A. K. Gaharwar, N. A. Peppas, and A. Khademhosseini, "Nanocomposite hydrogels for biomedical applications," Biotechnol. Bioeng. **111**, 441-453 (2014).

225. A. M. Kloxin, C. J. Kloxin, C. N. Bowman, and K. S. Anseth, "Mechanical properties of cellularly responsive hydrogels and their experimental determination," Advanced Materials **22**, 3484-3494 (2010).

226. K. S. Anseth, C. N. Bowman, and L. Brannon-Peppas, "Mechanical properties of hydrogels and their experimental determination," Biomaterials **17**, 1647-1657 (1996).

227. M. C. Koetting, J. T. Peters, S. D. Steichen, and N. A. Peppas, "Stimulus-responsive hydrogels: Theory, modern advances, and applications," Materials Science and Engineering: R: Reports **93**, 1-49 (2015).

228. J. R. Xavier, T. Thakur, P. Desai, M. K. Jaiswal, N. Sears, E. Cosgriff-Hernandez, R. Kaunas, and A. K. Gaharwar, "Bioactive nanoengineered hydrogels for bone tissue engineering: a growth-factor-free approach," ACS Nano **9**, 3109-3118 (2015).

229. J. W. Nichol, S. T. Koshy, H. Bae, C. M. Hwang, S. Yamanlar, and A. Khademhosseini, "Cell-laden microengineered gelatin methacrylate hydrogels," Biomaterials **31**, 5536-5544 (2010).

230. B. Fabry, G. N. Maksym, J. P. Butler, M. Glogauer, D. Navajas, and J. J. Fredberg, "Scaling the microrheology of living cells," Physical Review Letters **87**, 148102 (2001).

231. J. A. Burdick, T. M. Lovestead, and K. S. Anseth, "Kinetic chain lengths in highly cross-linked networks formed by the photoinitiated polymerization of divinyl monomers: A gel permeation chromatography investigation," Biomacromolecules **4**, 149-156 (2003).

232. A. Khanlari, M. S. Detamore, and S. H. Gehrke, "Increasing cross-linking efficiency of methacrylated chondroitin sulfate hydrogels by copolymerization with oligo (ethylene glycol) diacrylates," Macromolecules **46**, 9609-9617 (2013).

233. K. Koenig, and I. Riemann, "High-resolution multiphoton tomography of human skin with subcellular spatial resolution and picosecond time resolution," Journal of Biomedical Optics **8**, 432-439 (2003).

234. Y. Bai, P.-F. Lee, H. C. Gibbs, K. J. Bayless, and A. T. Yeh, "Dynamic multicomponent engineered tissue reorganization and matrix deposition measured with an integrated nonlinear optical microscopy–optical coherence microscopy system," Journal of biomedical optics **19**, 036014-036014 (2014).

235. C. Zhang, Y. S. Zhang, D.-K. Yao, Y. Xia, and L. V. Wang, "Label-free photoacoustic microscopy of cytochromes," Journal of Biomedical Optics **18**, 020504-020504 (2013).

236. J. Squier, M. Muller, G. Brakenhoff, and K. R. Wilson, "Third harmonic generation microscopy," Optics Express **3**, 315-324 (1998).

237. C. Xu, W. Zipfel, J. B. Shear, R. M. Williams, and W. W. Webb, "Multiphoton fluorescence excitation: new spectral windows for biological nonlinear microscopy," Proceedings of the National Academy of Sciences **93**, 10763-10768 (1996).

238. S. W. Hell, and J. Wichmann, "Breaking the diffraction resolution limit by stimulated emission: stimulated-emission-depletion fluorescence microscopy," Optics letters **19**, 780-782 (1994).

239. M. J. Rust, M. Bates, and X. Zhuang, "Sub-diffraction-limit imaging by stochastic optical reconstruction microscopy (STORM)," Nature Methods **3**, 793-796 (2006).

240. W. F. Oliver, C. A. Herbst, S. M. Lindsay, and G. H. Wolf, "A general method for determination of Brillouin linewidths by correction for instrumental effects and aperture broadening: Application to high‐pressure diamond anvil cell experiments," Review of scientific instruments **63**, 1884-1895 (1992).

241. V. R. Muzykantov, "Drug delivery by red blood cells: vascular carriers designed by mother nature," Expert Opinion on Drug Delivery **7**, 403-427 (2010).

242. S. C. Ritter, M. A. Milanick, and K. E. Meissner, "Encapsulation of FITC to monitor extracellular pH: a step towards the development of red blood cells as circulating blood analyte biosensors," Biomedical Optics Express **2**, 2012-2021 (2011).

243. J. W. Kang, N. Lue, C.-R. Kong, I. Barman, N. C. Dingari, S. J. Goldfless, J. C. Niles, R. R. Dasari, and M. S. Feld, "Combined confocal Raman and quantitative phase microscopy system for biomedical diagnosis," Biomedical Optics Express **2**, 2484-2492 (2011).

244. K. A. Sem'yanov, P. A. Tarasov, J. T. Soini, A. K. Petrov, and V. P. Maltsev, "Calibration-free method to determine the size and hemoglobin concentration of individual red blood cells from light scattering," Applied optics **39**, 5884-5889 (2000).

245. W. H. Grover, A. K. Bryan, M. Diez-Silva, S. Suresh, J. M. Higgins, and S. R. Manalis, "Measuring single-cell density," Proceedings of the National Academy of Sciences **108**, 10992-10996 (2011).

246. Z. N. Utegulov, J. M. Shaw, B. T. Draine, S. A. Kim, and W. L. Johnson, "Surface-plasmon enhancement of Brillouin light scattering from gold-nanodisk arrays on glass," in *NanoScience+ Engineering*(International Society for Optics and Photonics, 2007), pp. 66411M-66411M-66410.

247. A. C. De Luca, G. Rusciano, R. Ciancia, V. Martinelli, G. Pesce, B. Rotoli, L. Selvaggi, and A. Sasso, "Spectroscopical and mechanical characterization of normal and thalassemic red blood cells by Raman tweezers," Optics Express **16**, 7943-7957 (2008).

248. D. Schneditz, H. Heimel, and H. Stabinger, "Sound speed, density and total protein concentration of blood," Clinical Chemistry and Laboratory Medicine **27**, 803-806 (1989).

249. E. Evans, and Y.-C. Fung, "Improved measurements of the erythrocyte geometry," Microvascular research **4**, 335-347 (1972).

250. P. W. Kuchel, and E. D. Fackerell, "Parametric-equation representation of biconcave erythrocytes," Bulletin of mathematical biology **61**, 209-220 (1999).

251. M.-M. Khani, M. Tafazzoli-Shadpour, M. Rostami, H. Peirovi, and M. Janmaleki, "Evaluation of mechanical properties of human mesenchymal stem cells during differentiation to smooth muscle cells," Ann Biomed Eng **42**, 1373-1380 (2014).

252. M. G. Krebs, R. L. Metcalf, L. Carter, G. Brady, F. H. Blackhall, and C. Dive, "Molecular analysis of circulating tumour cells [mdash] biology and biomarkers," Nature reviews Clinical oncology **11**, 129-144 (2014).

253. M. M. Brandao, A. Fontes, M. L. Barjas‐Castro, L. C. Barbosa, F. F. Costa, C. L. Cesar, and S. T. O. Saad, "Optical tweezers for measuring red blood cell elasticity: application to the study of drug response in sickle cell disease," European Journal of Haematology **70**, 207-211 (2003).

254. K. A. Nelson, R. J. D. Miller, D. R. Lutz, and M. D. Fayer, "Optical generation of tunable ultrasonic waves," Journal of Applied Physics **53**, 1144-1149 (1982).

255. R. S. Moog, M. D. Ediger, S. G. Boxer, and M. D. Fayer, "Viscosity dependence of the rotational reorientation of rhodamine B in mono-and polyalcohols. Picosecond transient grating experiments," The Journal of Physical Chemistry **86**, 4694-4700 (1982).

256. W. H. Bragg, and W. L. Bragg, "The reflection of X-rays by crystals," Proceedings of the Royal Society of London. Series A, Containing Papers of a Mathematical and Physical Character, 428-438 (1913).

257. D. Pohl, and W. Kaiser, "Time-resolved investigations of stimulated Brillouin scattering in transparent and absorbing media: determination of phonon lifetimes," Physical Review B **1**, 31 (1970).

258. T. Sonehara, and H. Tanaka, "Forced Brillouin spectroscopy using frequency-tunable continuous wave lasers," Physical Review Letters **75**, 4234 (1995).

259. A. Pal, and A. Kumar, "Excess molar volumes and ultrasonic speeds of diethylene glycol monomethyl ether: N-alcohol mixtures at 298.15 K," Acoustics letters **20**, 203-212 (1997).